


Fall 11-14-2018

# Rate-Determining Step and Active Sites Probing for Platinum-Group-Metal Free Cathode Catalyst in Fuel Cell

Yechuan Chen  
*University of New Mexico*

Follow this and additional works at: [https://digitalrepository.unm.edu/cbe\\_etds](https://digitalrepository.unm.edu/cbe_etds)

 Part of the [Chemical Engineering Commons](#), and the [Nanoscience and Nanotechnology Commons](#)

---

## Recommended Citation

Chen, Yechuan. "Rate-Determining Step and Active Sites Probing for Platinum-Group-Metal Free Cathode Catalyst in Fuel Cell." (2018). [https://digitalrepository.unm.edu/cbe\\_etds/74](https://digitalrepository.unm.edu/cbe_etds/74)

This Dissertation is brought to you for free and open access by the Engineering ETDs at UNM Digital Repository. It has been accepted for inclusion in Chemical and Biological Engineering ETDs by an authorized administrator of UNM Digital Repository. For more information, please contact [disc@unm.edu](mailto:disc@unm.edu).

Yechuan Chen

*Candidate*

Chemical and Biological Engineering

*Department*

This dissertation is approved, and it is acceptable in quality and form for publication:

*Approved by the Dissertation Committee:*

Plamen Atanassov, Chairperson

Fernando Garzon

Iryna Zenyuk

Ivana Matanovic

Kateryna Artyushkova

**RATE-DETERMINING STEP AND ACTIVE SITES PROBING FOR  
PLATINUM-GROUP-METAL FREE CATHODE CATALYST IN FUEL CELL**

**BY**

**YECHUAN CHEN**

Bachelor of Science, Applied Chemistry, University of Electronic Science and  
Technology of China, 2012

Master of Science, Chemical Engineering and Technology, University of Electronic  
Science and Technology of China, 2015

**DISSERTATION**

Submitted in Partial Fulfilment of the  
Requirement for the Degree of

**Doctor of Philosophy  
Engineering**

The University of New Mexico  
Albuquerque, New Mexico

**December 2018**

## **DEDICATION**

To my wife Sherry, Xuemei Wang

To my parents Dan Chen & Lifang Ye

## ACKNOWLEDGEMENT

I would like to thank my academic advisor, Dr. Plamen Atanassov, for his leading and supervise. I would like to thank Dr. Alexey Serov & Dr. Kateryna Artyushkova, for their direct guidance throughout the first part and second part of my three years' PhD life respectively. In addition, I'd like to thank Dr. Rohan Gokhale & Dr. Tristan Asset, for their postdoc colleagueship and experimental mentorship.

I appreciate Dr. Fernando Garzon, Dr. Ivana Matanovic & Dr. Iryna Zenyuk, for their time, and commitment as committee members in both comprehensive exam and PhD defense.

Thanks to my colleagues and collaborators who have be engaged in this dissertation: Dr. Carlo Santoro, Dr. Santiago Rojas-Carbonell, Ms. Elizabeth Weiler & Ms. Rose Lee. Also, thanks to those who have inspired me in the same lab or group: Dr. Sadia Kabir, Ms. Mounika Kodali, Mr. Morteza Rezaei Talarposhti, Dr. Nalin Anderson and Ms. Shanti Nayak.

**RATE-DETERMINING STEP AND ACTIVE SITES PROBING FOR  
PLATINUM-GROUP-METAL FREE CATHODE CATALYST IN  
FUEL CELL**

Yechuan Chen

Bachelor of Science, Applied Chemistry, University of Electronic Science and

Technology of China, 2012

Master of Science, Chemical Engineering and Technology, University of Electronic

Science and Technology of China, 2015

Doctor of Philosophy, Engineering, University of New Mexico, 2018

**ABSTRACT**

With the increasing demand on renewable energy, the fuel cell has attracted more and more interests because of its large power density and controllable size. However, the insufficiency of element abundance and unstable expensive price of conventional platinum-based electrocatalysts used in anode and cathode makes it essential to find their substitutes. As one of the most promising candidates to be used in cathode for oxygen reduction reaction (ORR), iron-nitrogen-carbon (Fe-N-C) catalysts have been widely investigated and get commercialized recently, but still lacks comprehensive understanding on the kinetic mechanism.

This dissertation has been divided into three parts with a discussion on rate-determining step (RDS) and selective active sites inhibition of Fe-N-C ORR electrocatalyst. This first part utilizes kinetic isotope effect (KIE) to figure out that RDS is the first charge transfer and has different proton dependency in the kinetic-controlled region and mass transport-controlled region. The atomically dispersed Fe-N-C catalyst can achieve KIE around 1 in

the kinetic-controlled region, implying that Fe-N-C could compete with Pt-based catalysts by optimizing synthesis and structures, while KIE keeps around 2 but slightly decreases with potential dropping in the mass transport-controlled region, indicating that nitrogen active sites have strong proton dependence on kinetics.

In the second and third parts, nitrogen-contained tris(hydroxymethyl)aminomethane (Tris) and nitrogen-free 1-hydroxyethane 1,1-diphosphonic acid (HEDP) have been used as molecular probes to inhibit Fe-N-C catalysts. It is found that Tris has irreversible inhibition on iron active sites but reversible inhibition on nitrogen active sites, in addition that Tris could protonate pyridinic nitrogen active sites to enhance the 2-electron pathway, resulting in more reduction of oxygen to peroxide. It is also found that HEDP has no performance inhibition of iron active sites but obvious inhibition on pyrrolic/hydrogenated nitrogen active sites, leading to higher selectivity towards 4-electron pathway of oxygen reduction to water in ORR. These selective inhibitors reveal more research possibility on the mechanism study of Fe-N-C catalysts.

## Table of Contents

DEDICATION .....	iii
ACKNOWLEDGEMENT .....	iv
ABSTRACT .....	v
Table of Contents .....	vii
List of Figures .....	x
List of Tables .....	xii
Chapter 1 Introduction – Catalyst for Oxygen Reduction Reaction .....	1
Chapter 2 Experimental and Methods.....	7
Synthesis of Fe-N-C Catalysts .....	7
FeNCB for Chapter 3 and 5 .....	7
FeAApyr and AApyr for Chapter 4 .....	7
Fe-N-C via PPM for Chapter 6 .....	8
Electrochemistry Tests.....	8
Three electrode cell measurements in Chapter 3 .....	8
Three electrode cell measurements in Chapter 4 .....	9
Three electrode cell measurements in Chapter 5 .....	10
Three electrode cell measurements in Chapter 6 .....	11
Density Functional Theory (DFT) .....	11
X-ray Photoelectron Spectroscopy (XPS) .....	12
Extra Characterizations in Chapter 3 and 6 .....	14



Chapter 3 Rate-Determining Step of Fe-N-C Catalyst .....	15
Introduction – Determination of RDS in Acid.....	15
Brief Physical Properties of FeNCB .....	19
Determination of Kinetic Rate and KIE.....	21
Chapter Conclusion.....	29
Alternate Explanation of KIE with Approximation.....	30
Extra Exploration Experiments.....	32
Chapter 4 Inhibition of Active Sites with Nitrogen-Contained Chemical.....	36
Introduction – Inhibition of ORR Catalysts.....	36
DFT Calculation on Adsorption Energy of Tris .....	37
Results of Electrochemistry Tests.....	39
Chapter Conclusion.....	49
Extra Exploration Experiments.....	51
Chapter 5 Inhibition of Active Sites with Nitrogen-Free Chemical .....	55
Introduction – Selective Inhibition of Active Sites.....	55
DFT Calculation on Adsorption Energy of HEDP .....	56
XPS of HEDP Inhibition.....	59
Results of Electrochemistry Tests.....	64
Near Ambient-Pressure XPS of HEDP Inhibition .....	67
Chapter Conclusion.....	69

Extra Combination Experiments.....	71
Chapter 6 Rational Design of Synthesis to Get Specific Ratio of N Active Sites .....	73
Introduction – Polymerization-Pyrolysis Method.....	73
Synthesis of Fe-N-C via PPM.....	75
Polymerization .....	75
Pyrolysis.....	76
Ammonia processing .....	76
Properties and Discussion.....	77
Possible polymerization pathway .....	77
TGA and FTIR results .....	79
XRD pattern and BET results .....	80
XPS and Raman results.....	84
TEM figures .....	89
Electrochemistry Results .....	90
Chapter Conclusion.....	96
Chapter 7 Conclusion and Outlook.....	97
Conclusion .....	97
Outlook .....	98
References.....	100

## List of Figures

<b>Figure 3-1.</b> Diagrams of Koutecky-Levich and Tafel plots .....	19
<b>Figure 3-2.</b> Assorted spectra of FeNCB.....	21
<b>Figure 3-3.</b> LSV plots of four electrolytes .....	22
<b>Figure 3-4.</b> LSV, Koutecky-Levich and Tafel plots of four electrolytes .....	23
<b>Figure 3-5.</b> Results of Koutecky-Levich plots.....	25
<b>Figure 3-6.</b> Results of Tafel plots.....	25
<b>Figure 3-7.</b> Kinetic isotope effects .....	28
<b>Figure 3-8.</b> Kinetic isotope effects (HH/DD) extrapolated at different potentials.....	29
<b>Figure 3-9.</b> Kinetic isotope effects via approximated slopes .....	31
<b>Figure 3-10.</b> LSV, Koutecky-Levich and Tafel plots for NCB .....	33
<b>Figure 3-11.</b> Effective diffusion coefficient of O <sub>2</sub> as a function of #n .....	35
<b>Figure 4-1.</b> DFT optimized geometries of TrisH adsorption on active sites.....	39
<b>Figure 4-2.</b> RRDE LSV of FeAAPyr, AAPyr and 10% Pt/C.....	41
<b>Figure 4-3.</b> Secondary data from RRDE LSV .....	42
<b>Figure 4-4.</b> RRDE LSV data of Tris inhibition in HClO <sub>4</sub> .....	46
<b>Figure 4-5.</b> Secondary data of Tris inhibition LSV in HClO <sub>4</sub> . .....	47
<b>Figure 4-6.</b> Schematic diagram of ORR mechanism changes .....	50
<b>Figure 4-7.</b> LSV of cumulative loadings in Tris .....	51
<b>Figure 4-8.</b> RRDE data for 0.1 M of Tris inhibition in different loadings.....	53
<b>Figure 4-9.</b> LSV data of different FeAAPyr inks.....	54
<b>Figure 5-1.</b> The types of chemical moieties present in the MNC catalyst .....	56
<b>Figure 5-2.</b> DFT optimized geometries of assorted active sites.....	58

<b>Figure 5-3.</b> DFT geometries of HEDP on assorted active sites .....	59
<b>Figure 5-4.</b> High resolution P 2p spectra for FeNCB sample .....	61
<b>Figure 5-5.</b> High-resolution N 1s spectra in UHV .....	61
<b>Figure 5-6.</b> High resolution N 1s spectra in UHV with deconvolution .....	62
<b>Figure 5-7.</b> LSV data of catalyst tested in 0.5 M sulfuric acid .....	65
<b>Figure 5-8.</b> LSV disk polarization data of catalyst .....	65
<b>Figure 5-9.</b> Koutecky-Levich plots of HEDP inhibition.....	66
<b>Figure 5-10.</b> High resolution O 1s spectra .....	68
<b>Figure 5-11.</b> High-resolution N 1s spectra and difference spectra .....	68
<b>Figure 5-12.</b> Two parallel pathways of the ORR mechanism.....	70
<b>Figure 5-13.</b> RRDE data of FeNCB after sequential inhibition and washing .....	71
<b>Figure 6-1.</b> Schematic diagram of PPM process using in situ SSM .....	74
<b>Figure 6-2.</b> Polymerization diagram .....	78
<b>Figure 6-3.</b> (a) TGA plots and (b) FTIR spectra of polymers.....	80
<b>Figure 6-4.</b> Raw and fitted XRD patterns .....	81
<b>Figure 6-5.</b> XPS spectra of nitrogen in different catalysts .....	86
<b>Figure 6-6.</b> XPS spectra of iron in different catalysts.....	87
<b>Figure 6-7.</b> Raman spectra of 26AMP-in and 26DAP-in.....	89
<b>Figure 6-8.</b> TEM images .....	90
<b>Figure 6-9.</b> LSV and H <sub>2</sub> O <sub>2</sub> % in alkaline and acid.....	92
<b>Figure 6-10.</b> Tafel plots of four electrocatalysts .....	94

## List of Tables

<b>Table 3-1.</b> Parameters of linear regression for Koutecky-Levich and Tafel plots .....	24
<b>Table 4-1.</b> Adsorption energy of Tris, TrisH and O <sub>2</sub> on active sites.....	38
<b>Table 5-1.</b> Adsorption energy of HEDP on assorted actives sites .....	57
<b>Table 5-2.</b> Relative speciation of nitrogen species.....	62
<b>Table 5-3.</b> Relative speciation of nitrogen species in NAPXPS .....	69
<b>Table 6-1.</b> XRD fitting datasheet of different catalysts .....	83
<b>Table 6-2.</b> BET surface areas of different catalysts .....	84
<b>Table 6-3.</b> XPS datasheet of different catalysts .....	88
<b>Table 6-4.</b> Parameters of Tafel plots .....	94

## Chapter 1

### Introduction – Catalyst for Oxygen Reduction Reaction

Since the first commercial fuel cell made by General Electric was utilized to generate power in NASA space program Project Gemini for satellites and space capsules, this system has attracted more and more interests in various applications such as fuel cell vehicle<sup>1</sup>, wastewater treatment<sup>2</sup> and carbon dioxide reduction<sup>3</sup>. Currently, there are several types of fuel cell systems that have been researched mostly<sup>4</sup>: Proton Exchange Membrane Fuel Cell (PEMFC)<sup>5-6</sup>, Alkaline Fuel Cell<sup>7</sup> (AFC), & Direct Methanol Fuel Cell (DMFC)<sup>8</sup> which mainly work below 100 °C, Phosphoric Acid Fuel Cell<sup>9</sup> (PAFC) working below 200 °C, Molten Carbonate Fuel Cell<sup>10</sup> (MCFC), Solid Oxide Fuel Cell<sup>11</sup> (SOFC) that is utilized around 800 °C, *et cetera*. Though these fuel cells have different electrolytes and fuels, they all consist of three segments: anode, electrolyte and cathode. Catalysts on both electrodes are essential to make the whole system work efficiently. Up to date, platinum is the most widely used anode and cathode catalyst in PEMFC, AFC, DMFC and PAFC for fuel oxidation reaction and oxygen reduction reaction. However, due to its high price and unstable trending<sup>12</sup> as one of the precious metals (from *ca.* \$2000 per ounce at May 2008 to *ca.* \$1000 per ounce at January 2018), it will be not practical to achieve hundreds of gigawatt-scale fuel cell application without optimization<sup>13</sup>. Two routes have been widely investigated to lower down the cost of catalysts<sup>14</sup>: lowering down the loading of platinum and looking for substitutes. Alloys of Pt and earth-abundant metals (*e.g.* Pt/Ni<sup>15</sup> and Pt/Co<sup>16</sup>) and nanostructure synthesis (such as core-shell<sup>17</sup> and hollow nanosphere<sup>18</sup>) are the two main methods to get ultralow platinum usage. To find efficient platinum substitutes, numerous candidates have been checked and tested either for anode or cathode, ranging

from transition metal inorganic nanoparticles (for instance, carbides<sup>19</sup>, nitrides<sup>20</sup>, oxides<sup>21</sup> and chalcogenide<sup>22</sup>), carbon-based materials (like porous carbon<sup>23</sup>, carbon nanotube<sup>24</sup> and graphene<sup>25</sup>) to metal-nitrogen-carbon (M-N-C) composite catalysts (as macrocycle based<sup>26</sup>, metal-organic-framework based<sup>27</sup> and nanostructure based<sup>28-30</sup>). Among these plentiful contenders, M-N-C material, specially iron-nitrogen-carbon (Fe-N-C), is one of the most promising platinum-group-metal (PGM) free cathode catalysts for oxygen reduction reaction (ORR).

At present, Fe-N-C catalyst still cannot compare to platinum from both half-wave potential in half-cell test (via rotating electrode disk, RDE) and on-set potential and power density in full-cell test (via membrane electrode assembly, MEA). For instance, Wu *et al.*<sup>31</sup> reported Fe-N-C catalyst synthesized from polyaniline, getting the half-wave potential of 43 mV to 59 mV lower than commercial Pt/C catalyst (0.85 V versus reversible hydrogen electrode, RHE) in acidic media. Chen *et al.*<sup>32</sup> synthesized polypyridine based Fe-N-C material and achieved 0.89 V half-wave potential in 1 M KOH alkaline media, which is comparable with the one of commercial Pt/C, but much lower diffusion current density (3.2 mA cm<sup>-2</sup> versus ca. 6 mA cm<sup>-2</sup> of platinum). To achieve better activity and durability of Fe-N-C cathode catalysts, it is essential to understand the different mechanism between Fe-N-C with the conventional platinum catalyst. For Pt based cathode catalyst, the mechanism has been researched for more than 50 years<sup>33</sup>, almost reaching state-of-the-art. In acid media, it is confirmed that ORR mainly follow a 4-electron pathway from an oxygen molecule to water molecule<sup>34</sup>, which could be further divided into four 1-electron steps. In alkaline media (i.e. AFC), it is found that oxygen reduction reaction undergoes two possible pathways<sup>35</sup>: one is direct 4-electron pathway from oxygen molecule to hydroxide

ion, the other is 2-electron pathway from oxygen molecule to peroxide ion followed by further reduction from peroxide ion to hydroxide ion. When the case goes to Fe-N-C catalyst, the mechanism becomes much more complicated. The pathways in both acidic and alkaline media are similar to the ones of Pt, but it is found that there are multiple active sites consisting of various structures that undergo different pathways<sup>36</sup>. Iron active sites are called Fe-N<sub>x</sub> (one iron atom bonded with several nitrogen atoms) and separated into 3 groups: Fe-N<sub>4</sub> (can undergo 4-electron pathway), Fe-N<sub>3</sub> (can only reduce peroxide) and Fe-N<sub>2</sub> (can reduce both oxygen molecule and peroxide). In addition, some nitrogen-carbon (N-C) networks are also found to be electrochemically active for oxygen reduction: pyrrolic (or protonated/hydrogenated) N can reduce oxygen molecule to peroxide and pyridinic N is able to reduce peroxide into water molecule. As each synthesis route using assorted metal and nitrogen precursors has its specific iron-nitrogen-carbon ratio, it is necessary to distinguish the rate-determining step and active sites ratio so that researchers can understand which active site has the synthesis priority.

Corresponding rate-determining step (RDS) research for platinum catalyst has been reported for decades. In 1985, Ghoneim *et al.*<sup>37</sup> utilized kinetic isotopic effect (KIE) method via deuterium (D) and hydrogen (H), finding that in phosphoric acid media, H<sub>3</sub>PO<sub>4</sub> and D<sub>3</sub>PO<sub>4</sub> led to same Tafel slopes (*i.e.* similar reaction free energy) and KIE was calculated to be *ca.* 1 after overpotential and temperature calibration. This result reveals that the kinetic step of oxygen reduction reaction for bulk platinum is not limited by proton related factors. Another precious metal gold, was also investigated via KIE method by Mei *et al.*<sup>38</sup> in 2014, since Au (100) is widely used as a working electrode in electrochemistry. It is found that on gold surface ORR is pH dependent, undergoing 4-electron mechanism



in alkaline media but proton diffusion limited mechanism in acidic media as oxygen molecule needs first to combine with one proton to form  $\text{HO}_2$  which could then be further reduced. Investigation of KIE for PGM-free catalysts is rare. Tse *et al.*<sup>39</sup> in 2016 reported that Fe-N-C synthesized from polyaniline has kinetic isotopic effect in both acidic and alkaline media. The calculation was based on a comparison of kinetic current densities derived from Koutecky-Levich plots via testing rotating disk electrode in different rotation speeds. They also utilized a similar method to compare KIE between RDEs with and without Nafion (used as binder/ionomer in half-cell test and ionomer in full-cell test), finding that Nafion could compensate protons and result in lower kinetic isotopic effect. Malko *et al.*<sup>40</sup> in 2017 utilized Tafel plots and Gibbs free energy to calculate KIE for PGM-free catalyst synthesized from polyaniline derivative. By doing overpotential calibration, it is found that their Fe-N-C catalyst has a KIE of 3.4 in acidic and KIE of 2.5 in alkaline media. They also reported a KIE of 1.8 for corresponding iron-free N-C catalyst synthesized from the same precursor, implying that nitrogen active sites have proton limited mechanism to reduce oxygen. It is essential to compare these two different calculation methods using one Fe-N-C catalyst to check whether rate-determining step could be universal among different methods derived PGM-free ORR catalysts. In addition, it is important to know whether arbitrary selected Fe-N-C catalyst leads to same proton dependent results or not, as this indicates if Fe-N-C could reach as high kinetic rate as Pt. As there are assorted active sites for Fe-N-C catalyst, distinguishing them is important to tell whether a specific active site applies to the rate-determining step discovered by KIE or is a secondary factor that doesn't have much impact on global performance. Researches on this topic originated from Fe-N-C catalyst poisoning test with chemicals that inhibit

conventional Pt/C materials or deactivate iron-contained proteins. Thorum *et al.*<sup>41</sup> in 2011 reported Fe-N-C and Cu-N-C inhibition results with NaF, KSCN, EtSH (ethanethiol), NaN<sub>3</sub> and KCN in acidic media. It is found that Cu-N-C catalyst could suffer more than 200 mV of a decrease in half-wave potential when facing these inhibitors while Fe-N-C is much more resistant. However, Fe-N-C that was derived from iron phthalocyanine in their study could be severely poisoned by KCN, which is a fatal chemical to hemoglobin with an iron complex center. In 2012, von Deak *et al.*<sup>42</sup> utilized pretest gas treatment on ORR catalysts in hydrogen and hydrogen sulfide atmospheres respectively. It is found that in acidic media conventional Pt/C catalyst got decreases of half-wave potential and diffusion current density while Fe-N-C catalyst achieved more than 50 mV higher E<sub>1/2</sub> and a *ca.* 30% increase of current density after H<sub>2</sub>S treatment. The data from X-ray absorption (XANES) and photoelectron (XPS) spectra reveal that Fe-N<sub>x</sub> sites got poisoned by hydrogen sulfide and the increase of performance is probably attributed to carbidic iron phase. This hypothesis got supported by Singh *et al.*<sup>43</sup> in 2014, reporting that their Fe-N-C catalyst which was derived from phenanthroline got decreased performance after H<sub>2</sub>S treatment. In recent years, there are many reports showing cyanide<sup>44-45</sup>, chloride<sup>46</sup>, carbon monoxide<sup>47</sup>, sulfide<sup>48</sup>, nitric monoxide<sup>49-50</sup> and phosphate<sup>51</sup> have inhibition effect for Fe-N-C and other M-N-C catalysts. However, these reports mainly concentrate on iron or metal active sites, without data and analysis for ring current density (it comes from the reduction of peroxide), which is important to reveal the inhibition and activity of nitrogen active sites. In addition, most of the current researched inhibitors are environmentally harmful or difficult to operate. It is essential to find specific chemicals that could distinguish N-C active sites and Fe-N<sub>x</sub>

active sites or could be operationally simple to be universally used on all metal-nitrogen-carbon catalysts for probing.

## Chapter 2

### Experimental and Methods

#### Synthesis of Fe-N-C Catalysts

Two Fe-N-C catalysts have been used. The catalyst synthesized from N-C precursor nicarbazin is designated as FeNCB and used in RDS (Chapter 3) and HEDP (Chapter 5) researches. The catalyst derived from N-C precursor aminoantipyrine is designated as FeAApyr and used in Tris (Chapter 4) research, with corresponding iron-free catalyst designated as AApyr.

#### *FeNCB for Chapter 3 and 5*

FeNCB was synthesized via previously reported Sacrificial Support Method<sup>52</sup> (SSM). A calculated amount of nicarbazin (1,3-bis(4-nitrophenyl)urea compound with 4,6-dimethyl-1H-pyrimidin-2-one, from Sigma-Aldrich), iron nitrate (from Sigma-Aldrich) and assorted silica (Stöber spheres synthesized in-house with a diameter of 370 nm, Cab-O-Sil<sup>®</sup> LM-150 and Cab-O-Sil<sup>®</sup> OX-50) were mixed together in a viscous solution, dried and ball-milled. Then, they were pyrolyzed at 950 °C under 7% H<sub>2</sub> – 93 % N<sub>2</sub> atmosphere, etched in HF for 4 days after a second ball-milling and heat treated at 950 °C under NH<sub>3</sub> atmosphere, before a final ball-milling. The final cooled down catalyst was collected for research.

#### *FeAApyr and AApyr for Chapter 4*

FeAApyr and AApyr were also synthesized via previously reported SSM<sup>48, 53</sup> with different parameters. FeAApyr was prepared by mixing iron nitrate and aminoantipyrine (4-Amino-2,3-dimethyl-1-phenyl-3-pyrazolin-5-one, from Sigma-Aldrich). In the case of metal-free

catalyst AAPyr, only the organic precursor was used. In both cases, the monodispersed silica Cab-O-Sil<sup>®</sup> LM-150 with a surface area of 250 m<sup>2</sup> g<sup>-1</sup> was impregnated with mentioned above precursors. The material was then homogenized using ball milling for 30 minutes. High-temperature treatment was done in a quartz tube in an inert atmosphere of UHP nitrogen. The gas flow was constant at 100 mL min<sup>-1</sup>. The temperature was increased from room temperature to 950 °C with a ramp rate of 25 °C min<sup>-1</sup>. The sample was heat treated for 45 minutes. The silica template was etched using 20 wt% HF overnight (*ca.* 12 h). The catalyst was then washed with DI water until the neutral pH of the supernatant was reached. The catalyst was then dried for research.

### ***Fe-N-C via PPM for Chapter 6***

The detailed description for Polymerization Pyrolysis Method (PPM) is given in Chapter 6 for better understanding, as it is the main theme of that chapter.

## **Electrochemistry Tests**

### ***Three electrode cell measurements in Chapter 3***

Linear sweep voltammetry (LSV) measurements were performed via a three-electrode electrochemical cell system with data collected by WaveNow potentiostat (PINE research). The three electrodes are: model E7R9 rotating ring disk electrode (RRDE) with a glassy carbon disk of 0.2472 cm<sup>2</sup> as the working electrode (the ring is not used for data collection); single junction silver chloride (Ag/AgCl) electrode as a reference electrode; graphite rod electrode as the counter electrode. Two Ag/AgCl electrodes (one filled with KCl saturated H<sub>2</sub>O while the other by KCl saturated D<sub>2</sub>O) were used for light water and heavy water tests respectively. Corresponding LSV parameters are: 0.2 mg cm<sup>-2</sup> catalyst loading, 5 mV s<sup>-1</sup>

scanning rate from 0.8 V to  $-0.2$  V *vs.* Ag/AgCl and rotating speeds at 1000, 1200, 1400, 1600, 1800 and 2000 rpm. The ink was prepared as previously presented<sup>54-55</sup>, by sonicating 5 mg of FeNCB in 75  $\mu$ L of 1% Nafion solution and 925  $\mu$ L of 1:4 isopropanol-water mixture, leading to a 15% weight ratio of Nafion to the catalyst. Electrolytes are 0.5 M H<sub>2</sub>SO<sub>4</sub> H<sub>2</sub>O (HH), 0.5 M D<sub>2</sub>SO<sub>4</sub> H<sub>2</sub>O (DH), 0.5 M H<sub>2</sub>SO<sub>4</sub> D<sub>2</sub>O (HD) and 0.5 M D<sub>2</sub>SO<sub>4</sub> D<sub>2</sub>O (DD). For HH and DH, the KCl saturated H<sub>2</sub>O Ag/AgCl was used, whereas the KCl saturated D<sub>2</sub>O Ag/AgCl was used for DH and DD, thus avoiding junction potentials<sup>39-40, 56</sup>. LSV were performed with the same catalyst layer in sequence: HH, washed by light water, DH, washed by heavy water, HD, washed by heavy water, DD. All potentials are reported relative to the reversible hydrogen electrode (RHE).

#### ***Three electrode cell measurements in Chapter 4***

RRDE was used to determine the performances of FeAAPyr and metal-free AAPyr in acidic media with/without the addition of Tris (or tris(hydroxymethyl)aminomethane, from Sigma-Aldrich). The working electrode is model E7R9 rotating ring disk electrode (the ring is used for data collection), having a glassy carbon disk of 0.2472 cm<sup>2</sup> and platinum ring of 0.1859 cm<sup>2</sup> with 37% collection efficiency. The ink preparation was the same one as described previously, but by replacing FeNCB with FeAAPyr or AAPyr. The catalyst loading on the disk was 200  $\mu$ g cm<sup>-2</sup>. LSV was run from 0.8 to  $-0.2$  V *versus* Ag/AgCl at a scan rate of 5 mV s<sup>-1</sup> for FeAAPyr sample, while from 0.65 to  $-0.35$  V for AAPyr sample. The potentials on ring electrode for both samples were set at 1.1 V *vs.* Ag/AgCl. A graphite rod electrode was used as the counter electrode. After every test, a calculated amount of Tris was added, and the pH was controlled to be lower than 1. Two series of electrochemical inhibition studies were done independently. The first set of experiments

tested electrode made from FeAAPyr catalyst with the following concentrations of Tris in 0.5 M H<sub>2</sub>SO<sub>4</sub> and in 1 M KOH: 0.001 M, 0.01 M, 0.1 M, 0.8 M. The second study tested both FeAAPyr and AAPyr in 1 M HClO<sub>4</sub> using the following concentrations of Tris: 0.1 M, 0.15 M, 0.2 M, 0.25 M, 0.3 M, 0.4 M, 0.5 M, 0.6 M, 0.7 M, 0.8 M. After LSV was recorded in the 0.8 M solution of Tris, the electrolyte was changed to a freshly prepared 0.5 M H<sub>2</sub>SO<sub>4</sub>, 1 M HClO<sub>4</sub> or 1M KOH while the working electrode was immersed and kept 1600 rpm rotating in de-ionized (DI) water for 5 minutes (DI water was changed 3 times). After washing, the working electrode was used for ORR measurements in the Tris-free electrolytes. The tests under this condition are designated as 'R' (recovery or refresh). The reference tests of commercial Pt were performed in Tris in 0.5 M H<sub>2</sub>SO<sub>4</sub> using the following concentrations of Tris: 0.001 M, 0.01 M, 0.1 M, 0.8 M. The ink formulation was modified for the commercial Pt/C (Aldrich, 10 wt. % of Pt), to achieve a 40 μg cm<sup>-2</sup> loading while maintaining an identical Nafion (N) over Carbon (C) ratio with the PGM-free ink (N/C = *ca.* 0.15).

### ***Three electrode cell measurements in Chapter 5***

RRDE measurements were performed via three electrode electrochemical cell system with data collected by WaveNow potentiostat. The working electrode is model E7R9 rotating ring disk electrode (the ring is used for data collection). The reference electrode is Ag/AgCl calibrated in saturated KCl solution, while the counter electrode is a graphite rod. The FeNCB ink recipe is the same one as previously described. 30 μL of this ink (5 μL one time) was added on the surface of RRDE, leading to about 0.6 mg cm<sup>-2</sup> loading of the catalyst. Electrolyte for testing is 100 mL of 0.5 M sulfuric acid. The rotation speed of RRDE is 1600 rpm, in addition to a scanning rate of 5 mV s<sup>-1</sup> ranging from 0.8 V to -0.2

V versus Ag/AgCl. HEDP was etidronic acid monohydrate (from Sigma Aldrich) (or 1-hydroxyethylidenediphosphonic acid) and added into the electrolyte to achieve 0.3 M concentration for inhibition test. The refreshed electrochemical test was prepared by adding pure 0.5 M sulfuric acid into the cell after washing, as well as cleaning of rotating RRDE in deionized water for 15 minutes.

### ***Three electrode cell measurements in Chapter 6***

Electrochemical characterization was performed using Pine Instrument analytical system. For working electrode, the inks were prepared by dispersing of 5 mg of catalysts in a mixture of 850  $\mu\text{L}$  DI/IPA (deionized water and isopropanol, 4:1 by volume) and 150  $\mu\text{L}$  of 0.5 % Nafion solution. After 90 seconds of the sonication, 30  $\mu\text{L}$  was applied on a glassy carbon rotating ring-disk electrode (RRDE) with a disk surface area of 0.2472  $\text{cm}^2$  and a ring surface area of 0.1859  $\text{cm}^2$ . The catalyst loading was calculated to be 0.6  $\text{mg}/\text{cm}^2$ . The electrolyte was oxygen saturated 1 M KOH and 0.5 M sulfuric acid, while Hg/HgO and Ag/AgCl electrodes were used as reference electrodes respectively. In addition, graphite electrode is used as a counter electrode in both acid and base electrolytes. All data were calibrated and reported versus reversible hydrogen electrode (RHE).

### **Density Functional Theory (DFT)**

The calculations were performed using plane-wave pseudopotential implementation of DFT<sup>57-58</sup> with the Perdew-Burke-Ernzerhof (PBE) functional<sup>59-60</sup> with the use of Vienna Ab initio Simulation Package (VASP)<sup>61-62</sup>. Fe-N<sub>x</sub> and graphitic nitrogen sites were modeled using extended surfaces with the dimensions of 17.04  $\text{\AA}$   $\times$  17.04  $\text{\AA}$ ,  $\gamma = 60^\circ$  and a vacuum region of 20  $\text{\AA}$ . Pyridinic and hydrogenated pyridinic nitrogen were modeled using



the nanoribbons, which were constructed from  $4 \times 2$  orthorhombic super cells with the size of  $9.84 \text{ \AA} \times 23.52 \text{ \AA}$  and with a vacuum regions of  $15 \text{ \AA}$  in z- and y-direction. Pt (111) surface was modeled using three layers of Pt atoms in the unit cell of the size  $11.2 \times 11.2 \text{ \AA}$  and a vacuum region of  $20 \text{ \AA}$ . The electronic energies were calculated using tetrahedron method with Blöchl correction<sup>63</sup> and  $3 \times 3 \times 1$  k-point Monkhorst-Pack<sup>64</sup> mesh in the case of the extended surfaces and  $8 \times 1 \times 1$  k-points in the case of the super cells used to model edge defects. In all the cases, plane-wave basis cut off was set to 700 eV.

Adsorption energies of Tris and protonated Tris (TrisH) in Chapter 4 and mono-deprotonated HDEP in Chapter 5 at different defects ( $\Delta E_{ad}$ ) were calculated using the following formula:

$$\Delta E_{ad} = E_{surface+ad} - [E_{surface} + E_{ad}] \quad \text{Eq. 2-1}$$

where  $E_{surface+ad}$  is the energy of Tris, TrisH or mono-deprotonated HDEP adsorbed on the certain defect,  $E_{surface}$  is the energy of the extended surface or a nanoribbon, and  $E_{ad}$  is the energy of the Tris, TrisH or mono-deprotonated HDEP molecule in the gas phase. In each case, multiple adsorption orientations were considered, but the results reported in work correspond to the most preferable adsorption orientation.

### **X-ray Photoelectron Spectroscopy (XPS)**

In Chapter 5, XPS was used to investigate the inhibition effect of HEDP on the surface of FeNCB catalyst. In a previous study using variable energy ambient pressure XPS, 1400 and 550 eV energy sources were utilized<sup>65</sup>. Due to the lower energy source available at the beamline where synchrotron experiments were done, to match the same energies, lab-based XPS was also utilized for higher incident energy experiment.

Catalyst coated carbon papers were prepared for XPS analysis. 10 mg of pure FeNCB was first sonicated in 3 mL isopropanol for 1.5 min (30 sec one time), followed by dropping 900  $\mu\text{L}$  (100  $\mu\text{L}$  one time) onto a piece of 1  $\text{cm}^2$  GDL 29 BC carbon paper (purchased from SGL). After each dropping, the carbon paper was air dried to evaporate isopropanol. Two 0.25  $\text{cm}^2$  pieces of this carbon paper were used as a pure sample for UHV XPS and synchrotron-based XPS. Two other 0.25  $\text{cm}^2$  pieces of the same carbon paper with FeNCB were dipped into 0.3 M HEDP solution in deionized water for 1 min. The pieces then were washed in deionized water for 15 min followed by air drying.

Kratos Ultra DLD XPS spectrometer utilizing monochromatic Al  $K\alpha$  source with the energy of 1486.6 eV was used for laboratory-based analysis of surface chemistry. High-resolution C 1s and N 1s spectra were obtained at 20 eV pass energy. The same samples were analyzed at Beamline 9.3.2 near ambient-pressure soft XPS (NAP-XPS) in Advanced Light Source at Lawrence Berkeley National Laboratory (DOE Office of Science User Facility under contract no. DE-AC02-05CH11231). C 1s and N 1s spectra were acquired at vacuum conditions and in an equal pressure mixture of oxygen and water of total 200 mTorr pressure at 80 °C.

Data analysis and quantification were performed using CasaXPS software. Linear background subtraction was used for quantification of C 1s and N 1s spectra. Sensitivity factors provided by the manufacturer were utilized. A 70% Gaussian / 30% Lorentzian line shape was utilized in the curve-fit of spectra. For spectral subtraction, spectra were smoothed and normalized to the same total area. For curve-fitting, original non-smoothed data were used for both lab-based and synchrotron-based spectrometers.

### **Extra Characterizations in Chapter 3 and 6**

Scanning electron microscope (SEM) images were collected by Hitachi S-5200. Transmission electron microscopy (TEM) images were obtained using JEOL JEM-2010. WITec alpha300 RA was used to get Raman spectroscopy data while X-ray diffraction (XRD) data was carried out using Rigaku SmartLab. Data for Fourier transform infrared spectroscopy (FTIR), and Thermogravimetric analysis (TGA) were acquired by Thermo Nicolet 6700 and TA SDT Q600 respectively. Micromeritics Gemini 2360 is used to get surface areas via Brunauer-Emmett-Teller (BET) analysis. XPS is also used in these two chapters, using Kratos Ultra DLD XPS with the same parameters.

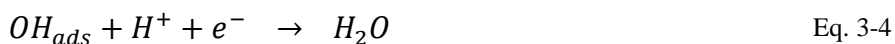
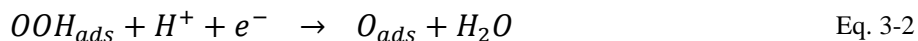
## Chapter 3

### Rate-Determining Step of Fe-N-C Catalyst

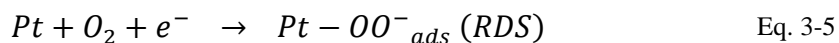
The contents in this chapter have been submitted as “Kinetic Isotopic Effect Research of Fe-N-C Electrocatalyst for Oxygen Reduction Reaction in Acid” to Journal of the American Chemical Society for revision. Co-authors are Tristan Asset, Rose Lee (electrochemistry tests), Kateryna Artyushkova and Plamen Atanassov.

#### Introduction – Determination of RDS in Acid

According to previous research<sup>36</sup>, Fe-N<sub>x</sub> (x = 2, 3 or 4) active site is the main electrocatalysis center in Fe-N-C catalyst for the oxygen reduction reaction in an acidic environment, with a 4-electron pathway similar as platinum<sup>34</sup>. The mechanism can be roughly written as four steps, as shown below:

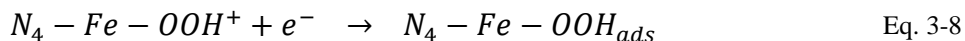
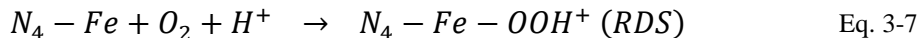


Here ‘ads’ means adsorption on the electrocatalyst surface. Among these four steps, the first charge transfer has been proved to be the slowest one<sup>66</sup>, *i.e.* rate-determining step (RDS). By replacing the hydrogen ion with a deuterium ion<sup>37,39</sup>, it has been found that this electron transfer step on Pt surface could be further decomposed into two steps, as shown below:





The adsorption of oxygen molecule on platinum and first charge transfer is independent of hydrogen ion. As a comparison, it was reported<sup>39-40</sup> that first charge transfer on Fe-N-C surface is probably dependent of the proton, which could be decomposed in another form:



The oxygen molecule needs to combine with a hydrogen ion, forming an adsorbed intermediate on the iron surface before getting an electron from the electrocatalyst. Hence, the proton needs to diffuse, either from the double layer or on the surface, to the active sites (the Fe-N-C electrocatalysts exhibiting a low density of active sites onto the surface, *i.e.* here for FeNCB, the Fe loading is 0.06 at. %). This phenomenon, as well as the oxygen transport, is likely to influence the rate determining step<sup>67-68</sup>. Surface diffusion of the proton is more complicated progress on Fe-N-C surface than Pt/C since Nafion has strong binding energy with iron active sites<sup>69</sup> and possible to compensate proton when it is insufficient<sup>39</sup>, as well as possible diffusion directly from pyrrolic / hydrogenated pyridinic / quaternary nitrogen active sites. Recent Fe-N-C pH-dependence research<sup>70</sup> indicates that hydrogenated pyridinic N-C active site is able to provide proton to neutralize adsorbed hydroxide ion for oxygen reduction in alkaline media.

As hydrogen ion is so important for RDS of ORR in acid, it is an efficient way to observe whether there is a change of kinetic rate by replacing hydrogen with deuterium, *i.e.* kinetic isotopic effect (KIE). In electrochemistry, the kinetic rate is mostly derived by linear

regression of either Koutecky-Levich plot or Tafel plot from data of linear sweep voltammetry (LSV). The corresponding Koutecky-Levich equation could be written as:

$$\frac{1}{j} = \frac{1}{j_k} + \frac{1}{j_{MT}} \quad \text{Eq. 3-9}$$

$$\frac{1}{j_{MT}} = \frac{1}{0.62nFC_{O_2}D_{O_2}^{2/3}\nu^{-1/6}\omega^{1/2}} \quad \text{Eq. 3-10}$$

$j$  is the current density directly measured by a potentiostat,  $j_k$  the kinetic current density, and  $j_{MT}$  the mass transport current density,  $n$  the number of electron,  $F$  the Faraday constant,  $C_{O_2}$  the concentration of oxygen ( $1.12 \times 10^{-6} \text{ mol cm}^{-3}$  in light water and  $1.23 \times 10^{-6} \text{ mol cm}^{-3}$  in heavy water<sup>53, 71-73</sup>),  $D_{O_2}$  the oxygen diffusion coefficient ( $1.90 \times 10^{-5} \text{ cm}^2 \text{ s}^{-1}$  in light water and  $1.63 \times 10^{-5} \text{ cm}^2 \text{ s}^{-1}$  in heavy water<sup>74</sup>),  $\nu$  the electrolyte kinematic viscosity ( $1.00 \times 10^{-2} \text{ cm}^2 \text{ s}^{-1}$  in light water and  $1.10 \times 10^{-2} \text{ cm}^2 \text{ s}^{-1}$  in heavy water<sup>75</sup>) and  $\omega$  the rotation speed of disk electrode (from 1000 *rpm* to 2000 *rpm*, converted in  $\text{rad s}^{-1}$ ). By doing linear regression using  $\omega^{-1/2}$  as X-axis and  $j^{-1}$  as Y-axis, with  $j$  determined in the mass-transport limited region,  $j_k$  could be derived from the reciprocal of Y-intercept, which further leads to rate constant  $k_k$  and KIE by using these equations:

$$j_k = nFk_kC_{O_2} \quad \text{Eq. 3-11}$$

$$KIE = \frac{k_k(H)}{k_k(D)} \quad \text{Eq. 3-12}$$

The Tafel slope describes the reaction kinetics and is derived from the Butler-Volmer equation, which can be written as below:

$$E = E^0 + \frac{2.303RT}{\alpha n_{\alpha}F} \log j_0 - \frac{2.303RT}{\alpha n_{\alpha}F} \log j \quad \text{Eq. 3-13}$$

$$\eta = \frac{2.303RT}{\alpha n_{\alpha}F} \log \frac{j_0}{j} \quad \text{Eq. 3-14}$$

$E^0$  is the standard potential of the ORR,  $\alpha$  the electron transfer coefficient,  $n_\alpha$  the corresponding number of electrons transferred (regarded as 1 in the RDS),  $F$  the Faraday constant,  $R$  the gas constant,  $T$  the temperature and  $j_0$  the exchange current density at the thermodynamic equilibrium.  $E$  and  $j$  are directly collected by the potentiostat and  $2.303RT/(\alpha n_\alpha F)$  corresponds to the Tafel slope (positive value as  $j_0$  is smaller than  $j$ ).  $\eta$  the overpotential rather than  $E$  is used as Y-axis in Tafel plot since  $E^0$  slightly changes in the heavy system. However, determining  $j_0$  at the thermodynamic equilibrium results in the extrapolation of the Tafel slope over *ca.* 300 mV. Hence, we also determined the exchange current density at the onset potential (*i.e.* where the reaction starts, in practice), here referred at the onset current density (designated as  $j_1$ ), to reduce the imprecision in the KIE determination.

Rate constants and KIE that are calculated from (i) the onset and exchange current density and (ii) the kinetic current density have different electrochemical meaning as they are representatives of the rate determining step extrapolated from (i) the kinetic-controlled region where the Tafel slopes are determined and (ii) the mass transport-controlled region where the Koutechy-Levich is determined (see **Figure 3-1**). Here, kinetic current density, exchange current density and onset current density are designated as  $j_k$ ,  $j_0$  and  $j_1$  respectively. Corresponding rate constants have same subscripts, as  $k_k$ ,  $k_0$  and  $k_1$ . **Figure 3-1** shows the difference of these current densities. In light water system (0.5 M H<sub>2</sub>SO<sub>4</sub> in H<sub>2</sub>O, abbreviated as HH), the standard potential for oxygen reduction reaction is 1.229 V vs. the standard hydrogen electrode (SHE), while in heavy water system (0.5 M D<sub>2</sub>SO<sub>4</sub> in D<sub>2</sub>O, abbreviated as DD) it is 1.249 V vs. SHE<sup>37,40</sup>. For the standard potential of HD (0.5 M H<sub>2</sub>SO<sub>4</sub> in D<sub>2</sub>O) and DH (0.5 M D<sub>2</sub>SO<sub>4</sub> in H<sub>2</sub>O), the extreme conditions were used, *i.e.*

DH was considered as a pure D<sub>2</sub>O system and HD as a pure H<sub>2</sub>O system. Numerous researches<sup>76-77</sup> for hydrogen-deuterium exchange rate have been done in organic chemistry and biomedical areas showing that exchange rate of C-H to C-D and N-H to N-D is limited. But kinetic H/D exchange rate of hydronium ion in the heavy water system is still unknown. Hence, it is also investigated the effect of the solvent (H<sub>2</sub>O or D<sub>2</sub>O) and of the charge carrier (D<sup>+</sup> and H<sup>+</sup>) onto the KIE, by determining the KIE vs. HH for DH, HD and DD solutions.

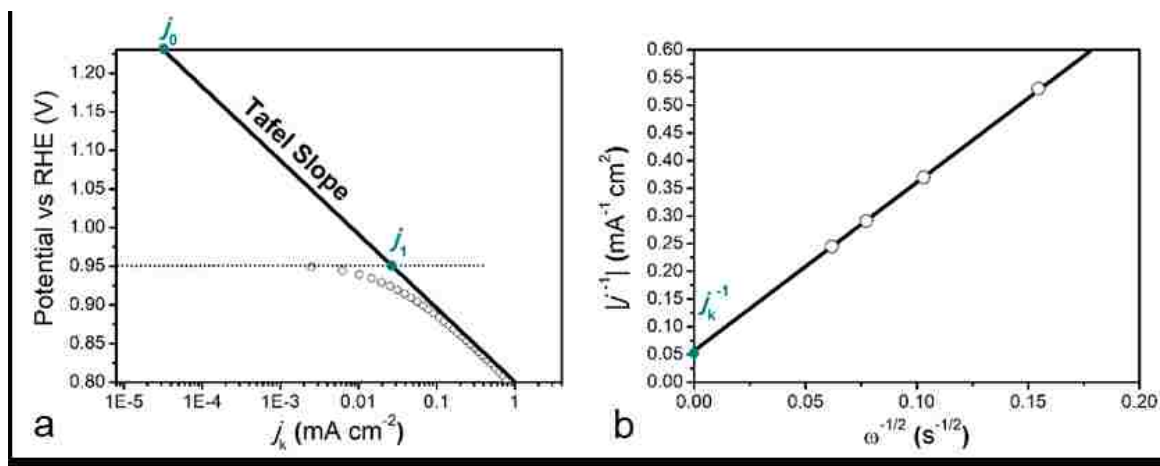


**Figure 3-1.** Diagrams of Koutecky-Levich and Tafel plots

(a) typical Tafel plot where exchange current density ( $j_0$ ) and onset current density ( $j_1$ ) are two different extrapolated points at the standard potential and (1.229 V vs. RHE in HH, 1.249 V vs. RHE in DD) onset potential respectively. (b) typical Koutecky-Levich plot measured at 0.425 V vs. RHE (*i.e.* in the mass transport-controlled region) where Y-intercept is the reciprocal of kinetic current density.

### Brief Physical Properties of FeNCB

M-N-C catalysts mainly consist of three categories by synthesis: macrocycle catalysts (such as porphyrin and phthalocyanine<sup>26, 78</sup>), metal-organic framework catalysts (*e.g.* zeolitic imidazolate framework<sup>27</sup>) and metal-nitrogen-carbon composite catalysts (for instance, polyaniline<sup>31</sup> and poly-aminopyridine<sup>32</sup>). They can be further divided into subcategories depending on whether pyrolysis is needed or not, graphitic degrees or pore size distribution, *et cetera*. Hence their physical properties differ significantly among different synthesis methods. Here, brief spectra of scanning electronic microscopy (SEM),



transmission electronic microscopy (TEM), XPS, X-ray diffraction (XRD) and infrared Raman for FeNCB that is researched in this chapter are given for comparison with other ORR Fe-N-C catalysts that were previously investigated via KIE<sup>39-40</sup>.

**Figure 3-2** provides detailed insights into the physicochemical properties of the FeNCB electrocatalyst used in this chapter. The material exhibits a highly porous structure (see **Figure 3-2a** and **3-2b**) with a specific surface of  $558 \text{ m}^2 \text{ g}^{-1}$ . The metal loading is of 0.08 at. %. According to the TEM (see **Figure 3-2c** and **3-2d**) and the XRD (see **Figure 3-2g**), the metals atoms are atomically dispersed, and the structure show a high graphitization level outside of the plane (as evidenced by the sharp graphite peaks for the (002) and (100) planes and the absence of Fe crystalline peaks). The in-plane crystallite size is  $L_a = 3.8 \text{ nm}$  (see **Figure 3-2h**). The C1s and N1s high resolution spectra determined by XPS (see **Figure 3-2e** and **3-2f**) present the typical features of carbonaceous materials with atomically dispersed Fe<sup>36</sup>. The morphology of the Fe-N-C electrocatalysts are extremely dependent of the synthesis processes<sup>79-80</sup>, hence making essential a thoughtful analysis of the materials physicochemical characteristics, to be later crossed to the observed mechanistic (*e.g.* KIE, *et cetera*).

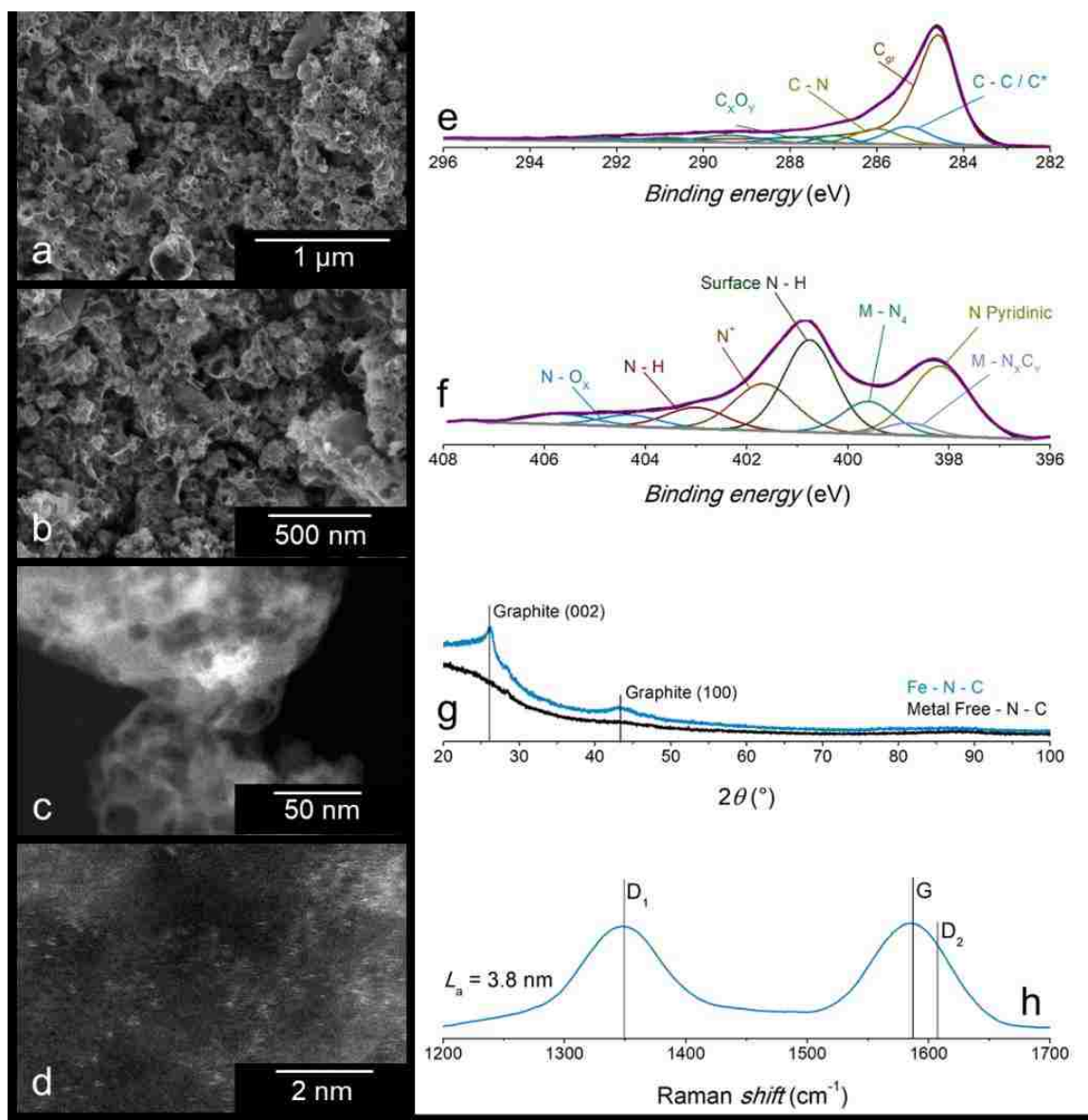


**Figure 3-2.** Assorted spectra of FeNCB  
 SEM micrographs in scale of (a) 1  $\mu\text{m}$  and (b) 500 nm. Dark field TEM micrographs of the Fe-N-C electrocatalysts in scale of (c) 50 nm and (d) 2 nm; XPS patterns in the (e) C 1s and (f) N 1s region; (g) XRD and (h) Raman patterns.

### Determination of Kinetic Rate and KIE

Linear sweep voltammetry (LSV) measurements have been done in four different electrolytes as previously described in Chapter 2, as HH, DH, HD and DD in sequence, without changing the working electrode and catalyst layer (but they were washed with

corresponding de-ionized light water or heavy water before starting the next series of experiment). **Figure 3-3** shows current density-potential LSV plots, with six rotation speed from 1000 rpm to 2000 rpm, 0.2 mg cm<sup>-2</sup> loading of FeNCB and 5 mV s<sup>-1</sup> scanning rate from 0.8 V to -0.2 V *versus* Ag/AgCl in 0.5 M corresponding acidic electrolyte.

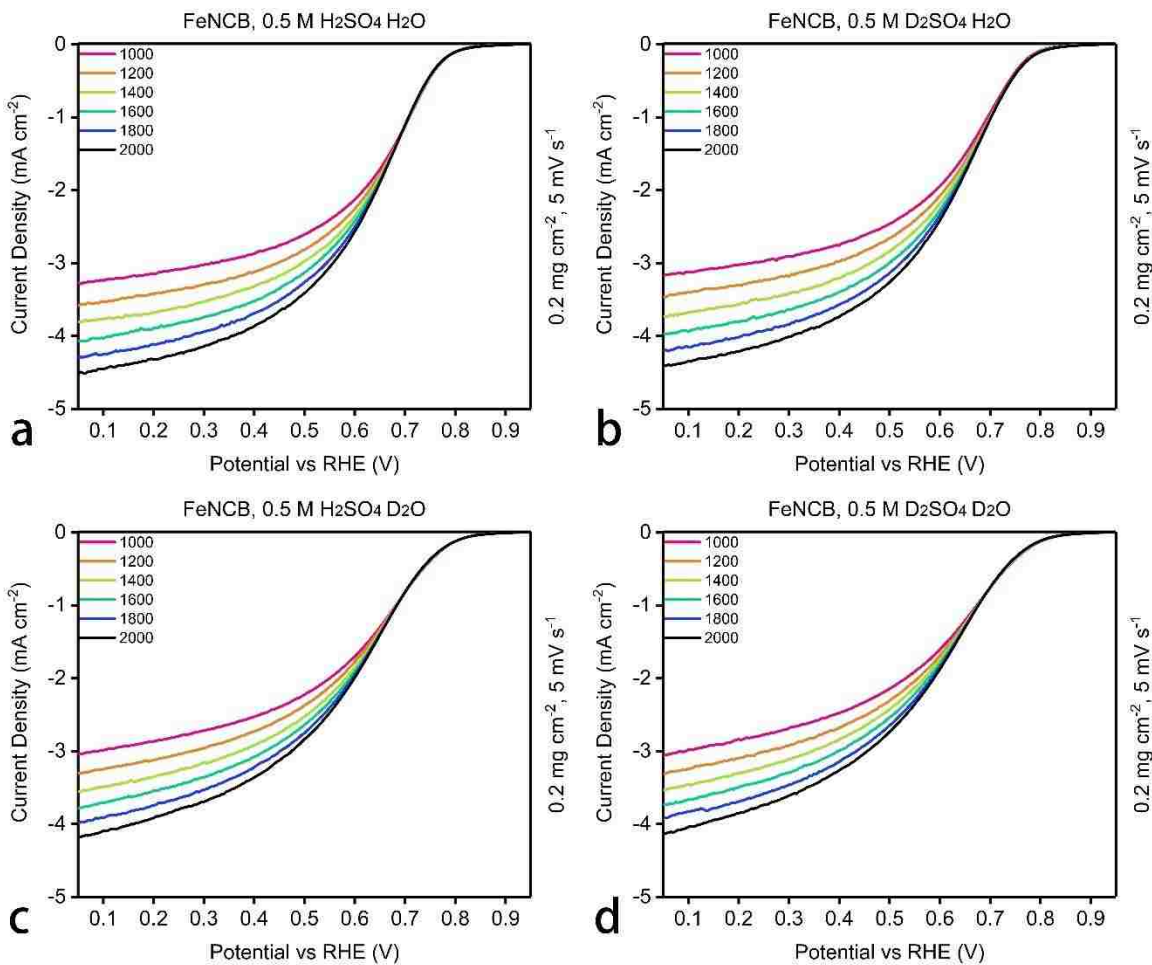


**Figure 3-3.** LSV plots of four electrolytes (a) HH (H<sub>2</sub>SO<sub>4</sub> H<sub>2</sub>O), (b) DH (D<sub>2</sub>SO<sub>4</sub> H<sub>2</sub>O), (c) HD (H<sub>2</sub>SO<sub>4</sub> D<sub>2</sub>O) and (d) DD (D<sub>2</sub>SO<sub>4</sub> D<sub>2</sub>O)

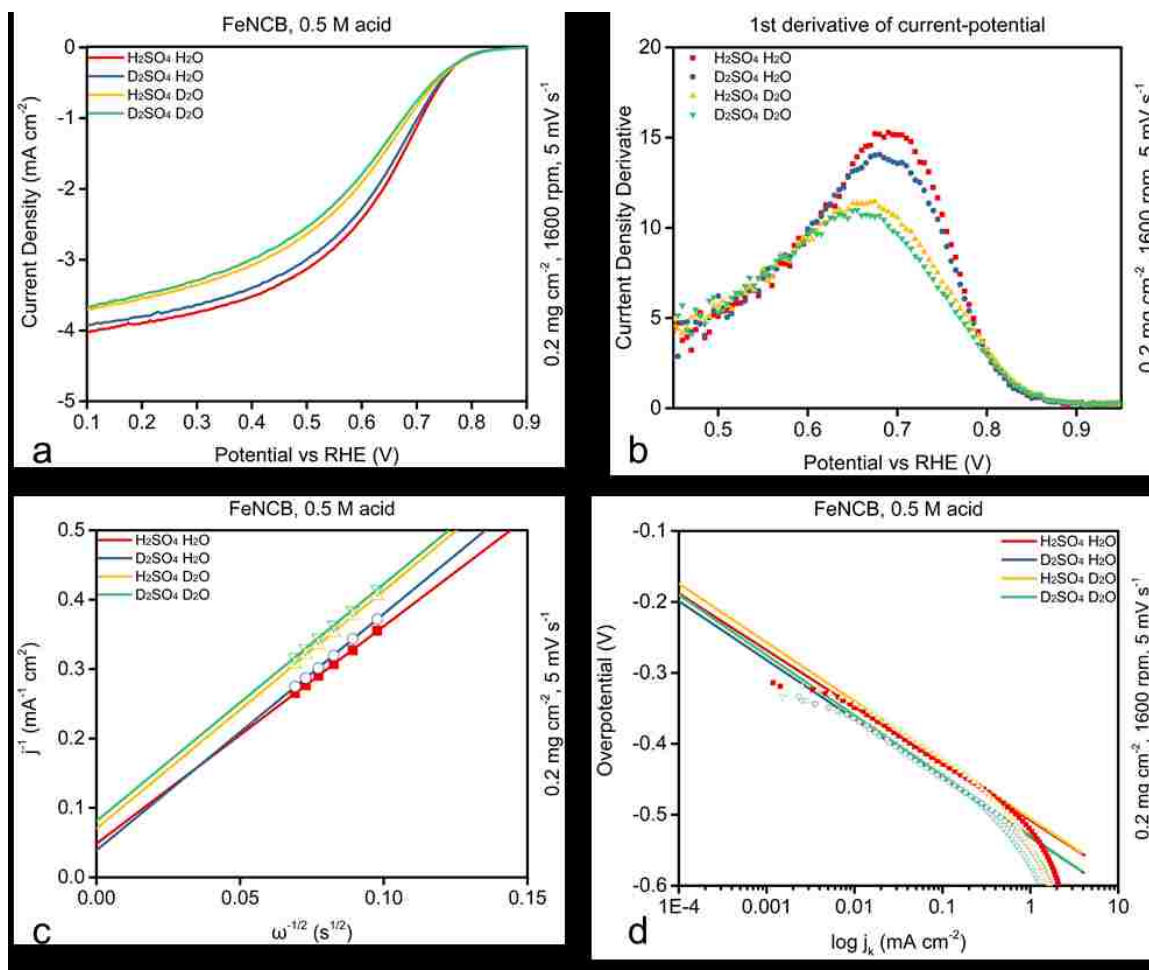


**Figure 3-4.** LSV, Koutecky-Levich and Tafel plots of four electrolytes

(a) comparison of LSV in four different O<sub>2</sub>-saturated electrolytes (HH, DH, HD, DD) at 1600 rpm (loading, 0.2 mg cm<sup>-2</sup>, scan rate 5 mV s<sup>-1</sup>). (b) 1st derivative of these four LSV. (c) Koutecky-Levich plots at 0.425 V vs. RHE and (d) Tafel plots.

**Figure 3-4** shows the corresponding comparison of LSV in four different electrolytes (HH, DH, HD and DD) at 1600 rpm and their 1<sup>st</sup> derivative curves where maximum points are regarded as half-wave potentials. The Koutecky-Levich plots were determined at 0.425 V vs. RHE for **Figure 3-4**. The diffusion current densities and half-wave potentials could be divided into light water group and heavy water group, while hydrogen ion and deuterium ion give less impact than the change of solvents. The diffusion current densities at 0.425 V vs. RHE are around 3.4 mA cm<sup>-2</sup> in HH, 3.3 mA cm<sup>-2</sup> in DH, 3.0 mA cm<sup>-2</sup> in HD and 2.9

mA cm<sup>-2</sup> in DD, respectively. The half-wave potentials are *ca.* 0.695 V vs. RHE in the light water system (the difference between H<sup>+</sup> and D<sup>+</sup> is negligible) and *ca.* 0.665 V vs. RHE in the heavy water system, with a decrease of ~ 30 mV. Hence, mass transport is influenced by the nature of the solvent. Interestingly, the product ratio of  $C_{O_2}D_{O_2}^{2/3}v^{-1/6}$  between light water and heavy water is around 1.02. Thus, the difference in diffusion current is not resulting from a difference in O<sub>2</sub> diffusion or saturation in solution between light and heavy water.

Electrolyte	KL a	KL b	KL R <sup>2</sup>	T a (mV dec <sup>-1</sup> )	T b	T R <sup>2</sup>
H <sub>2</sub> SO <sub>4</sub> H <sub>2</sub> O	3.13	0.048	0.99973	79.95	0.72	0.99917
D <sub>2</sub> SO <sub>4</sub> H <sub>2</sub> O	3.40	0.039	0.99969	83.09	0.71	0.99875
H <sub>2</sub> SO <sub>4</sub> D <sub>2</sub> O	3.42	0.070	0.99977	82.78	0.72	0.99937
D <sub>2</sub> SO <sub>4</sub> D <sub>2</sub> O	3.41	0.080	0.99973	84.93	0.71	0.99919

**Table 3-1.** Parameters of linear regression for Koutecky-Levich and Tafel plots

Here “a” represents slope and “b” represents Y-intercept in general form  $y = ax + b$ . Tafel slope is written as “-a” in unit of mV dec<sup>-1</sup> for easier comparison. R<sup>2</sup> represents the coefficient of determination for a predicted straight line, which is calculated as  $1 - \frac{\sum(y_i - f_i)^2}{\sum(y_i - \bar{y})^2}$ , where  $y_i$ ,  $f_i$  and  $\bar{y}$  are practical value, predicted value and arithmetic mean respectively.

The corresponding Koutecky-Levich plots and Tafel plots derived from **Figure 3-3** are given in **Figure 3-4c** and **3-4d**, with parameters of the slope, Y-intercept and R<sup>2</sup> (coefficient of determination) listed in **Table 3-1**. In Koutecky-Levich plots, four lines could be divided into two same groups as in LSV since the Y-axis is the reciprocal of the current density at 0.425 V vs. RHE. It can be found that DH, HD and DD have similar slopes while HH has a smaller one. Corresponding numbers of electrons are calculated as  $3.14 \pm 0.23$  in HH,  $3.05 \pm 0.23$  in DH,  $3.03 \pm 0.33$  in HD and  $2.99 \pm 0.23$  in DD respectively, as **Figure 3-5** shows, in addition to kinetic current densities which are used to calculate kinetic rates and kinetic isotopic effects. Corresponding exchange current densities at

standard potentials of ORR in different systems are shown in **Figure 3-6**, as well current densities at the onset potentials where ORR starts in practice.

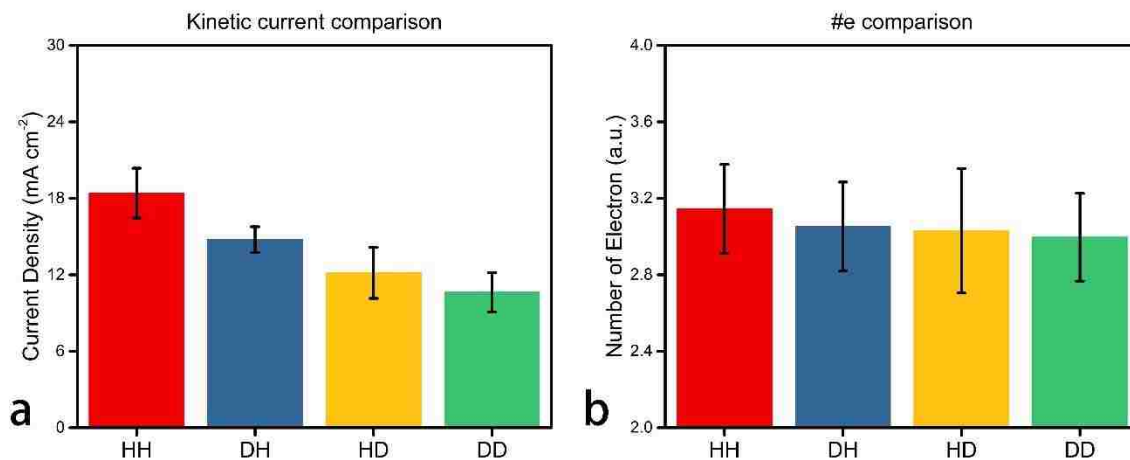


**Figure 3-5.** Results of Koutecky-Levich plots Comparison of (a) kinetic current densities and (b) numbers of electron.

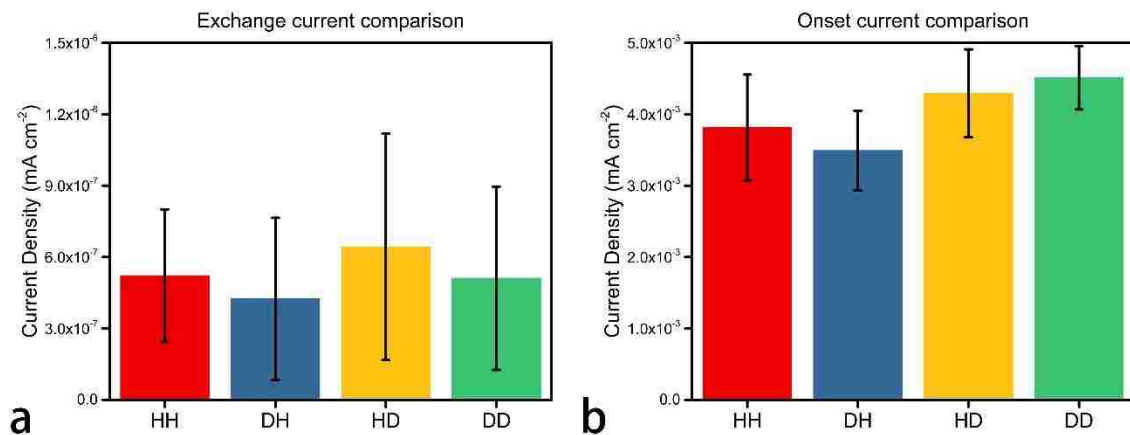


**Figure 3-6.** Results of Tafel plots Comparison of the exchange current densities at (a) the standard potential and (b) the onset potential.

The kinetic isotopic effect of  $1.92 \pm 0.11$  is calculated by comparing the kinetic rate of HH with DD at 0.425 V vs. RHE (see **Figure 3-7**). In Tafel plots, four lines could also be divided into two groups, *i.e.* HH and HD (the H<sup>+</sup> systems) and DH and DD (the D<sup>+</sup> systems). According to Malko *et al.*<sup>40</sup>, the standard potential for the ORR in D<sub>2</sub>O (with D<sup>+</sup> as a charge

carrier) is 20 mV higher than in H<sub>2</sub>O (with H<sup>+</sup> charge carriers). But the potential difference is not determined for a complex system such as HD and DH (thus, we used the extreme condition, *i.e.* HD behaves like a HH system and DH behaves like a DD system in terms of standard potential). Thus, to compare the KIE on HH, DD, HD and DH in the Tafel slope region, without being influenced by the change in the standard potential of the ORR, we calculated, in addition to the current exchange density ( $j_0$ ), the onset current density ( $j_1$ ), see **Figure 3-1** and **3-6**. In this experiment set, exchange current densities in four electrolytes are  $5.2 \pm 2.7$  in HH,  $4.2 \pm 3.4$  in DH,  $6.4 \pm 4.8$  in HD and  $5.1 \pm 3.9$  in DD (all in the unit of  $10^{-7}$  mA cm<sup>-2</sup>), resulting in a KIE =  $1.18 \pm 0.31$ , using  $j_0$  and a KIE =  $0.98 \pm 0.17$ , using  $j_1$  (see **Figure 3-7**). Interestingly, this value differs from the KIE value calculated by the Koutecky-Levich method, hence inducing different mechanisms (and rate determining steps) are involved between the kinetic-controlled region (0.7 – 0.9 V *vs.* RHE) and the mass transport-controlled region (0.425 V *vs.* RHE). It is also important to note that the KIE determined in the mass transport-controlled region correspond to the values reported by Tse *et al.*<sup>39</sup> ( $1.9 \pm 0.5$ ). Hence, the Fe-N-C electrocatalysts synthesized by different methods suffer from the same limitations in this potential region and this limitation involves the H<sup>+</sup> species. This can be induced either by (*i*) a change of mechanism toward an enhanced 2-electron pathway<sup>81</sup> with a proton involvement in the rate determining step and/or (*ii*) a limitation induced by the surface-diffusion of protons toward the active sites of the Fe-N-C electrocatalyst, similar to what is observed in Pt/C electrocatalyst<sup>68</sup>. By opposition, the KIE in the kinetic-controlled region is highly different than reported by Malko *et al.* (*ca.* 3.4) thus underlining the fact that the mechanistic and proton-involvement in the rate determining step in the low overpotential region is greatly

dependent of the electrocatalyst physicochemical properties (*i.e.* presence of metallic nanoparticles, density of active sites, *et cetera*). Therefore, under specific synthesis conditions, a Fe-N-C electrocatalyst RDS for the ORR can be independent of the proton, as evidenced here. In addition to the classic KIE determination (see **Equation 3-12**), **Figure 3-7** also feature the ‘partial’ KIE, *i.e.* HH/HD and HH/DH, determined in the Tafel slope potential range ( $j_0$  and  $j_1$ ) and at 0.425 V *vs.* RHE, via the Koutechy-Levich equation ( $j_k$ ). Two interesting features can be extracted from **Figure 3-7**: 1) the KIE determined via the Koutechy-Levich equation decreases when going from HH/DD to HH/HD and HH/DH (the KIE for HH/HH being 1). This phenomenon can be explained by the following hypothesis: The  $H^+$  and  $D^+$  transport in aqueous solution is driven by the Grotthuss mechanism, *i.e.* the  $D^+/H^+$  ‘jumps’ from one  $D_2O/H_2O$  to the other (In the three described solutions, DD correspond to  $D^+$  in  $D_2O$ , HD to  $H^+$  in  $D_2O$  and DH to  $D^+$  atoms in  $H_2O$ ). Hence, if we assume that the transfer of  $D^+$  to  $H_2O$  and the transfer from  $H^+$  to  $D_2O$  is fast: (i) only  $D^+$  ‘jumps’ in the DD solution; (ii) as  $c_D \gg c_H$  (*i.e.* concentration of D element  $\gg$  concentration of H element) in the HH/HD solution,  $D^+$  carry most of the charge in the HH/HD solution and, (iii) in the HH/DH solution, where  $c_H \gg c_D$ ,  $H^+$  will do the same. The element of the solvent is responsible for the charge carrying. If this hypothesis is correct, this confirms the involvement of the protons into the RDS in the mass transport-controlled region, as, by gradually replacing  $H^+$  by  $D^+$  (HH  $\rightarrow$  DH  $\rightarrow$  HD  $\rightarrow$  DD), an increase of the KIE is observed. 2) the KIE determined by the onset and exchange current densities remains of *ca.* 1 for the partial ‘KIE’. The only outlier is the KIE determined by the exchange current density for the HH/DH, which is ascribed either to (a) the imprecision of the determination of the KIE using this method, because of the large Tafel slope



extrapolation (see the large standard deviation,  $2.25 \pm 1.25$ ) or to (b) a non-negligible influence of the H<sub>2</sub>O solvent onto the value of the ORR standard potential (as, for DH, the standard potential is assumed to be 1.249 V vs. RHE, *i.e.* the potential in presence of D<sup>+</sup>/D<sub>2</sub>O), therefore impacting the value of  $k_0$  and, consequently, the KIE.

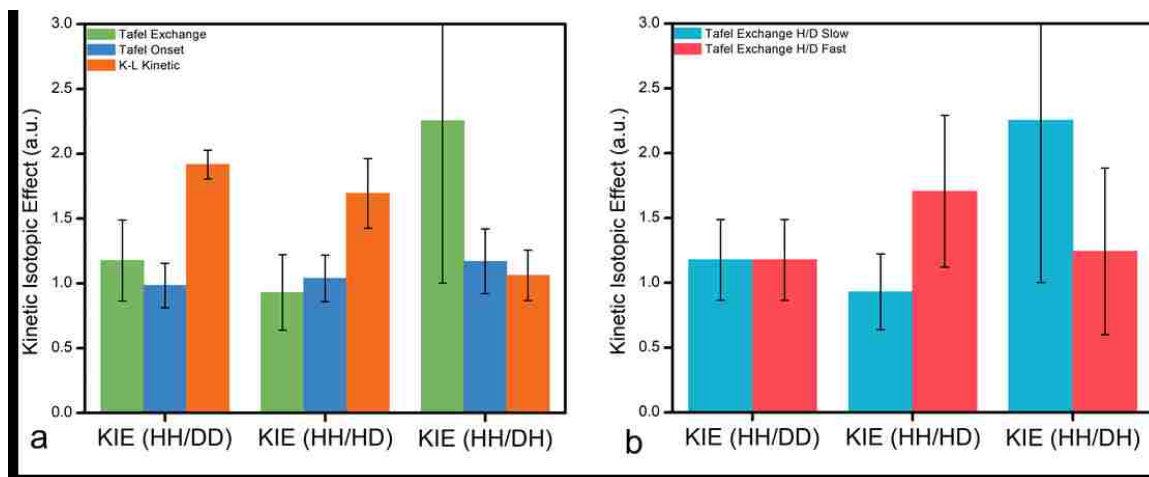


**Figure 3-7.** Kinetic isotope effects

(a) Legends represent KIE calculated via Tafel plot derived exchange current density ( $j_0$ ), Tafel plot derived current density at on.set potential ( $j_i$ ) and Koutecky-Levich plot derived kinetic current density ( $j_k$ ) respectively. (b) Determination of the KIE based on the hypothesis that the H/D exchange rate in the DH and HD system is slow, hence the standard potential of the ORR is constant or fast, *i.e.* the DH is considered as pure HH and the HD as pure DD systems.

To obtain better insights on the KIE observed in the mass transport-controlled region and to assess whether it was induced by the proton surface diffusion or in a change in mechanism toward a proton limited rate-determining step, we extrapolated the KIE from the Koutecky-Levich plots at several potentials, *i.e.*  $0.175 \text{ V} \leq E \text{ vs. RHE} \leq 0.575 \text{ V}$ . The results are presented in **Figure 3-8**. In this potential range, the KIE slightly increases from  $1.76 \pm 0.36$  at  $0.175 \text{ V vs. RHE}$  to  $2.14 \pm 0.30$  at  $0.575 \text{ V vs. RHE}$ . This trend corresponds to the trend in H<sub>2</sub>O<sub>2</sub> yield recently reported by our group (see Chen *et al.*<sup>82</sup>), *i.e.* an increase in H<sub>2</sub>O<sub>2</sub> yield from  $0.1 \text{ V vs. RHE}$  to  $0.5 - 0.6 \text{ V vs. RHE}$ , followed by a sharp decrease to reach H<sub>2</sub>O<sub>2</sub> yield = 0 at  $0.7 - 0.8 \text{ V vs. RHE}$ . If the large standard deviation (see **Figure 3-**

8) avoids a definitive conclusion, this result points toward the fact that the KIE observed in mass transport-controlled region results from involvement of the proton in the RDS of the  $O_2 \rightarrow H_2O_2$  mechanism. Further researches will focus on the identification of the active sites that are affected by the KIE, by working with metal free-N-C electrocatalysts and inhibiting the active iron sites – and the proton surface diffusion.

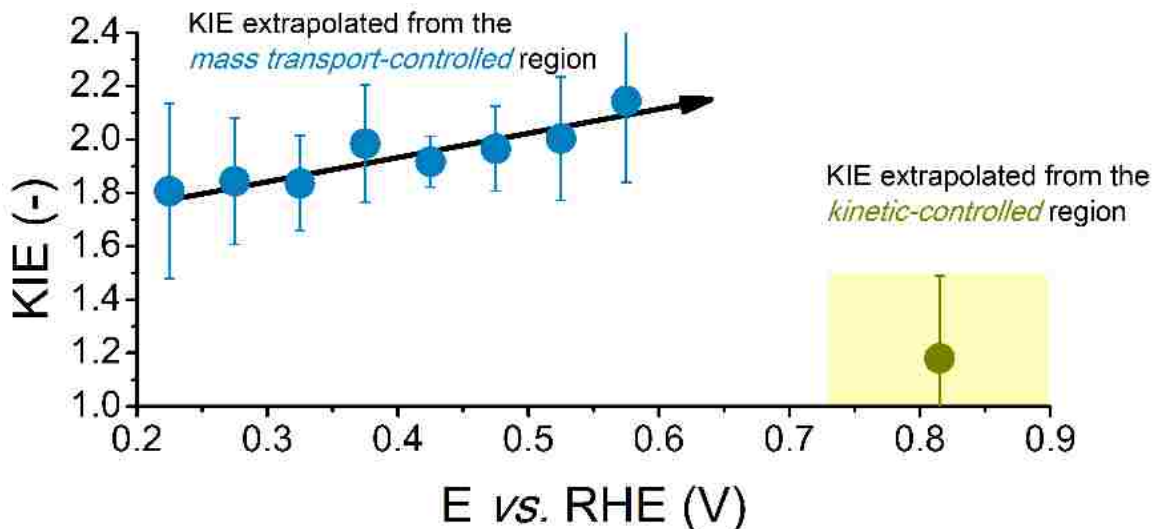


**Figure 3-8.** Kinetic isotope effects (HH/DD) extrapolated at different potentials (i) from the Koutechy-Levich plots (in blue, from 0.175 V vs. RHE to 0.575 V vs. RHE) and (ii) from the Tafel plot (in gold, the Tafel plot being linear from 0.730 V vs. RHE to 0.9 V vs. RHE).

## Chapter Conclusion

In this report, we investigated the kinetic isotopic effect (KIE) of a FeNCB electrocatalyst for the oxygen reduction reaction (ORR) extrapolated from the mass transport-controlled region (at 0.425 V vs. RHE, by the Koutechy-Levich method) and the kinetic-controlled region (0.7 – 0.9 V vs. RHE), to investigate the proton involvement in the rate-determining step (RDS). In the mass transport-controlled region, a KIE of *ca.* 2 was obtained, hence evidencing that in this potential range, the proton is limiting the reaction. This was confirmed by investigating the KIE (vs. 0.5 M  $H_2SO_4$  in  $H_2O$ ) in 0.5 M  $H_2SO_4$  in  $D_2O$  and

0.5 M D<sub>2</sub>SO<sub>4</sub> in H<sub>2</sub>O. By extrapolating the KIE from the Koutecky-Levich plots at different potentials ( $0.175 \text{ V} \leq E \text{ vs. RHE} \leq 0.575 \text{ V}$ ), we evidenced that the proton limitation was induced by a change in mechanism, leading to a higher peroxide yield ( $\text{O}_2 \rightarrow \text{H}_2\text{O}_2$ ) and, thus, that the proton was involved in the RDS of this reaction. For the Fe-N-C electrocatalyst described in this work (*i.e.* highly graphitic, without metallic particles and with atomically dispersed Fe-N<sub>x</sub> sites), no KIE was observed in the Tafel region, hence evidencing that, for this specific kind of non-precious metal group electrocatalyst, the RDS at low overpotential is proton independent, therefore implying that, by carefully optimizing the structure of Fe-N-C materials, Pt-like performances might be reached.

### **Alternate Explanation of KIE with Approximation**

Contents below and corresponding data are not published.

As described previously, both Koutecky-Levich and Tafel methods need long extrapolation from the datapoints collected. In addition, these data points and corresponding linear regression are limited by the accuracy of potentiostat used for LSV. In statistics, a small change of slope may still result in reasonable fitting but lead to a huge difference of intercept after extrapolation. If the slopes of Koutecky-Levich or Tafel plots were considered unchanged among four light water and heavy water systems, the extrapolated results and corresponding KIE values might become thoroughly different.

KIE values that are calculated on unchanged slopes from Koutecky-Levich plots or Tafel plots were shown in **Figure 3-9**. It can be found that KIE values derived from Tafel onset current densities and Koutecky-Levich kinetic current densities are similar with the ones from conventional mathematical optimum (see **Figure 3-7**), while corresponding standard deviations are larger. This consistency implies that proton dependence in the mass

transport-controlled region and proton independence in the kinetic-controlled region may correspond more to the structure and property of the catalyst itself, *i.e.* iron active sites which dominate onset potential are proton independent while nitrogen active sites are proton-dependent.

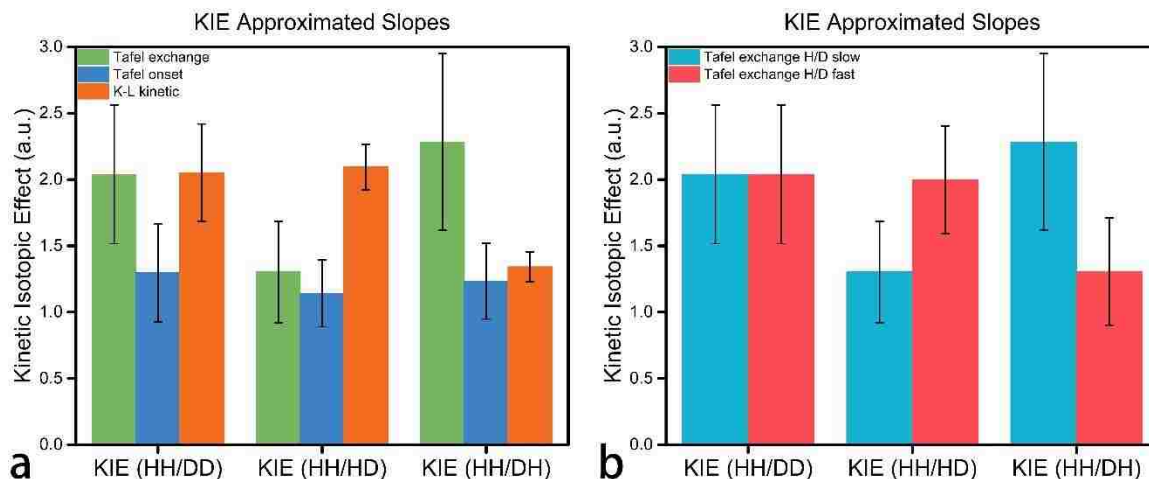


**Figure 3-9.** Kinetic isotope effects via approximated slopes

(a) Legends represent KIE calculated via Tafel plot derived exchange current density ( $j_0$ ), Tafel plot derived current density at onset potential ( $j_1$ ) and Koutecky-Levich plot derived kinetic current density ( $j_k$ ) respectively, with approximation that all slopes keep same in Koutecky-Levich or Tafel plots. (b) Determination of the KIE based on the hypothesis that the H/D exchange rate in the DH and HD system is slow, hence the standard potential of the ORR is constant or fast, *i.e.* the DH is considered as pure HH and the HD as pure DD systems

However, KIE values derived from exchange current densities and based on approximation are much higher, reaching *ca.* 2 in contrast to around 1.2 for mathematical optimum. Considering that KIE value derived from onset potential (*i.e.* kinetic-controlled region) is about 1.3 in this approximation, the physical meaning of same slopes in light water and heavy water systems could be explained that iron active sites and nitrogen active sites have same probability to get protons when the ORR stage is near thermodynamic equilibrium, regardless of proton dependence. When the reaction stage achieves more to kinetic-controlled region, the faster rate on iron active sites make total KIE nearer to 1. To confirm

whether this slope approximation is reasonable or not, more DFT calculation on the standard potential for nitrogen active sites is needed.

### **Extra Exploration Experiments**

Though nitrogen atoms that directly complex with iron to form Fe-N<sub>x</sub> don't exist in metal-free case, it is still possible to obtain the KIE values for pyrrolic / hydrogenated nitrogen and pyridinic nitrogen active sites by using N-C electrocatalyst synthesized from the same precursor. **Figure 3-10** shows corresponding LSV, 1st derivative, Koutecky-Levich plots and Tafel plots of NCB catalyst. Compared to FeNCB (see **Figure 3-4**), the diffusion current densities in H<sub>2</sub>SO<sub>4</sub> / H<sub>2</sub>O system are also around 4 mA cm<sup>-2</sup> but the half-wave potential is only *ca.* 0.55 V vs. RHE. In a heavy water system, the half-wave potential has a larger drop of about 50 mV, achieving around 0.50V.

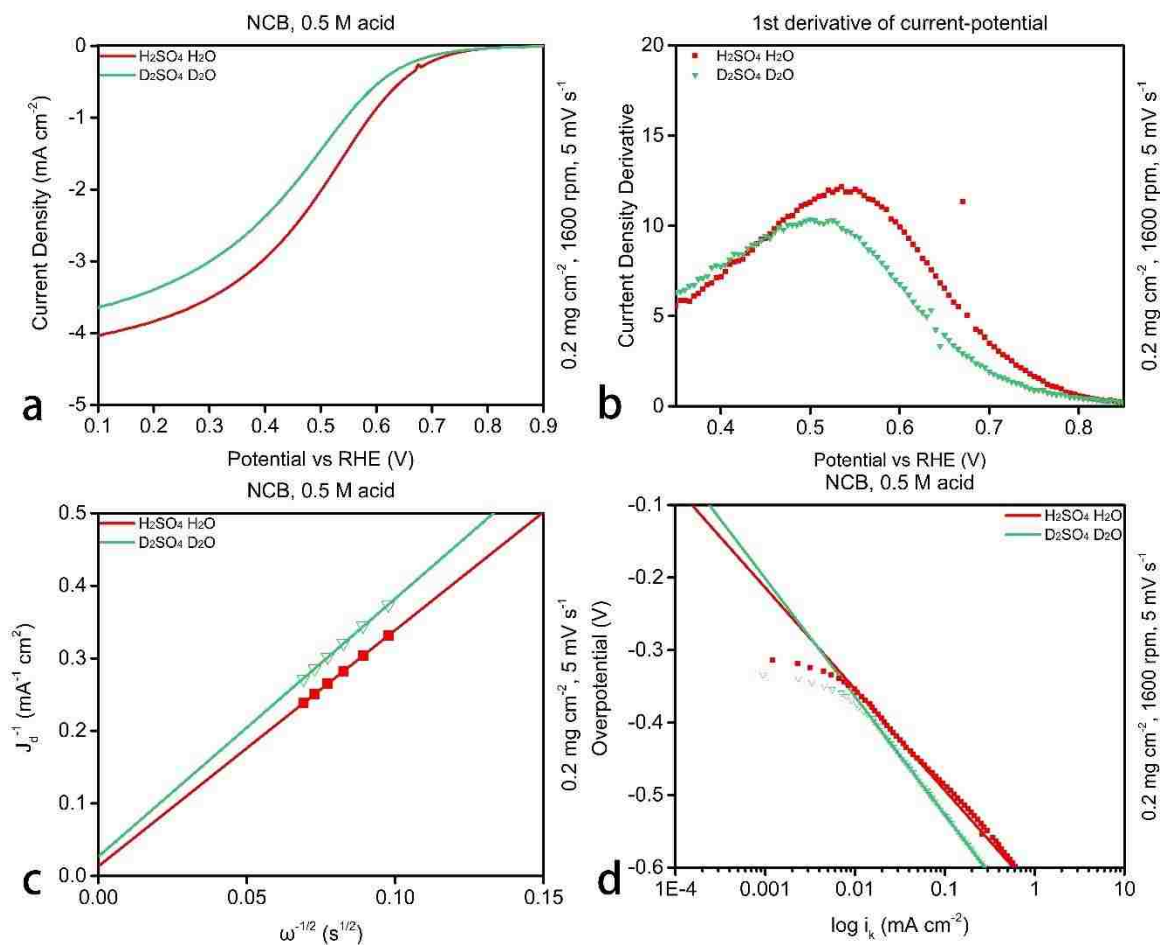


**Figure 3-10.** LSV, Koutecky-Levich and Tafel plots for NCB

(a) LSV, (b) 1st derivative of LSV, (c) Koutecky-Levich plots and (d) Tafel plots.

For Koutecky-Levich plots, KIE derived from the mass transport-controlled region is about 2.2 which is very similar to the one for FeNCB in the same region. This phenomenon indicates a similar proton dependence for nitrogen active sites. However, Tafel plots have thoroughly different behaviors. In the light water system, the corresponding Tafel plot could be obviously divided into two sections, one in low overpotential range from -0.35 V to -0.45 V with a slope of 139 mV dec<sup>-1</sup> and the other one in high overpotential range from -0.45 V to -0.55 V with a slope of 124 mV dec<sup>-1</sup>. According to previous Tafel research<sup>83-</sup>  
<sup>84</sup>, the slope around 120 mV dec<sup>-1</sup> means that rate-determining step is still the 1st charge

transfer. But when the slope increases to 140 mV dec<sup>-1</sup>, other effects such as adsorption of proton becomes more important and dominant. In a heavy water system, there is only one section in the Tafel plot, but the Tafel slope reaches 162 mV dec<sup>-1</sup>, implying that the RDS is still not the charge transfer. Hence, KIE values derived from the kinetic-controlled region for both onset current densities and exchange current densities are not meaningful for comparison with the ones for FeNCB. Because of that, it is essential to test KIE values of nitrogen active sites using Fe-N-C catalyst but with iron active sites inhibited (by molecule or other factors).

In addition, effective diffusion coefficients in light water and heavy water are calculated from the experiment data to be compared to the values from reference, as the porosity of the electrode layer may result in a non-negligible deviation. As shown in **Equation 3-9 & 3-10**, the diffusion coefficient  $D$  can be written as a function of the number of electrons  $n$  since the mass transport current density could be derived by the slope of Koutecky-Levich plot, as listed below:

$$D_{O_2} = \left( \frac{1/slope}{0.62nFC_{O_2}v^{-1/6}} \right)^{3/2} \quad \text{Eq. 3-15}$$

$$D_{O_2} = \left( \frac{1/slope}{0.62FC_{O_2}v^{-1/6}} \right)^{3/2} n^{-3/2} \quad \text{Eq. 3-16}$$

Corresponding plots are shown in Figure 3-11, with horizontal lines to indicate the referred values used in previous KIE calculations. It is found in both systems that the effective diffusion coefficients change more significantly when #e is near 2. The range of  $D$  is  $1.5 \times 10^{-5} \text{ cm}^2 \text{ s}^{-1}$  for #e being 2-3, while it is just *ca.* 0.5 when the number of electrons is larger than 3. In addition, the difference of  $D$  in two system decreases with the increase of #e. Because of this, if the number of electrons keeps the same in two systems, the effective diffusion coefficient in heavy water needs to be smaller than the referred value. When the

loading of catalyst is high (*e.g.*  $0.6 \text{ mg cm}^{-2}$ ), more in-plane active sites and the porosity will limit the mass transport of oxygen and proton, making the numbers of electrons in two systems nearer to each other. Hence, lower loading of catalyst and smaller porosity of electrode layer will make the results of Koutecky-Levich plot more accurate.

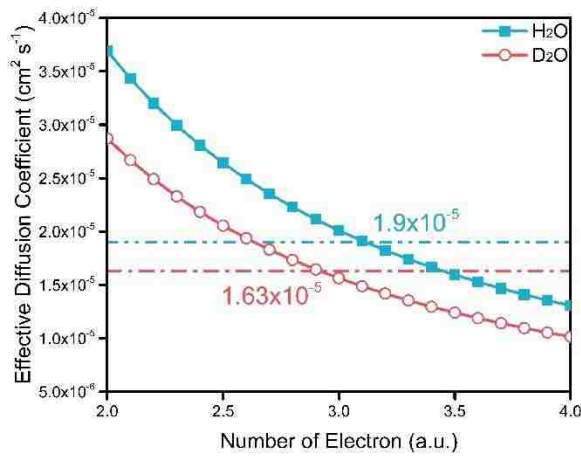


**Figure 3-11.** Effective diffusion coefficient of  $\text{O}_2$  as a function of #n  
Blue and red lines are light and heavy water system separately. Horizontal lines are corresponding values from references.



## Chapter 4

### **Inhibition of Active Sites with Nitrogen-Contained Chemical**

The contents in this chapter have been published as “Inhibition of Surface Chemical Moieties by Tris(hydroxymethyl)aminomethane: A Key to Understanding Oxygen Reduction on Iron–Nitrogen–Carbon Catalysts” in ACS Applied Energy Materials<sup>82</sup>. Co-authors are Kateryna Artyushkova, Santiago Rojas-Carbonell (Synthesis), Alexey Serov, Ivana Matanovic (DFT), Carlo Santoro, Tristan Asset (Pt/C electrochemistry tests) and Plamen Atanassov.

#### **Introduction – Inhibition of ORR Catalysts**

As described in the introduction chapter, most previous researches for the poisoning or inhibition of Fe-N-C catalyst start from inhibitor chemical of a platinum catalyst, or from poison chemical of hemoglobin or similar iron-centered proteins. This result in a selection of assorted chemicals that are environmentally harmful or difficult to operate. In addition, these inhibitors are not considered to be removed from the surface of the catalyst, or to selectively adsorb on specific active sites like pyridinic and pyrrolic nitrogen, leading to a limited understanding on distinguishing assorted active sites.

Recent studies on Fe-N-C inhibition start focusing on specific chemicals that catalysts may encounter in their working environment, reversibility and neutralization of inhibitors, as well as recoverable inhibition routes for quantification. Hu *et al.*<sup>85</sup> investigated inhibition of phosphoric acid, perchloric acid, sulfuric acid and hydrochloric acid, which are either common acid or working electrolyte in a fuel cell. Chung *et al.*<sup>86</sup> gave the information of irreversibility and reversibility for cyanide inhibition and its neutralization with perchlorate.

Malko *et al.*<sup>87</sup> reported nitrite inhibition with electrochemical stripping to quantify iron active sites.

In this chapter, we report the use of tris(hydroxyl-methyl)-aminomethane (Tris) as a specific molecular probing agent of active sites in Fe-N-C catalysts<sup>82</sup>. Two catalysts, one metal-free (N-C) and one metal-containing (Fe-N-C), were fabricated by identical synthetic procedure from the same carbon-nitrogen precursor, aminoantipyrine (AAPyr), without and with Fe salt (AAPyr and FeAAPyr, respectively)<sup>88-90</sup>. Study of inhibition and recovery of metal-containing catalysts in the acidic and alkaline electrolyte and comparison between metal-free and metal-containing PGM-free catalysts allowed us to correlate the nature of their active sites with individual steps of oxygen reduction reaction.

### DFT Calculation on Adsorption Energy of Tris

DFT calculation on adsorption energy could reveal what chemical could be most possible to be adsorbed on the surface of a specific active site, including platinum, nitrogen and iron. Corresponding results are listed in **Table 4-1**. Corresponding DFT geometries are listed in **Figure 4-1**. It is found that  $pK_a$  of Tris is 8.07 which indicates it exists as a protonated form (designated as TrisH) in acidic media, and deprotonated form in alkaline media. As reported previously<sup>36, 91</sup>, iron active sites undergo 4-electron or 2-electron mechanism, while nitrogen active sites (graphitic, pyrrolic, hydrogenated pyridinic) undergo 2-electron mechanism, in addition to the reduction of peroxide to water by pyridinic-N active site. **Figure 4-1** shows these active sites as defects with TrisH adsorbed in acidic media.

Active Site	TrisH	Tris	O2
Fe-N4	-1.96	-0.25	-1.01* to -1.43**

Fe-N2	-2.18		-1.68*
Graphitic-N	-1.07	-0.02	-0.13* to -0.41**
Pyridinic-N	-3.65	-0.41	-0.08* to -0.28**
Pyrrolic-N†	-0.53	-0.26	-0.21* to -0.25**
Pt (111)	-3.07		-0.44 to -0.81***

**Table 4-1.** Adsorption energy of Tris, TrisH and O<sub>2</sub> on active sites

All values are in unit of eV from DFT calculation. † It can also be described as hydrogenated pyridinic-N. \* Values are calculated using PBE (Perdew-Burke-Ernzerhof) functional<sup>92</sup>. \*\* Values are calculated using vdW-DF functional<sup>65</sup>. \*\*\* Values come from references<sup>93-95</sup>.

It can be found that the interaction energy between the Fe-N<sub>4</sub> site and Tris of -0.25 eV is significantly smaller than that of oxygen (see **Table 4-1**). Therefore, we assume that Tris form does not bind to metal-containing active sites and is not involved in the inhibition process, by opposition to TrisH (- 1.96 eV). From the comparison of the adsorption energies of TrisH and O<sub>2</sub> on different defects (**Table 4-1**), it can be concluded that TrisH has the strongest interaction with pyridinic-N and Fe-N<sub>x</sub> sites, followed by the graphitic-N and hydrogenated nitrogen defects (pyrrolic and hydrogenated pyridine). At the same time, only pyridinic nitrogen serves as a possible site for Tris binding that is strong enough to compete with the binding of oxygen. Fe-N<sub>x</sub> and pyridinic nitrogen are the most preferred sites for TrisH binding and for these sites the binding energy of TrisH is significantly larger than that of oxygen.

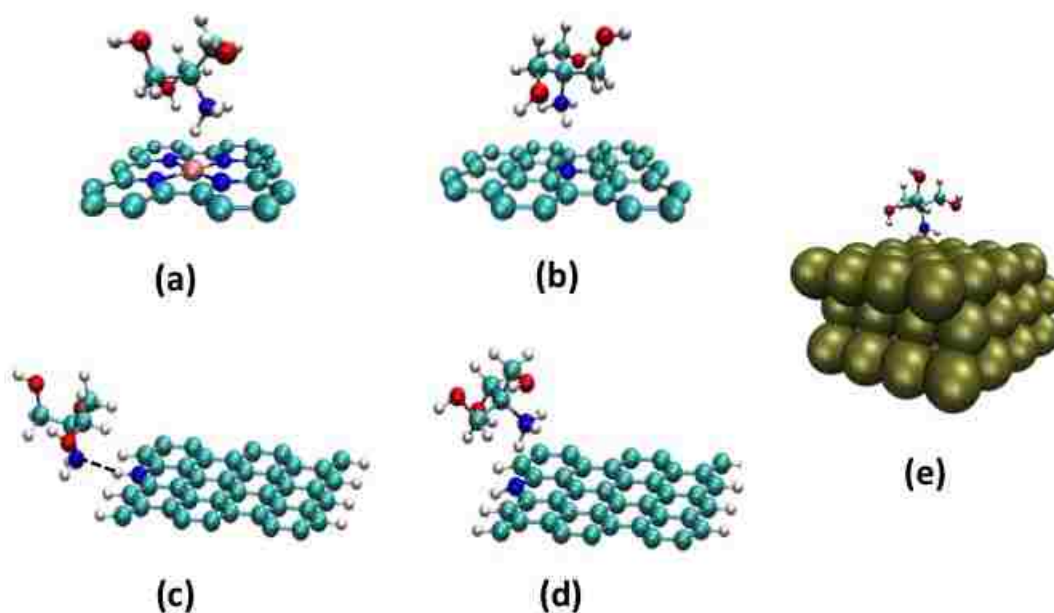


**Figure 4-1.** DFT optimized geometries of TrisH adsorption on active sites. Different active sites are (a) Fe-N<sub>4</sub>, (b) graphitic-N, (c) pyridinic-N, (d) hydrogenated pyridinic-N, and (e) Pt (111). Structure of Fe-N<sub>4</sub> represents a unit cell of this active site type.

## Results of Electrochemistry Tests

Electrocatalytic activity of FeAAPyr in the reaction of oxygen reduction was evaluated by Rotating Ring Disk Electrode (RRDE) in the 0.5M H<sub>2</sub>SO<sub>4</sub> and 1 M KOH (**Figure 4-2**). The information derived from linear sweep voltammograms (LSVs) as a function of Tris concentration is presented in **Figure 4-3**. LSV for commercial Pt/C was also acquired as a reference. According to DFT, there is a strong energy of adsorption between Pt and TrisH (-3.07 eV, see **Table 4-1** and **Figure 4-1e**), which is comparable to the energy of adsorption of TrisH to pyridinic N. In Pt/C where ORR occurs via direct 4e<sup>-</sup> mechanism, addition of TrisH causes very significant decreases in half-wave potential due to blockage of Pt sites by the absorbed inhibitor (**Figure 4-3e**), while limiting disk current decreases insignificantly at lower concentrations than 0.1 M and drops significantly at 0.8 M of Tris (**Figure 4-2c**). This indicates that at larger concentrations of Tris, *i.e.*, above 0.1 M, the

solubility of oxygen in the electrolyte decreases due to the increased concentration of inhibitor. This explanation is further supported by the negligible (and independent of the Tris concentration) ring current (**Figure 4-2f**). Indeed, this result confirms that the oxygen reduction reaction on Pt follows a direct  $4e^-$  pathway and that Tris addition does not have any effect on the hydrogen peroxide yield. Since the limiting current is dependent on the reactant concentration in solution and on the exchanged number of electrons. The constant value of the later confirms that Tris is decreasing  $O_2$  solubility in solution at concentrations above 0.1 M. Washing away Tris from the working Pt/C electrode results in full recovery of both half-wave potential and disk current at 0.2 V.

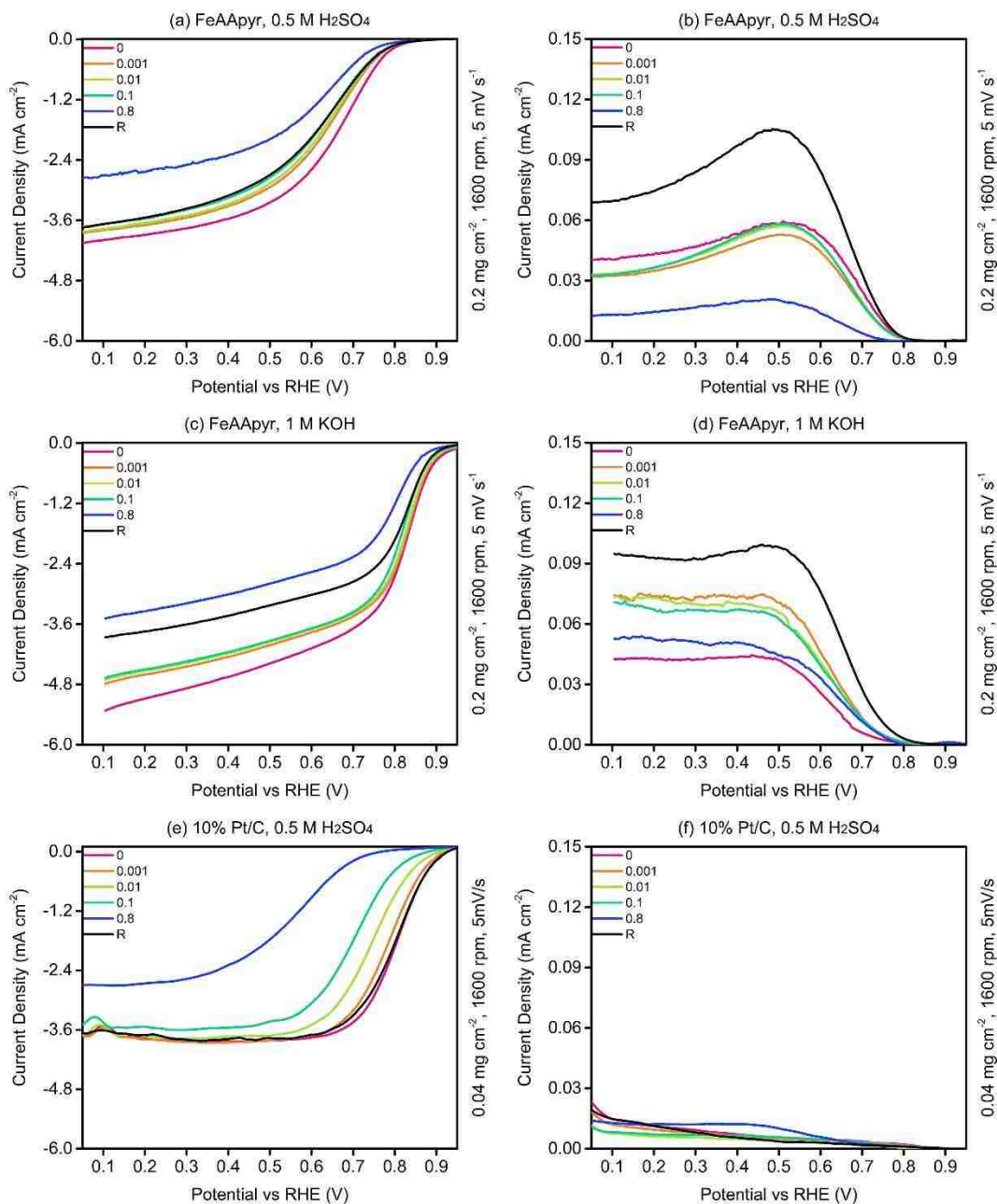


**Figure 4-2.** RRDE LSV of FeAAPyr, AAPyr and 10% Pt/C

(a)(c)(e) show disk current density versus potential, and (b)(d)(f) show ring current density versus potential, respectively. 0, 0.001, 0.01, 0.1 and 0.8 represents the sequential molar concentration of Tris in same electrolyte, while R means “refresh” or “recovery” by rotating electrode without changing catalyst layers in de-ionized water for 15 minutes.

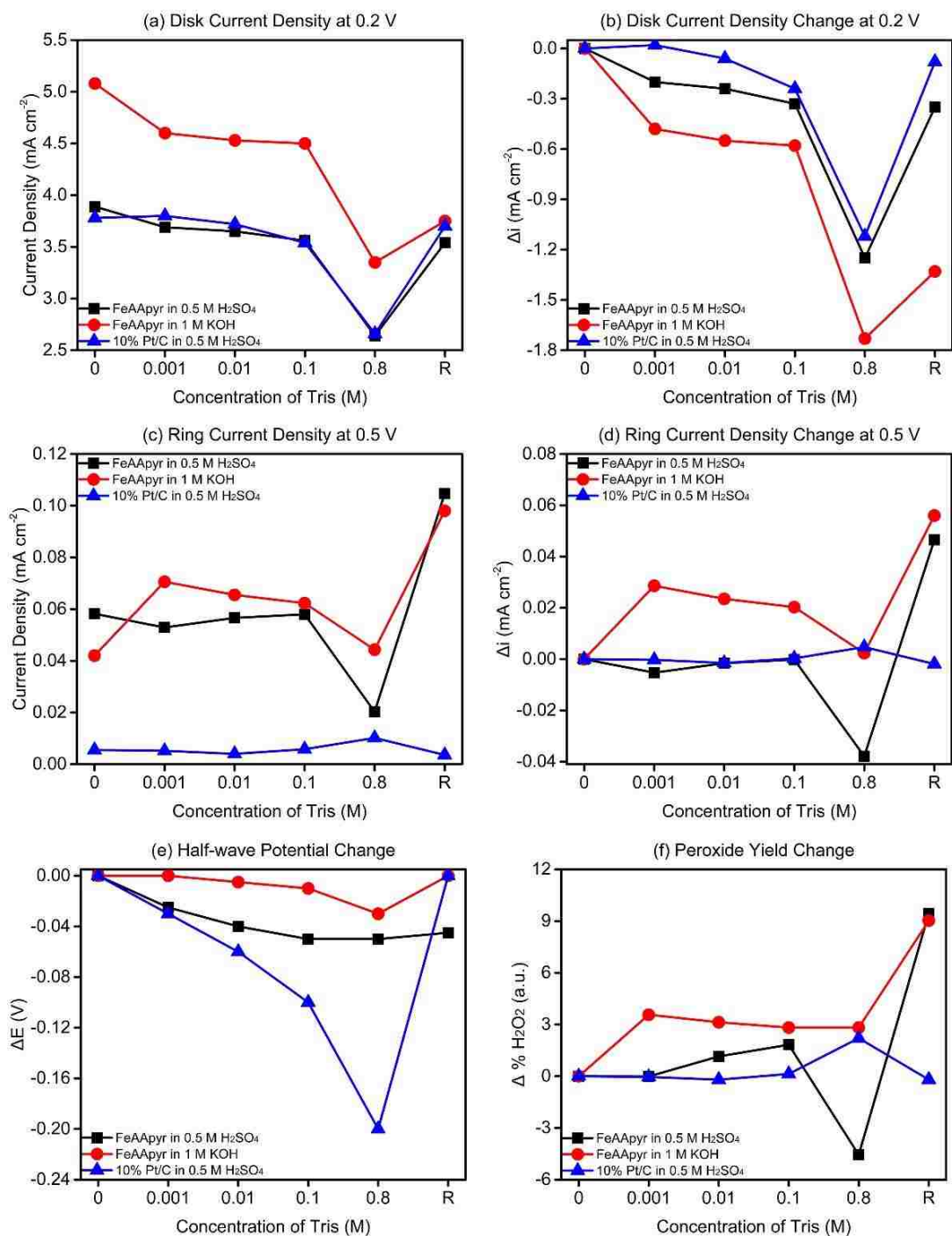


**Figure 4-3.** Secondary data from RRDE LSV

(a) Disk current densities at 0.2 V versus RHE, (b) Disk current change at 0.2 V, (c) Ring current densities at 0.5 V, (d) Ring current change at 0.5 V, (e) Half-wave potential change and (f) Peroxide yield change.

For FeAAPyr catalyst, the addition of even 0.001 M Tris to electrolyte results in 25 mV shift of half-wave potential to a lower value in acidic solution and no change in alkaline.

In acidic electrolyte, there is a 45 mV downshift in the half-wave potential at 0.1 M of Tris, but no further decrease in half-wave potential is observed when Tris concentrations were increased up to 0.8 M. The rate of change in half-wave potential is quite different in alkaline electrolyte (**Figure 4-3e**), where 0.1 M and 0.8 M Tris induce much smaller shift in half-wave potential of only 15 mV and 35 mV, respectively. The rate of decrease in the disk limiting current density is very similar for both acidic and alkaline solutions (**Figure 4-3b**) with maximum decrease observed for 0.8 M Tris concentration induced by the decreased solubility of oxygen (as observed on Pt/C), especially at high concentrations of an inhibiting agent. The larger effect on disk current density in alkaline media versus acidic even at low concentrations of Tris points to the higher solubility of Tris in alkaline electrolyte.

After washing the working electrode with de-ionized water, a very small increase in  $E_{1/2}$  (~5 mV) was registered in the acidic electrolyte, which indicates the irreversible inhibition of active sites participating in the ORR by the Tris added (**Figure 4-3e**). At the same time, the half-wave potential is almost fully recovered in alkaline media. However, in both cases, the diffusion limiting current for the “recovered” catalysts are lower than observed before Tris-addition. This is easily explained by the higher peroxide yield (**Figure 4-2b, 4-2d and Figure 4-3f**) that induces a decrease of the overall number of electrons exchanged during the reaction and, therefore, a diminished diffusion limiting current. Differences in peroxide yield arise from the addition of Tris, which results in drastically different behavior due to a different mechanism of oxygen reduction, particularly in the 1<sup>st</sup> step of oxygen reduction to hydrogen peroxide. A significant difference between ORR in acidic and alkaline media is based on an inner-sphere and outer-sphere mechanism. In alkaline media, surface



hydroxyl groups promote surface-independent outer-sphere electron transfer, while in acidic media immediate involvement of active sites such as metal coordinated to nitrogen in inner-sphere electron transfer is of direct relevance<sup>96-98</sup>.

In acidic media, Tris is present in its protonated form TrisH ( $pK_a = 8.07$ ); the addition of low concentrations of Tris, *i.e.*, between 1 mM and 0.1 M results in a similar decrease in a ring current due to TrisH inhibiting hydrogen peroxide producing sites. At large Tris concentration of 0.8 M, there is a significant decrease in hydrogen peroxide production due to a combination of decreased oxygen solubility and inhibition of  $H_2O_2$  producing sites by bound TrisH. However, after washing the working electrode, the ring current density increased from  $0.02 \text{ mA cm}^{-2}$  to  $0.10 \text{ mA cm}^{-2}$  at 0.5 V vs. RHE (**Figure 4-3c**). This phenomenon of hydrogen peroxide recovery after catalyst washing is a clear indication of Tris reversible weak binding to the active centers participating in the first step of the ORR mechanism. Moreover, DFT calculations show that the proton from TrisH is being transferred to pyridinic nitrogen due to the lower  $pK$  value of the pyridinic nitrogen (6.5 for pyridinic nitrogen and 8.06 for Tris molecule). The interaction energy between protonated pyridinic nitrogen, and Tris molecule is only -0.26 eV. In previous studies, protonation of pyridine has shown to inhibit oxygen reduction reaction<sup>51</sup>. Pyridinic nitrogen has shown to catalyze the second step of hydrogen peroxide reduction to water. This implies that after the catalyst washing, TrisH is removed, but pyridinic nitrogen remains in its protonated form, therefore, explaining the lower half-wave potential and higher hydrogen peroxide yield of the “recovered” catalysts compared to their “fresh” counterpart (**Figure 4-2a** and **4-2b**). Furthermore, based on the DFT results in **Table 4-1**,

TrisH can be more easily removed from protonated pyridinic nitrogen, pyrrolic nitrogen, and graphitic nitrogen, while Fe-N<sub>x</sub> sites may be irreversibly blocked by TrisH.

In alkaline media, Tris is present in its deprotonated form. DFT has shown competitive binding of Tris and oxygen to pyridinic nitrogen. Enhanced hydrogen peroxide generation at all concentrations of Tris is observed (**Figure 4-3f**). This can be attributed to the presence of Tris bound to pyridinic nitrogen within the outer Helmholtz sphere of the catalyst surface, which enhances the first step of oxygen reduction to peroxide<sup>97-98</sup>.

In conclusion, in an acidic electrolyte, TrisH interacts strongly with active sites that catalyze both complete and partial reduction of oxygen, and, therefore, it should inhibit both steps of ORR. As observed in the experiment performed in an acidic electrolyte, the addition of TrisH results in a decrease of both half-wave potential and the ring current confirming direct blocking of active sites for both complete and partial oxygen reduction by TrisH. In alkaline electrolyte, Tris can only competitively bind to pyridinic nitrogen which has been shown to catalyze the reduction of hydrogen peroxide to water<sup>36</sup>. The half-wave potential recorded in alkaline media is changed very slightly by the addition of Tris. However there is an enhancement of hydrogen peroxide production, observed experimentally when Tris is added to the alkaline electrolyte. One explanation could be that specific adsorption of Tris leads to selective blocking of pyridinic nitrogen moieties, which act as catalytic sites for hydrogen peroxide reduction to water. This effect of selective site blocking can be synergistic to a local increase of –OH groups in the proximity of Tris-bound to pyridinic nitrogen surface groups, which can be beneficial to oxygen reduction to hydrogen peroxide in alkaline electrolyte. In acidic electrolyte TrisH affects both partial oxygen reduction to peroxide and complete oxygen reduction to water, as

evidenced by the observation that both half-wave potential and the peroxide yield decrease for Tris concentrations exceeding 0.1 M. In contrast, in alkaline electrolyte Tris promotes the first step of reaction of producing hydrogen peroxide and inhibits the second step of H<sub>2</sub>O<sub>2</sub> reduction to water. This alternate effect on selectivity allows one to use Tris as a homogeneous, electrolyte based “titration agent” to selectively study kinetics of individual steps of ORR on various catalytically active moieties present in M-N-C catalysts.

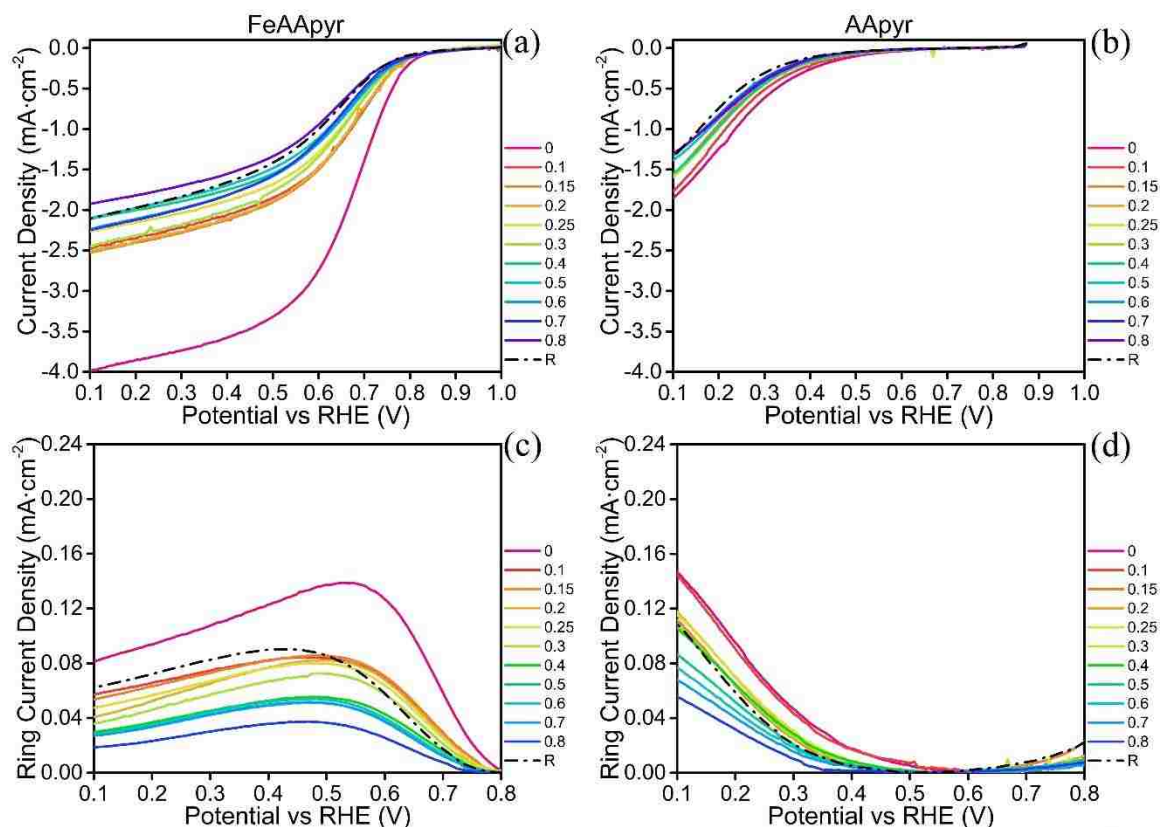


**Figure 4-4.** RRDE LSV data of Tris inhibition in HClO<sub>4</sub> (a & c) Fe-AApyr and (b & d) AApyr materials. Disk current density: (a) and (b). and Ring current density: (c) and (d).

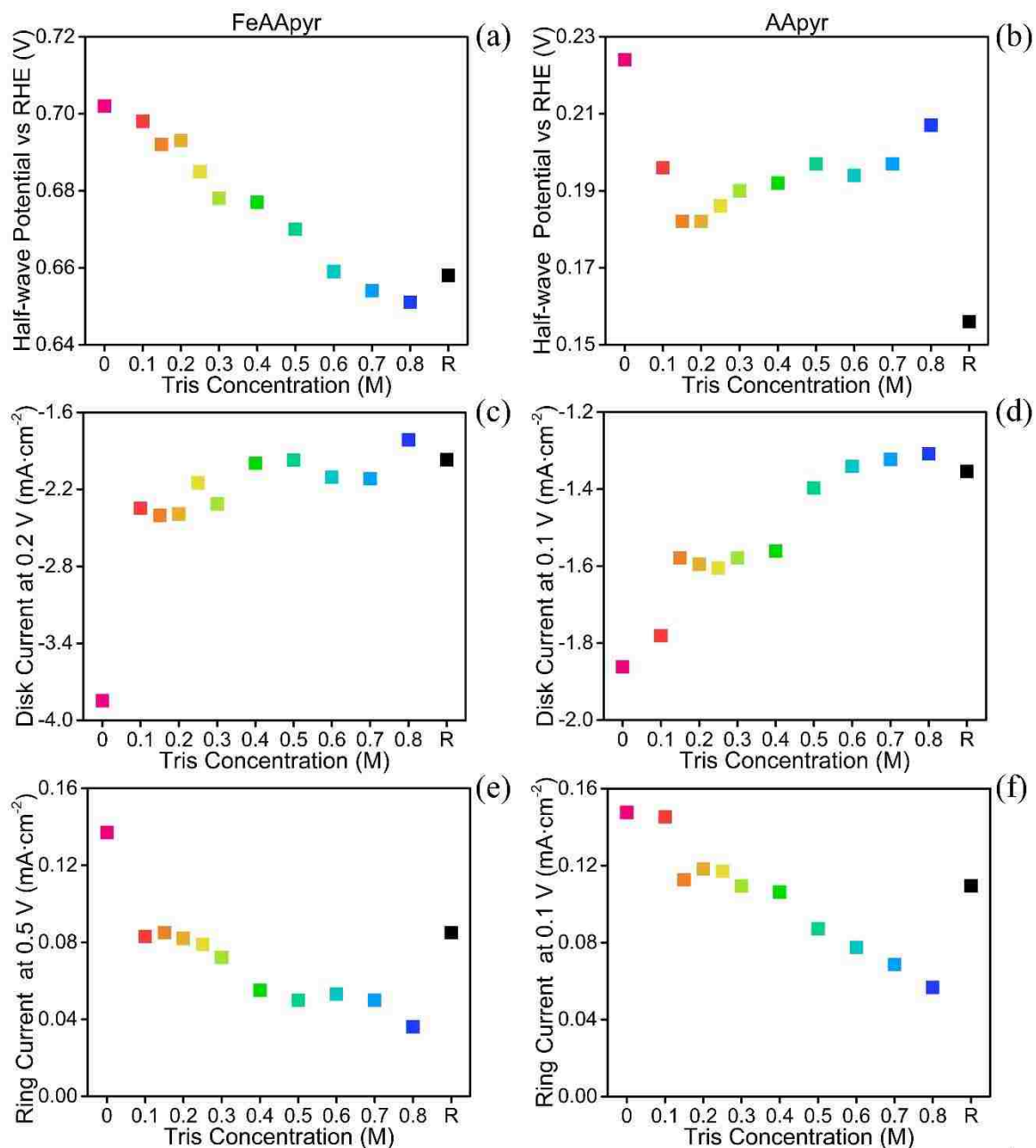


**Figure 4-5.** Secondary data of Tris inhibition LSV in  $\text{HClO}_4$ .

(a, c, e) FeAApyr and (b, d, f) AApyr: (a) half-wave potentials, (c) disk current densities at 0.2 V vs. RHE, (e) ring current densities at 0.5 V vs. RHE. (b), (d) and (f) give similar information for AApyr while the potential is at 0.1 V for disk current, ring current and hydrogen peroxide yield.

To address the role of metal on oxygen reduction mechanism we have tested inhibition of the electrocatalytic activity of FeAApyr and AApyr by Rotating Ring Disk Electrode (RRDE) method in the 1M  $\text{HClO}_4$  acidic electrolyte with the addition of Tris as the

inhibiting agent (**Figure 4-4**). The electrochemical information derived from linear sweep voltammetry (LSV) as a function of Tris concentration is presented in **Figure 4-5**. Like the experiments reported in **Figure 4-2**, in the case of FeAAPyr, the shift to lower values in half-wave potential with increasing concentration of Tris was observed (**Figure 4-5a**). When 0.8 M Tris is added to the acidic electrolyte, a similar shift of 50 mV is observed in both 0.5 M H<sub>2</sub>SO<sub>4</sub> and 1 M HClO<sub>4</sub>. Very insignificant recovery in half-wave potential indicates the irreversible inhibition of active sites participating in the ORR. After this initial decrease in ORR activity upon addition of 0.1 M Tris, increasing the Tris concentration resulted in the insignificant decrease of the limiting current density.

The similar set of experiments were performed with metal-free (AAPyr) electrocatalyst to discriminate further the active sites participating in ORR. It was found that upon exposure of metal-free catalyst (AAPyr) to Tris, both half-wave and disk current densities gradually decrease (**Figure 4-4b** and **4-4d**). In general, the overall half-wave potential is not recovered after washing, in contrast to ring current densities, which approaches the values obtained in the Tris-free electrolyte.

In both Fe-N-C and N-C materials, pyridinic nitrogen and hydrogenated nitrogen (pyrrolic and hydrogenated pyridine) are part of the 2×2e<sup>-</sup> mechanism, in which hydrogenated nitrogen reduces oxygen to H<sub>2</sub>O<sub>2</sub>, while pyridinic nitrogen reduces H<sub>2</sub>O<sub>2</sub> to water. Comparison between inhibition and recovery of ORR performance in metal-free and metal-containing electrocatalysts shows that the moieties that reduce oxygen directly to water (Fe-N<sub>x</sub>) have a higher affinity to TrisH compared to the active centers reducing oxygen to hydrogen peroxide (pyridinic and hydrogenated nitrogen). The metal-containing catalyst contains sites that have a stronger binding of TrisH as established by the drastic decrease

in the half-wave potential. TrisH also adsorbs onto both hydrogenated nitrogen and pyridinic nitrogen more strongly than  $O_2$ , inhibiting, thus, both the first and the second step of the ORR. However, upon Tris removal by washing, protonation of pyridine results in the creation of sites that reduce oxygen to hydrogen peroxide, which manifests itself as a recovery in the hydrogen peroxide yield. In metal-containing electrocatalysts,  $Fe-N_x$  moieties are the most active towards the full reduction of oxygen to water via either  $4e^-$  or  $2 \times 2e^-$  mechanism. At the same time, TrisH binds strongly and irreversibly to these sites, more strongly than  $O_2$ , and inhibits the oxygen reduction reaction. After removal of the TrisH by washing, most of the sites are protonated and contribute to the production of hydrogen peroxide.

### **Chapter Conclusion**

To summarize, **Figure 4-6** shows the possible mechanism of oxygen reduction and changes in surface chemistry that occur when inhibitor Tris is introduced into the acidic solution. In this diagram, it is shown that the  $Fe-N_x$  centers are being irreversibly blocked by TrisH resulting in slower direct  $4e^-$  oxygen reduction to water. At the same time protonation of pyridinic nitrogen results in the enhanced kinetics of the 1<sup>st</sup> step of reduction of oxygen to hydrogen peroxide.

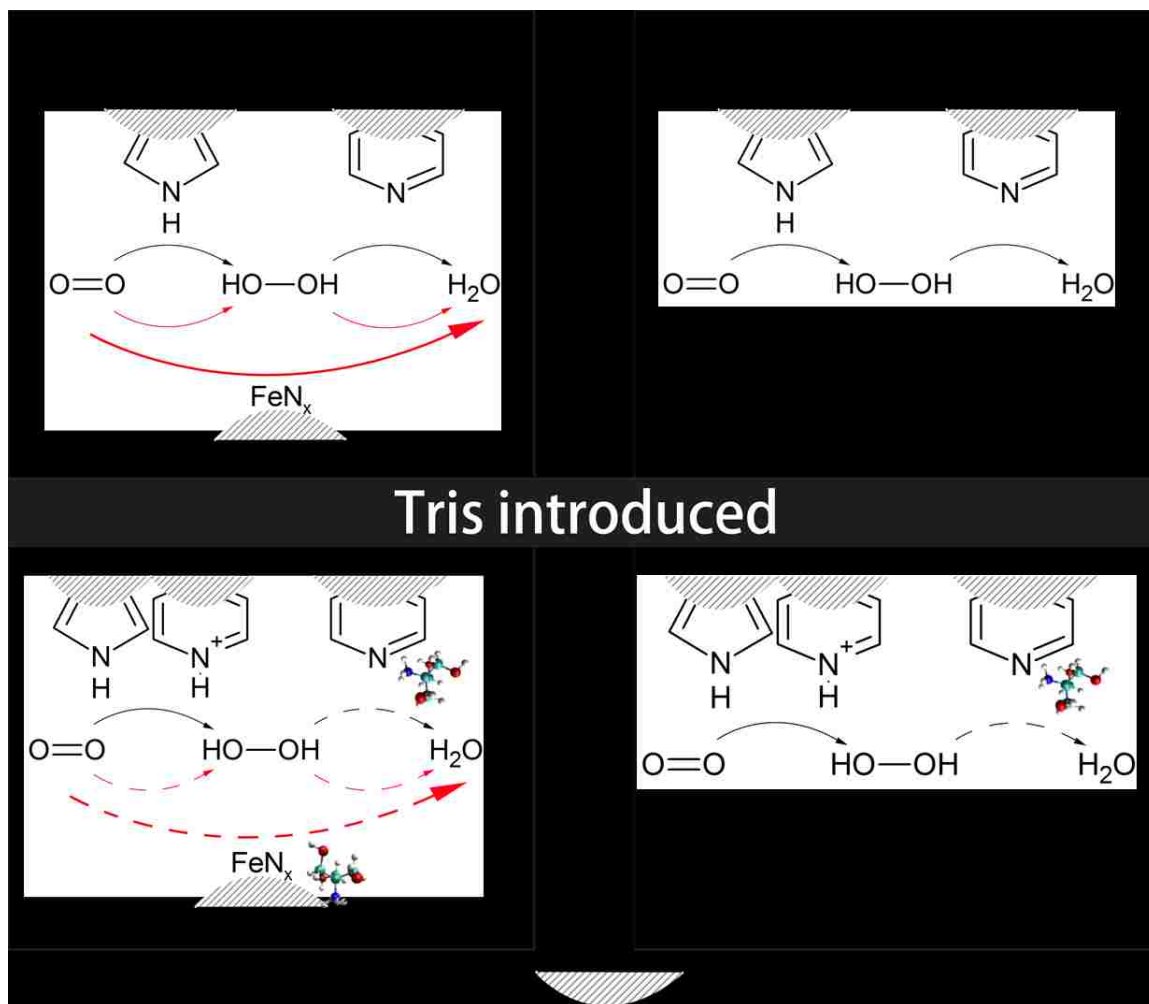


**Figure 4-6.** Schematic diagram of ORR mechanism changes. Catalytically active surface moieties are depicted schematically with no intention of implying any special positioning of distribution in the actual material. “Dashed” lines suppressed reactions subject to reversible or irreversible inhibition.

Poisoning effect of Tris(hydroxymethyl)aminomethane (Tris) on the electrocatalytic activity of M-N-C towards ORR in the acidic and alkaline environment was comprehensively studied experimentally and computationally. The experiments in acidic electrolyte also allowed to analyze the role of metal in M-N-C by studying the effect of the inhibitor on the electrochemical behavior of metal free and metal-containing electrocatalyst. The introduction of Tris into the electrolyte inhibits iron-nitrogen and nitrogen-carbon active sites. Rotating ring disk electrode experiments and density functional theory

calculations show that the Fe-N<sub>x</sub> sites could be irreversibly poisoned while N-C sites can be recovered by the removal of Tris. Density functional theory calculations also show that the protonation of pyridinic nitrogen could contribute to the recovery of the hydrogen peroxide generation in both metal-free and metal containing electrocatalysts in acidic media. As Tris is a commonly used chemical in electrochemistry research, the described phenomena reveal new avenues for mechanistic studies of PGM-free oxygen reduction catalysts.

### Extra Exploration Experiments

The catalyst loading on the working electrode may change the kinetic mechanism because of the in-plane effect, which has been observed on other kinds of Fe-N-C electrocatalysts previously<sup>53, 71</sup>. Here, extra exploration experiments were done in different loadings of FeNCB, as **Figure 4-7** shows. The LSV started using 0.2 mg cm<sup>-2</sup> loading first. After immersing in 0.1 M of Tris and following “refreshing” process, an extra 0.2 mg cm<sup>-2</sup> loading of FeNCB was deposited on the working electrode, *i.e.* in total 0.4 mg cm<sup>-2</sup>. Similar tests were also performed on 0.6 mg cm<sup>-2</sup> loading.

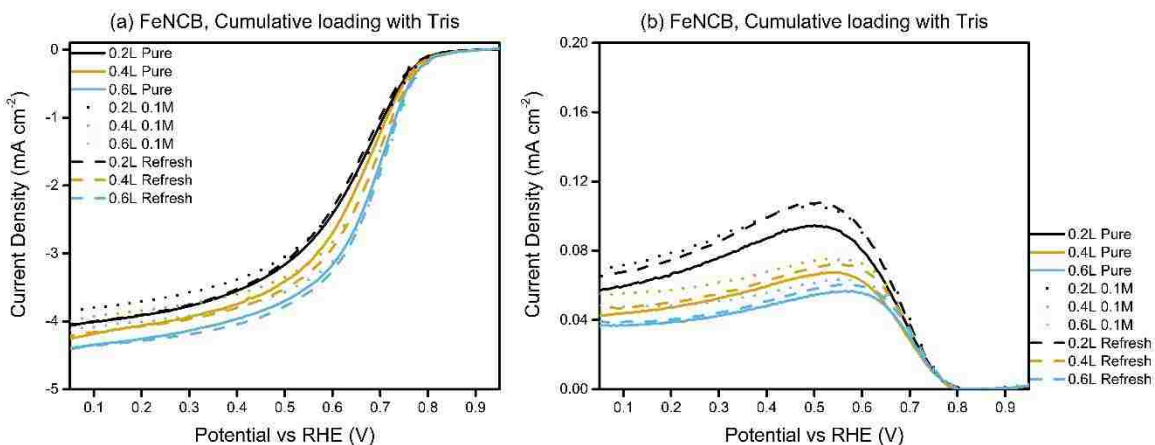


**Figure 4-7.** LSV of cumulative loadings in Tris (a) disk and (b) ring. Black, orange and blue lines show 0.2, 0.4 and 0.6 mg cm<sup>-2</sup> of FeNCB respectively. Each new loading was deposited on the previous loading after the refresh test.



Here, the inhibition of pyridinic nitrogen is more obvious than in results obtained with higher catalyst loading (see **Figure 4-2b**) after Tris was introduced for 0.1 M concentration, as **Figure 4-7b** shows. As a comparison, the half-wave potential in **Figure 4-7a** decreased but not as obviously as the one in **Figure 4-2a**, indicating that iron active sites were not severely inhibited, probably due to the limited concentration of Tris and limited edge Fe-N<sub>x</sub> active sites that can be accessible readily. As loading of 0.2 mg cm<sup>-2</sup> loading is not high enough to cover the surface area of 0.2472 cm<sup>2</sup> thoroughly and uniformly, the heterogeneity in morphology of the catalyst layer may result in a different ratio of inhibition on iron active sites and pyridinic nitrogen active sites. In addition, it is interesting that after inhibition in 0.1 M of Tris, the refreshed catalyst with 0.2 mg cm<sup>-2</sup> loading didn't have a significantly increased peroxide current density as the one after inhibition in 0.8 M of Tris (see **Figure 4-2b**). This may be due to limited inhibition of Tris. When the loading increases, it can be found that half-wave potentials and diffusion current densities increase while maximums of ring current densities decrease, which are consistent with previous reports<sup>53, 71</sup>, as more in-plane active sites take effect. Moreover, the E<sub>1/2</sub> of 0.6 mg cm<sup>-2</sup> loading didn't change in 0.1 M of Tris or after refreshing.

To exclude the interference of the cumulative deposition on the previous inhibited catalyst layer, LSV comparison between one-time deposited 0.2 mg cm<sup>-2</sup> and 0.6 mg cm<sup>-2</sup> loadings was performed, as **Figure 4-8** shows. This time, for 0.2 mg cm<sup>-2</sup> loading, the half-wave potential decreased obviously after inhibition and didn't recover after refreshing, while ring current density didn't recover or increase after refreshing, implying that Tris inhibited iron active sites rather than pyridinic nitrogen active sites. However, in 0.6 mg cm<sup>-2</sup> case, the half-wave potential didn't change in 0.1 M of Tris but decreased after refreshing (see

**Figure 4-8b**). Since Tris can reversibly inhibit nitrogen active sites but permanently inhibit iron active sites as described in Chapter 4 Conclusion, it seems that Tris molecular leaves nitrogen to inhibit in-plane iron. To check this hypothesis, more experiments in higher concentration of Tris between different loadings are needed.

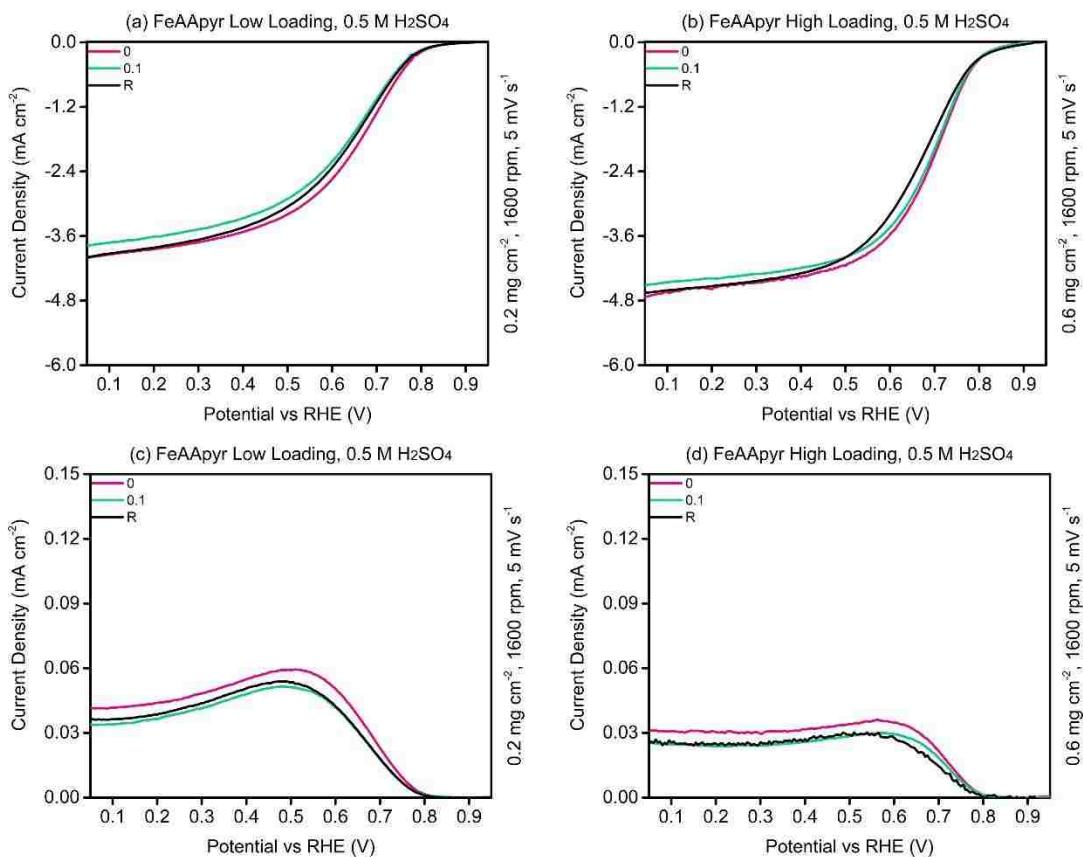


**Figure 4-8.** RRDE data for 0.1 M of Tris inhibition in different loadings (a)(b) are disk current densities of FeAApyr in 0.2 mg cm<sup>-2</sup> loading and 0.6 mg cm<sup>-2</sup> loading respectively. (c)(d) are their corresponding ring current densities.

All previous inhibition experiments were performed when Tris was introduced in solution. To check the inhibition ability of Tris powder, extra experiments were done by mixing Tris powder with the catalyst, as **Figure 4-9** shows. Here four inks were used to make the catalyst layer for LSV tests: FeAApyr + Nafion, FeAApyr + Nafion + Tris, pure FeAApyr and FeAApyr + Tris. The amount of Tris used is equimolar with FeAApyr.

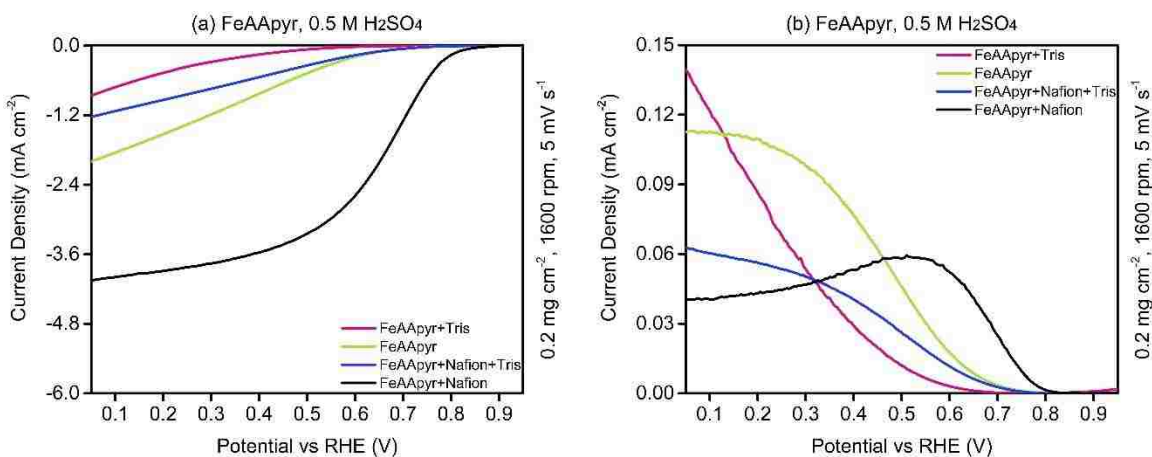


**Figure 4-9.** LSV data of different FeAApyr inks (a) disk and (b) ring. The conventional ink contains Nafion, as black line shows. This premixed here is equimolar with FeAApyr

It can be found that premixed Tris severely inhibits the performance of FeAApyr. Tris not only inhibits nitrogen and iron active sites but also prohibits efficient electric connection between the catalyst, Nafion and working electrode. Even pure FeAApyr without Nafion could beat the performance of FeAApyr + Nafion + Tris. Since previous report indicates that Nafion also has stronger binding energy<sup>69</sup> (-3.3 eV, see **Table 5-1**) with iron active sites than Tris (-1.96 eV) and oxygen (-1.43 eV), in addition to limit weight ratio (15%) of Nafion to the catalyst, it is reasonable that Fe-N-C catalyst is more resistant to Tris inhibition in solution (see **Figure 4-2a** and **4-8a**) and even sometimes  $E_{1/2}$  didn't change (see **Figure 4-7a**). As a comparison, the adsorption energy of Nafion on pyridinic nitrogen (-0.9 eV) is much smaller than the one of Tris (-3.65 eV), leading to more obvious change on ring current densities.

## Chapter 5

### **Inhibition of Active Sites with Nitrogen-Free Chemical**

The contents in this chapter have been published as “Mechanism of Oxygen Reduction Reaction on Transition Metal-Nitrogen-Carbon Catalysts: Establishing the Role of Nitrogen-containing Active Sites” in ACS Applied Energy Materials<sup>99</sup>. Co-authors are Ivana Matanovic (DFT), Elizabeth Weiler (Synthesis), Plamen Atanassov and Kateryna Artyushkova (XPS).

#### **Introduction – Selective Inhibition of Active Sites**

In addition to challenge in finding probes that are selective, it is also desirable for them to be spectroscopically distinguishable from the spectral signature of the catalyst itself. Majority of complexing agents that can be used as probes are nitrogen-based. One of the types of complexing agents free of nitrogen is a bisphosphonate chelating agent 1-hydroxyethane 1,1-diphosphonic acid (HEDP). By using this kind of phosphor-based molecular probe, it is possible to utilize XPS to tell how numerous nitrogen active sites change in the introduction of inhibitors.

Based on DFT calculations published previously, multiple types of nitrogen existing in the M-N-C materials show strong binding of reactants, intermediates, ionomers and other adsorbates that can be used as molecular probes and inhibitors<sup>65, 69, 82</sup>. For example, sulfonate group of ionomers shows strong binding with Fe-N<sub>x</sub> and weaker but still very significant binding to both graphitic and hydrogenated nitrogen active sites<sup>69</sup>. On the other hand, oxygen has the strongest binding to Fe-N<sub>x</sub> centers and weaker binding to other types of nitrogen<sup>65</sup>. Recently, we have introduced an inhibitor based on tris(hydroxyl-methyl)-

aminomethane (Tris) that shows strongest binding to pyridinic and slightly weaker binding to Fe-N<sub>x</sub> centers.

The multiple nitrogen sites existing in the MNC catalysts discussed in detail in multiple previous reports are summarized in **Figure 5-1**. First, multiple types of nitrogen coordinated with iron in either in-plane mesomeric Fe-N<sub>4</sub> (**1**) or edge disordered Fe-N<sub>x</sub> (x<4) configuration are present. Edge sites include pyridinic N (**4**), hydrogenated N (**3**) and quaternary N (**2**). Hydrogenated N includes both pyrrolic and hydrogenated pyridine. Pyridine can also be present in protonated form with a positive charge. In-plane graphitic N can be present as an in-plane defect (**5**) with or without proton depending on the local pH environment<sup>97</sup>.

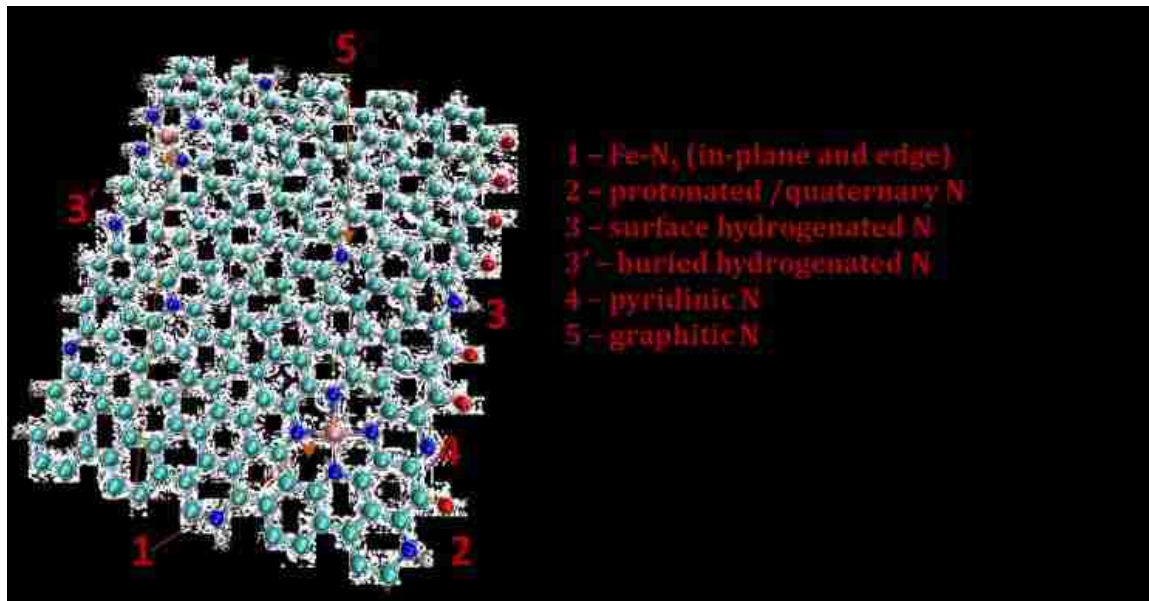


**Figure 5-1.** The types of chemical moieties present in the MNC catalyst

### **DFT Calculation on Adsorption Energy of HEDP**

**Table 5-1** compares the adsorption energies of oxygen, sulfonate fragment of Nafion, TrisH (protonated Tris) inhibitor reported recently, and HEDP on different types of

nitrogen and Fe-N<sub>x</sub> moieties shown in **Figure 5-2** as computed by DFT. **Figure 5-3** shows structures with HEDP fragment (in the mono-deprotonated form as its pK<sub>a1</sub> is 1.35) adsorbed. The results reported corresponds to the orientation and configuration with the largest adsorption energy. HEDP has strong adsorption energies to most of the nitrogen types with the highest affinity to Fe-N<sub>x</sub> sites. Moreover, the adsorption energy of HEDP onto quaternary nitrogen which encompasses any types of nitrogen that are protonated<sup>100</sup> (edge quaternary nitrogen, in-plane protonated graphitic nitrogen, and protonated pyridinic nitrogen) has the largest value of -3.79 eV (not listed in **Table 5-1**).

Site	O <sub>2</sub>	SO <sub>3</sub>	TrisH	HEDP
Fe-N <sub>x</sub>	-1.01 <sup>92</sup> to -1.43 <sup>65</sup>	-3.3 <sup>69</sup>	-1.96 (x=4) <sup>82</sup>	-2.18
Graphitic-N	-0.13 <sup>92</sup> to -0.41 <sup>65</sup>	-1.9 <sup>69</sup>	-1.07 <sup>82</sup>	-1.49
Pyridinic-N	-0.08 <sup>92</sup> to -0.28 <sup>65</sup>	-0.9 <sup>69</sup>	-3.65 <sup>82</sup>	-0.88
Hydrogenated pyridinic-N / Pyrrolic-N	-0.21 <sup>92</sup> to -0.25 <sup>65</sup>	-2.25 <sup>69</sup>	-0.53 <sup>82</sup>	-1.53

**Table 5-1.** Adsorption energy of HEDP on assorted actives sites  
All values are in the unit of eV, with a comparison of other chemicals. HEDP is in the first acid dissociated form.

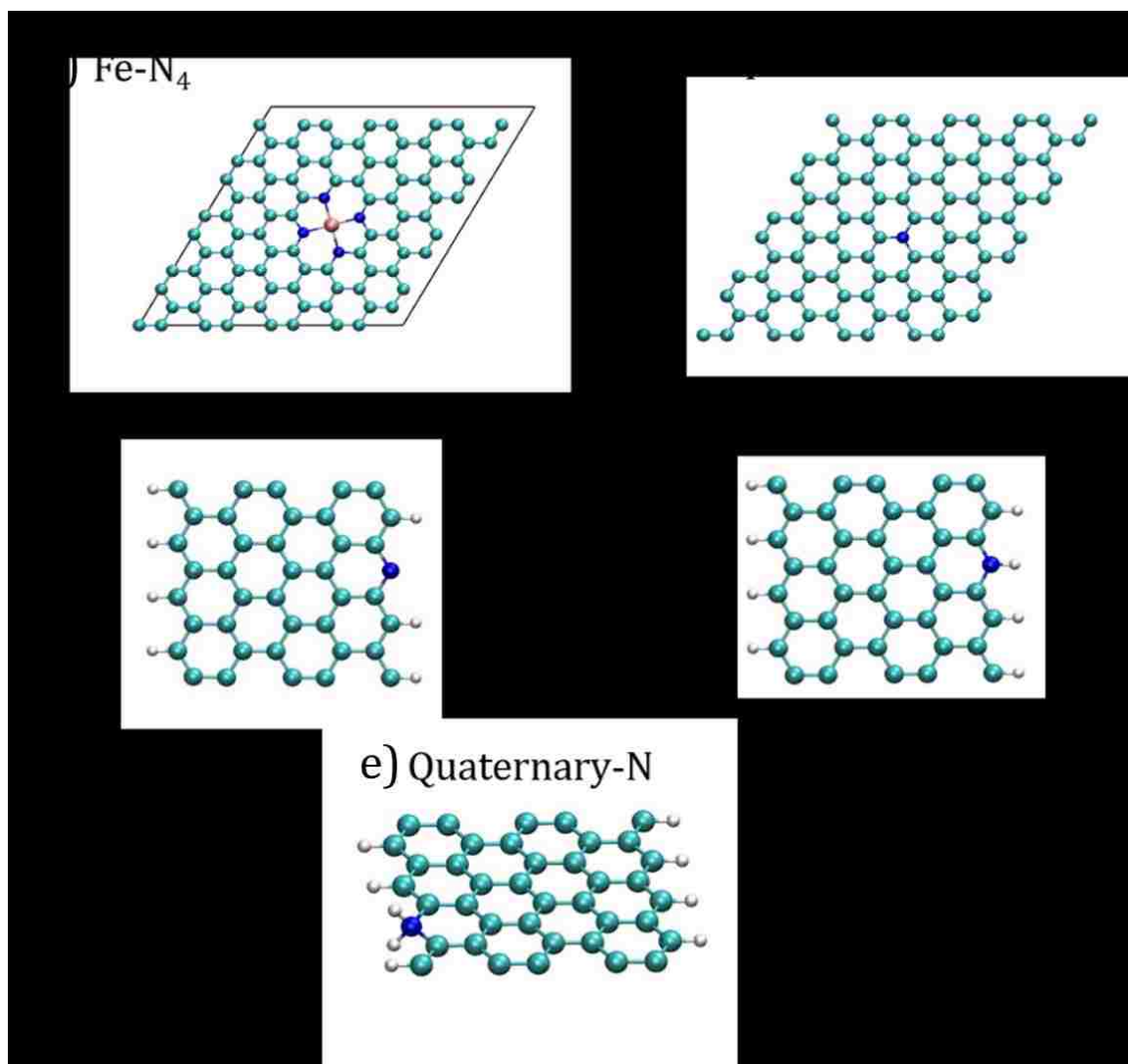


**Figure 5-2.** DFT optimized geometries of assorted active sites  
 (a) Fe-N<sub>4</sub>, (b) graphitic-N, (c) pyridinic-N, (d) hydrogenated pyridinic-N and (e) quaternary-N. Atoms belonging to a unit cell are shown. Blue – N, white – H, cyan – C, pink – Fe.

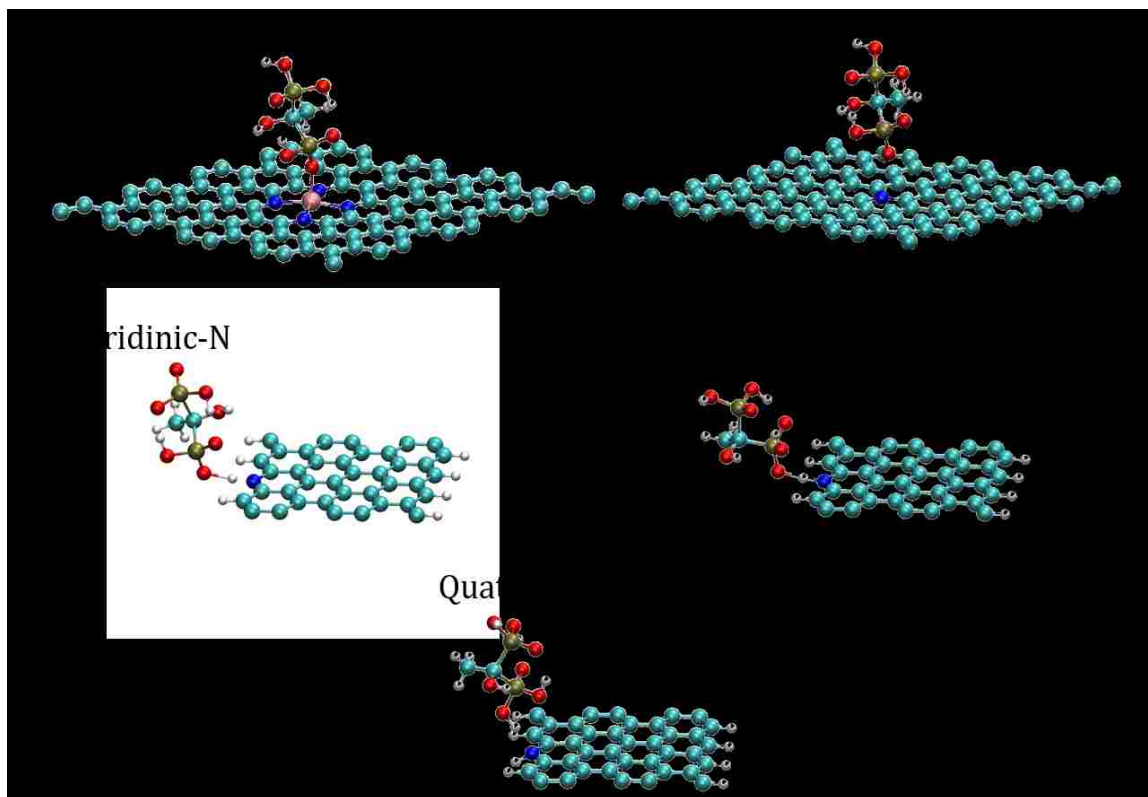


**Figure 5-3.** DFT geometries of HEDP on assorted active sites (a) Fe-N<sub>x</sub>, (b) graphitic N, (c) pyridinic-N, (d) hydrogenated pyridinic-N and (e) quaternary-N. Atoms belonging to a unit cell are shown. Blue – N, white – H, red – O, tan – P, cyan – C, pink – Fe.

### XPS of HEDP Inhibition

To confirm the binding of HEDP to the surface of the catalyst, spectroscopic analysis of changes in the surface chemistry of catalyst upon exposure and after washing of HEDP was performed by high-resolution XPS. The surface chemistry of pure catalyst and the catalyst after its exposure to HEDP at two different sampling depths was studied by both a fixed source lab-based and variable energy synchrotron-based instrument. In the lab-based instrument N 1s photoelectron has a kinetic energy of 1000 eV and it originates from approximately 20 nm of the surface, while in a synchrotron-based instrument N 1s photoelectron has a kinetic energy of only 150 eV originating from the surface depth of 2.5 nm. The power of energy-variable XPS using synchrotron sources at different source



energies was demonstrated previously for another sample from the same family of materials<sup>65</sup>. After washing HEDP from the surface of the catalyst, 0.5 at% of P is detected confirming its irreversible binding to the surface. Due to surface sensitivity of XPS, mostly unbound HEDP is detected for the unwashed sample with P 2p having a single peak due to free phosphonates at 133.5 eV. After washing away HEDP, there is a shift in the position of P 2p peak to 132.7 eV due to complexed phosphonate (**Figure 5-4**) confirming the chemical interaction between the HEDP and functional groups of the catalyst. A small amount of unbound phosphonate is still observed at the surface. **Figure 5-5** shows high-resolution N 1s spectra from both sampling depths for pure catalyst and catalyst with bound HEDP, while **Table 5-2** shows the relative surface chemical composition of nitrogen. There is a smaller amount of N detected at the surface (2.7 at % at 2 nm vs. 3.7 at % at 20 nm) which may be due to the actual smaller concentration of nitrogen present or due to a larger amount of oxygen in surface oxide groups at the surface. The relative distribution of nitrogen provides reliable and relevant information on differences in chemical composition at different sampling depths.

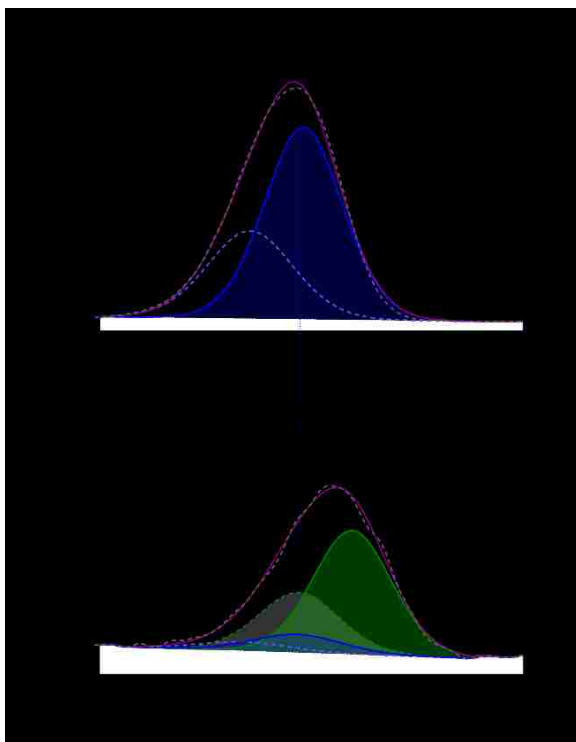


**Figure 5-4.** High resolution P 2p spectra for FeNCB sample  
Upper: dipped in HEDP, and Lower: dipped and washed.

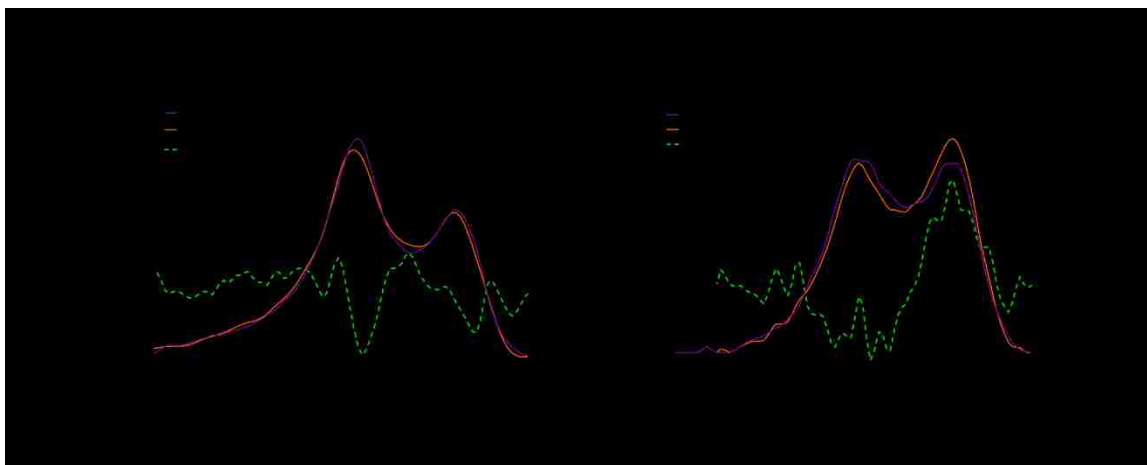


**Figure 5-5.** High-resolution N 1s spectra in UHV  
Purple lines for the fresh catalyst, red lines for catalyst after exposure and washing away HEDP, green lines for difference spectra of (a) 1000 eV N 1s photoelectron and (b) 150 eV N 1s electron. Fitted spectra are shown in **Figure 5-6**, while quantitative information extracted from the spectra is included in **Table 5-2**.

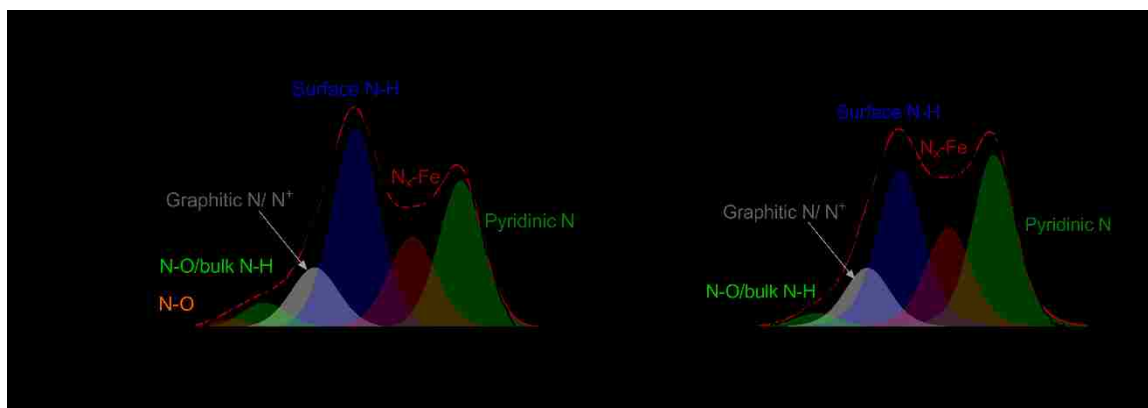


**Figure 5-6.** High resolution N 1s spectra in UHV with deconvolution

a) obtained at fixed energy lab based and b) synchrotron source spectrometers. Black – non-smoothed experimental line, red – synthetic envelope obtained from the individual peaks.

<b>Kinetic energy, Sampling depth</b>	<b>398.4</b>	<b>399.5</b>	<b>400.8</b>	<b>401.8</b>	<b>402.9</b>
<b><u>150 eV</u> <u>2.6 nm</u></b>	N <sub>pyr</sub> (4)	N <sub>x</sub> -Fe (1)	N-H (3)	N <sup>+</sup> /N <sub>gr</sub> (2,5)	NO/ Bulk N-H (3')
Catalyst	32.6	20.3	32.5	12.0	2.7
Catalyst +HEDP washed	36.2	20.5	30.7	9.6	3.1
<i>Difference</i>	3.6	0.2	-1.8	-2.4	0.4
	<b>398.4</b>	<b>399.5</b>	<b>400.8</b>	<b>401.8</b>	<b>402.9</b>
<b><u>1000 eV</u> <u>20 nm</u></b>	N <sub>pyr</sub> (4)	N <sub>x</sub> -Fe (1)	N-H (3)	N <sup>+</sup> /N <sub>gr</sub> (2,5)	NO/ Bulk N-H (3')
Catalyst	25.1	15.5	32.8	14.6	12.0
Catalyst +HEDP washed	25.8	14.8	31.3	13.7	14.4
<i>Difference</i>	0.7	-0.7	-1.6	-0.8	1.2

**Table 5-2.** Relative speciation of nitrogen species

For pure catalyst and catalyst after exposure to HEDP and their difference for two experimental conditions, at synchrotron and at the lab-based spectrometer obtained by fitting the spectra as shown in **Figure 5-6**

Very different distribution of nitrogen species at different sampling depths is evident in the catalyst. At shallower sampling depth, a higher concentration of edge pyridinic nitrogen sites is detected. The peak at 399.5 eV has a contribution from different types of iron coordinated to nitrogen, including mesomeric Fe-N<sub>4</sub> in-plane moieties and disordered edge sites such as Fe-N, Fe-N<sub>2</sub>, and Fe-N<sub>3</sub><sup>101</sup>. In-plane Fe-N<sub>4</sub> moieties will be mainly located within the plane of the graphene layer, while those with smaller than 4 nitrogen coordination will be located at the edge of exposed graphene plane<sup>102</sup>. A larger concentration of N<sub>x</sub>-Fe closer to the surface may point to the fact that the sites contributing to peak at 399.5 eV are not only mesomeric symmetrical in-plane Fe-N<sub>4</sub> centers, but also disordered edge Fe-N<sub>x</sub> sites with less than four nitrogens coordinated with iron that would be predominantly present at the edges at the surface<sup>101</sup>. At deeper sampling depth, there is also the more significant contribution of the peak at a binding energy of 403 eV. The N 1s binding energy of hydrogenated pyridinic and pyrrolic nitrogen N-H defects in nanoribbons terminated with hydrogen (C-H) is around 403 eV, while N-H edge defects located closer to the surface/air interface terminated with oxygenated carbon contribute to lower binding energy of 400.8 eV<sup>100, 103</sup>. The difference in relative abundance of the high binding energy peak at 403 eV for two different depths confirms that hydrogenated nitrogen atoms located at deeper depths are surrounded by a mixture of graphitic and amorphous aliphatic carbons contributing to the energy of 403 eV. **Figure 5-5** shows the structure of nitrogen moieties as discussed.

The changes in nitrogen chemistry when the catalyst is exposed to HEDP is captured by the difference spectra between the fresh catalyst and after exposure to the adsorbate (**Figure 5-5**). The difference in spectra within deeper layers is less intense due to a smaller

fraction of the signal coming from the adsorbed HEDP to the total 20 nm sampling depth. There is a decrease in the relative amount of edge hydrogenated nitrogen and protonated nitrogen, particularly closer to the surface. Deprotonated HEDP has a very high adsorption energy to these sites, and during the DFT optimization, it is observed that H is transferred from quaternary-N to HEDP. After washing the catalyst+HEDP with deionized water, HEDP should be removed, and protonated pyridinic nitrogen should be converted to pyridinic-N. This prediction is confirmed by an increase in the relative amount of unprotonated pyridines (peak at 398.4 eV) after washing away the HEDP as shown in **Table 5-2**. No significant difference in the region of the peak due to Fe-N<sub>x</sub> (399.5 eV) is observed. The smaller decrease in the amount of protonated nitrogen in the deeper probed layers (peak at 401.8 eV) may indicate that these nitrogen atoms are not in-plane protonated graphitic N but edge surface defects such as quaternary and protonated pyridines. From the spectroscopic analysis of catalyst with and without adsorbed HEDP, it can be concluded that the major sites blocked by HEDP are hydrogenated and protonated nitrogen atoms.

### **Results of Electrochemistry Tests**

To probe the effect of the inhibitor onto the oxygen reduction reaction, linear sweep voltammetry (LSV) in 0.5 M sulfuric acid was performed using a rotating ring disk electrode (RRDE) (**Figure 5-7**). Half-wave potentials of pure catalyst, the catalyst in the presence of 0.3 M HEDP and catalyst after washing HEDP with deionized water for 15 minutes are almost the same, being 0.72V. **Figure 5-8** shows that this behavior is true even for higher concentrations of HEDP up to 1.0 M. There is a drop of disk current density in diffusion region at 0.2 V from 4.15 mA cm<sup>-2</sup> in the pure catalyst to 3.41 mA cm<sup>-2</sup> in the presence of 0.3 M HEDP, which is completely recovered after washing inhibitor away.

According to the previous study, at the concentrations of inhibitor larger than 0.1M there is a decreased oxygen solubility causing a decrease in the current density in diffusion-limited regime<sup>82</sup>. **Figure 5-9** shows that the calculated number of electrons involved in the reaction does not depend on the presence of HEDP. This behavior indicates that HEDP doesn't compete with oxygen for binding to sites catalyzing full 4 electron reduction of oxygen to water.

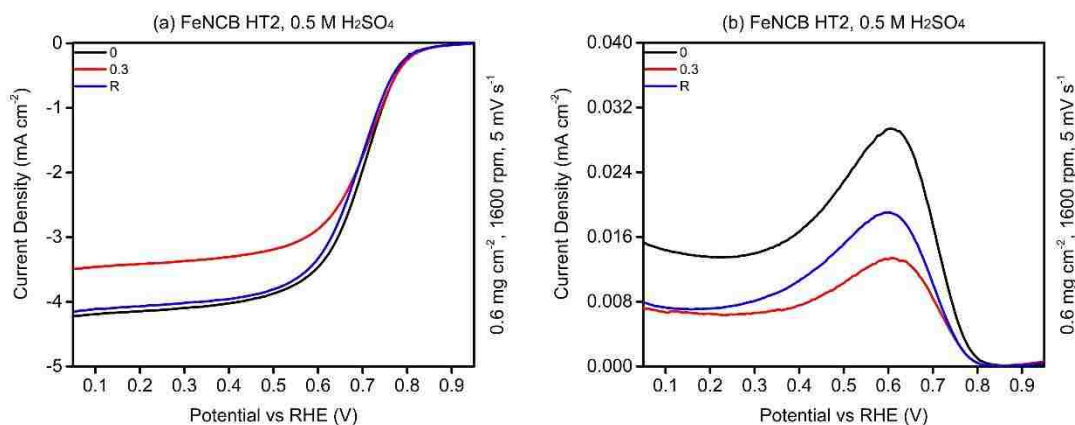


**Figure 5-7.** LSV data of catalyst tested in 0.5 M sulfuric acid (a) disk current density and (b) ring current density. Legends of 0, 0.3 and R mean pure electrolyte, 0.3 M HEDP added and refreshed electrolyte. Corresponding parameters are 0.6 mg cm<sup>-2</sup> loading of catalyst, 1600 rpm of rotation speed and 5 mV s<sup>-1</sup> of scanning rate. The metrics of performance, i.e. half-way potential, ring and disk current densities are discussed in text.

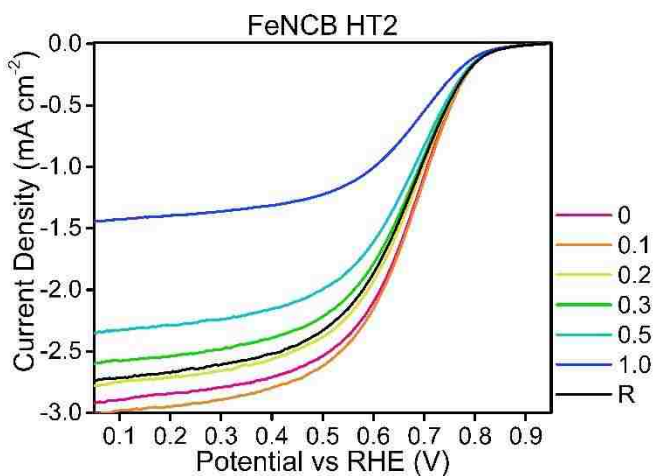


**Figure 5-8.** LSV disk polarization data of catalyst

All were tested in 0.5 M sulfuric acid with different HEDP concentrations as legend shows. R corresponds to washing away HEDP after 1.0 M experiment. Corresponding parameters are  $0.6 \text{ mg cm}^{-2}$  loading of catalyst, 1600 rpm of rotation speed and  $5 \text{ mV s}^{-1}$  of scanning rate.

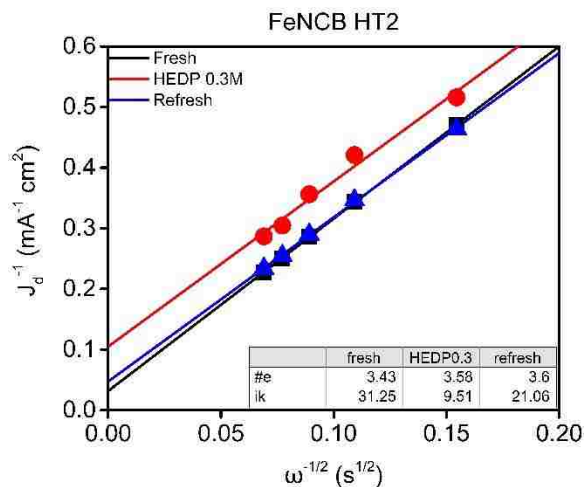


**Figure 5-9.** Koutecky-Levich plots of HEDP inhibition

For pure 0.5 M sulfuric acid (black) 0.3 M HEDP, 0.5 M sulfuric acid (red), and refreseed 0.5 M sulfuric acid (blue). #e refers to a number of the electron (derived from slope), and  $i_k$  refers to kinetic current density in the unit of  $\text{mA cm}^{-2}$  (derived from Y-intercept). Corresponding parameters are  $0.6 \text{ mg cm}^{-2}$  loading of catalyst and  $5 \text{ mV s}^{-1}$  of scanning rate. The data were collected at 400, 800, 1200, 1600 and 2000 rpm.

On the other hand, there is a significant effect of HEDP onto the ring current density, which decreases from  $0.029 \text{ mA cm}^{-2}$  for a pure catalyst to  $0.013 \text{ mA cm}^{-2}$  for a catalyst with HEDP added (values at 0.6 V). This can be mainly attributed to the inhibition of sites that mainly contribute to partial  $2\text{-e}^-$  reduction of oxygen into hydrogen peroxide. Based on DFT data and spectroscopic data discussed above, these sites are surface hydrogenated nitrogen and protonated nitrogen. After washing HEDP away, there is a partial recovery of ring current density to  $0.019 \text{ mA cm}^{-2}$ , indicating that HEDP binding to hydrogenated and protonated nitrogen sites is not completely reversible. Based on a combination of spectroscopic analysis and RRDE studies, we can conclude that there is selective inhibition of nitrogen active sites responsible for the partial reduction of oxygen to hydrogen peroxide. Similar values of the slope of Tafel plots calculated for three tests in **Figure 5-7** (98.16,

94.83 and 99.89 mV dec<sup>-1</sup> for the pure electrolyte, 0.3 M HEDP and refreshed electrolyte, respectively) confirm that HEDP does not affect iron-nitrogen active sites responsible for the full reduction of oxygen to water.

### **Near Ambient-Pressure XPS of HEDP Inhibition**

To directly demonstrate how oxygen adsorption is affected by the presence of HEDP, near ambient pressure XPS (NAPXPS) was performed for in-situ spectroscopic characterization. **Figure 5-10** shows high-resolution O 1s spectra acquired in the gaseous atmosphere for both samples showing that in addition to gaseous water and oxygen phase there is the presence of bound hydroxyls and oxygen at the surface. **Figure 5-11** shows high-resolution N 1s spectra for the pure catalyst and catalyst with adsorbed HEDP at UHV conditions and after exposure to the O<sub>2</sub>/H<sub>2</sub>O atmosphere. The difference spectra are plotted as well. The negative values in the difference spectra represent a decrease in the intensity of peaks due to species which bind oxygen and hydroxyls to it. **Table 5-3** shows changes in the chemical concentration of different nitrogen species upon exposure to humidified oxygen gas. In the case of a pure catalyst, there is a decrease in the relative amounts of peaks due to N<sub>x</sub>-Fe and N<sup>+</sup>/N<sub>gr</sub> moieties seen in both **Table 5-3** and highlighted negative peaks in difference spectra. These observations are consistent with a previously published report showing the duality of sites for oxygen binding in MNC catalysts dependent on the strength of oxygen binding to different nitrogen species<sup>36</sup>. The oxygen binding to the catalyst with adsorbed HEDP results in very different behavior. The large difference in lower binding energy of N 1s spectrum around 399 eV is observed in the negative part of the difference spectra highlighted in green in **Figure 5-11b** indicating binding of oxygen to N<sub>x</sub>-Fe sites and pyridinic nitrogen. Binding of oxygen and water to N<sub>x</sub>-Fe sites causes the shift of the peak



at 399.5 eV to higher binding energy causing an increase in the relative abundance of the peak at 400.8 eV. Binding of water to pyridinic nitrogen causes its protonation contributing to an increase in the peak 401.8 eV. No binding to protonated and graphitic nitrogen is detected at higher binding energy as these sites are blocked by adsorbed HEDP.

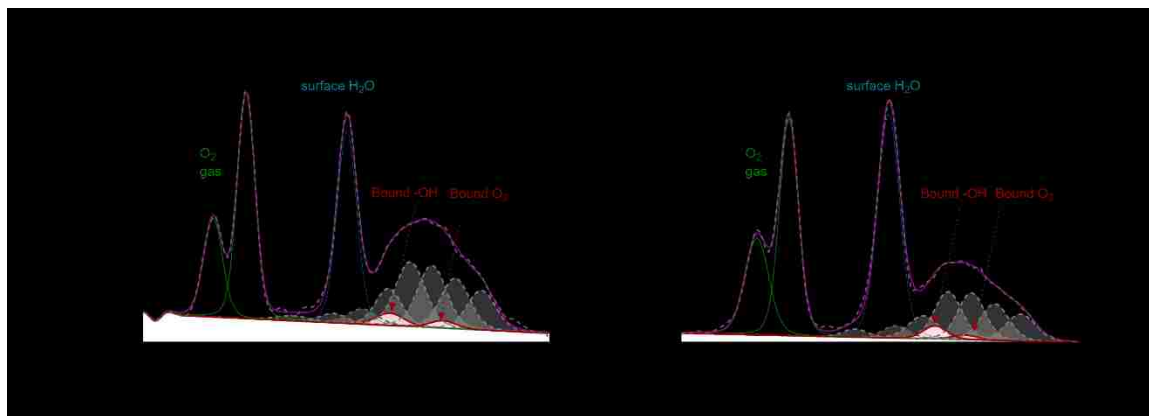


**Figure 5-10.** High resolution O 1s spectra

For FeNCB and FeNCB-HEDP samples acquired at 200 mTorr of oxygen and water. The dashed lines correspond to the O 1s components that are present on the surface of the in UHV. These peaks were fixed in position, width and relative areas and used to fit the O 1s spectra in the gaseous atmosphere<sup>104</sup>.

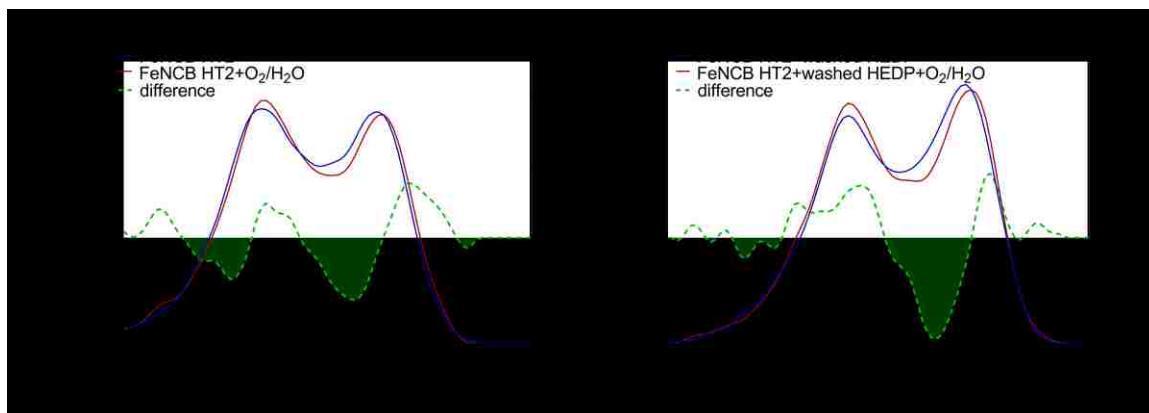


**Figure 5-11.** High-resolution N 1s spectra and difference spectra

For the fresh catalyst (a) and catalyst after exposure and washing away HEDP overlaid (b) in UHV and in 200 mTorr of oxygen and water (1:1 volume ratio). Quantitative information extracted from the spectra is included in **Table 5-3**.

	398.4	399.5	400.8	401.8	402.9
<b>FeNCB</b>	N <sub>pyr</sub> (4)	N <sub>x</sub> -Fe (1)	N-H (3)	N <sup>+</sup> /N <sub>gr</sub> (2,5)	NO/ Bulk N-H (3')

Catalyst UHV	32.6	20.3	32.5	12.0	2.7
Catalyst +gas	32.8	18.4	33.6	10.9	4.3
<i>Difference</i>	<i>0.2</i>	<i>-1.8</i>	<i>1.1</i>	<i>-1.1</i>	<i>1.6</i>
	<b>398.4</b>	<b>399.5</b>	<b>400.8</b>	<b>401.8</b>	<b>402.9</b>
<b>FeNCB + washed HEDP</b>	N <sub>pyr</sub> (4)	N <sub>x</sub> -Fe (1)	N-H (3)	N <sup>+</sup> /N <sub>gr</sub> (2,5)	NO/ Bulk N-H (3')
Catalyst + washed HEDP UHV	36.2	20.5	30.7	9.6	3.1
Catalyst + washed HEDP +gas	34.2	19.1	33.5	10.9	2.4
<i>Difference</i>	<i>-2.0</i>	<i>-1.4</i>	<i>2.8</i>	<i>1.3</i>	<i>-0.7</i>

**Table 5-3.** Relative speciation of nitrogen species in NAPXPS

For pure catalyst and catalyst after exposure to HEDP in UHV and a gaseous environment. The difference between them for two experimental conditions is shown. The numbers in the first low of **Table 5-3** in the unit of eV. The numbers in brackets point to **Figure 5-1**.

## Chapter Conclusion

The results of the in-situ spectroscopy and electrochemical testing clearly identify the chemical structures that are responsible for two parallel mechanisms of ORR, via direct 4 electron reduction of oxygen to water, which occurs on iron coordinated to nitrogen Fe-N<sub>x</sub> sites, and via dual site 2×2 electron mechanism, where protonated and hydrogenated nitrogen catalyze the reduction of oxygen to hydrogen peroxide<sup>28</sup>. From previous studies, we have observed that pyridinic nitrogen is catalyzing the second step of reaction of H<sub>2</sub>O<sub>2</sub> reduction to H<sub>2</sub>O<sup>36</sup>. The role of different defects in the ORR mechanism on MNC catalysts are illustrated in **Figure 5-12**.

In conclusion, the HEDP is a unique inhibitor that has strong and partially irreversible adsorption to protonated and hydrogenated nitrogen, which increases the selectivity of the

catalyst towards the 4-electron reduction of oxygen to water. HEDP has, therefore, a potential application as fuel cell cathode additive to improve cathode selectivity. Importantly, the selectivity of HEDP towards binding to hydrogen peroxide producing sites should ensure that total density of sites performing full oxygen reduction to water will not be reduced.

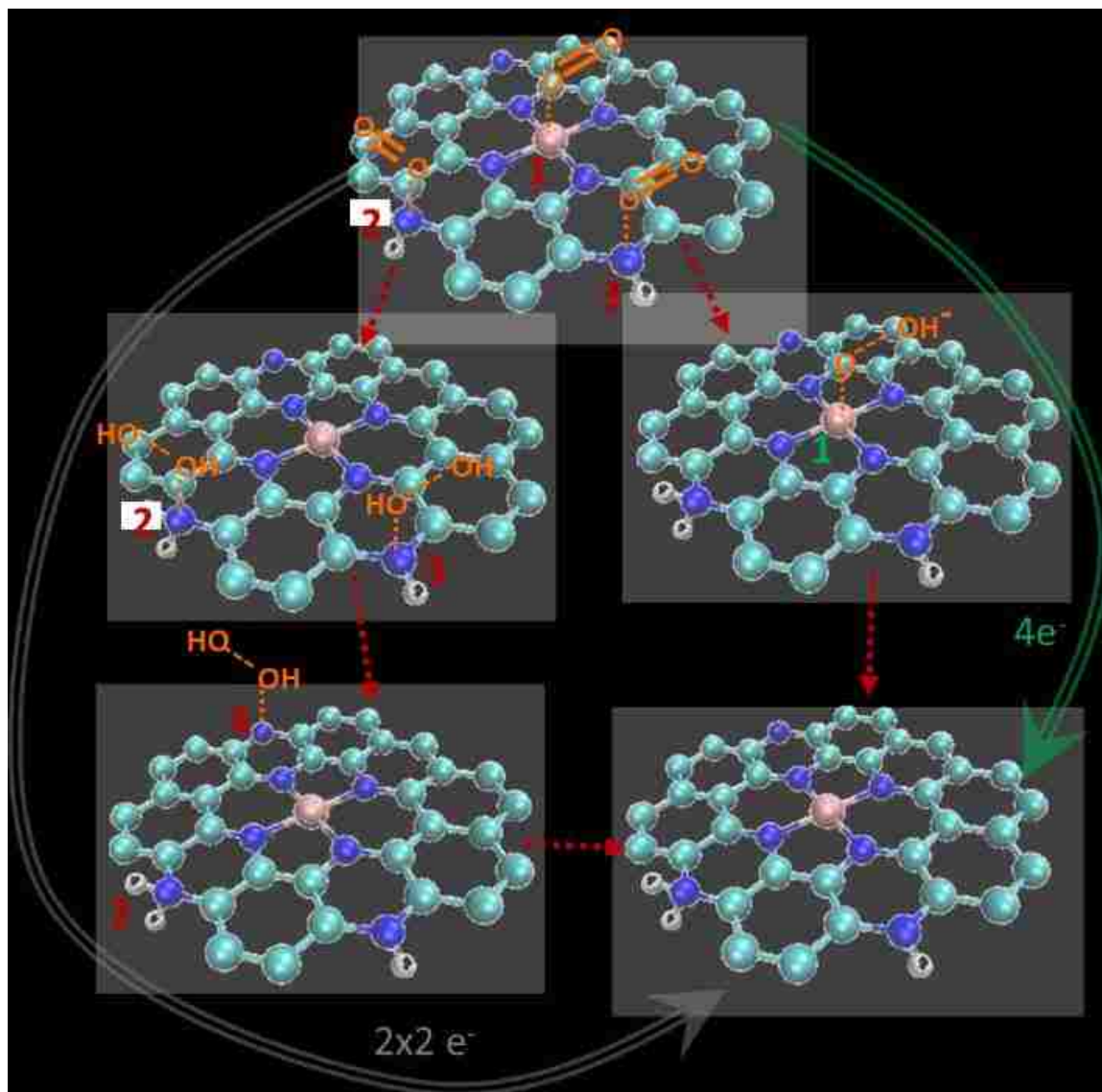


**Figure 5-12.** Two parallel pathways of the ORR mechanism  
Oxygen binds strongly to  $N_x$ -Fe (1), N-H (3) and  $N^+$  (2) sites. Direct  $4e^-$  occurs on  $N_x$ -Fe sites, while N-H and  $N^+$  catalyze  $2e^-$  reduction to  $H_2O_2$  which is further reduced on pyridinic N

## Extra Combination Experiments

As HEDP is more selective to pyrrolic nitrogen that partially reduces oxygen into peroxide while Tris is more selective to pyridinic nitrogen that can reduce peroxide into water, it will be interesting to combine these two inhibitors. Initial exploration experiments of LSV were done by first introducing HEDP, then followed by the extra introduction of Tris after refreshing the working electrode, as **Figure 5-13** shows, with 5 consecutive LSV tests. Here R1 and R2 represent the refreshed working electrode after inhibition of HEDP and Tris respectively.

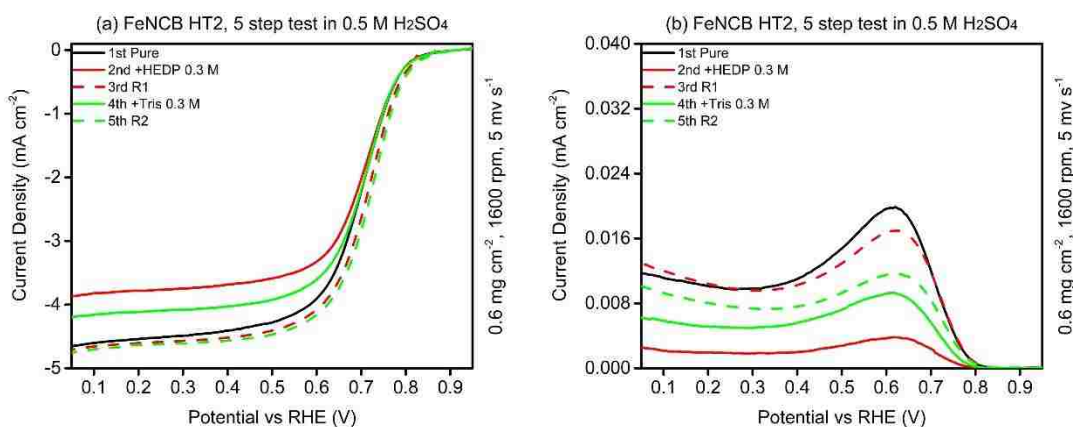


**Figure 5-13.** RRDE data of FeNCB after sequential inhibition and washing

R1 represents the first refreshed situation after washing from HEDP contained electrolyte and R2 represents the second refreshed situation after washing from Tris contained the electrolyte.

The first 3 steps have similar phenomena in both disk and ring as previous standard HEDP (see **Figure 5-7**) since partial pyrrolic / hydrogenated nitrogen active sites were inhibited by HEDP and transformed into pyridinic nitrogen. The difference on ring current density after refresh is mainly due to different catalyst layers in each test. In 4th and 5th tests of Tris inhibition, it can be found that  $E_{1/2}$  has negligible change but ring current density decreased even after refreshing. The consistency of half-wave potential may be attributed to the protection of Fe-N<sub>x</sub> active sites by HEDP against extra adsorption of Tris. It is still

unknown why peroxide continued decreasing. One hypothesis can be made that TrisH could transfer a proton to deprotonated HEDP. If HEDP was adsorbed on iron active sites, this proton transfer supplies more proton to let Fe-N<sub>x</sub> go 4-electron pathway. If HEDP was adsorbed on pyrrolic / hydrogenated pyridinic N active sites, TrisH could not transfer more protons as protonated HEDP is saturated. Extra DFT calculation and combination electrochemistry tests are needed to check this hypothesis.

## Chapter 6

### **Rational Design of Synthesis to Get Specific Ratio of N Active Sites**

The contents in this chapter have been published as “Novel highly active and selective Fe-N-C oxygen reduction electrocatalysts derived from in-situ polymerization pyrolysis” in Nano Energy<sup>32</sup>. Co-authors are Rohan Gokhale (Synthesis & TEM), Alexey Serov, Kateryna Artyushkova (XPS) and Plamen Atanassov.

### **Introduction – Polymerization-Pyrolysis Method**

As described in previous chapters, the environment of nitrogen active sites in Fe-N-C electrocatalysts corresponds to the performance of oxygen reduction reaction. Since pyridinic nitrogen can reduce peroxide into water and hydrogenated pyridinic nitrogen goes 2-electron pathway to reduce oxygen into peroxide, one rational design to make Fe-N-C prefer 4-electron (or 2×2-electron) pathway is to get the specific ratio of pyridinic-N active sites and to limit the ratio of pyrrolic nitrogen. The extra adjustment could then be done by introducing nitrogen inhibitors such as Tris or HEDP that have been described in Chapter 4 and 5. Here a novel Polymerization-Pyrolysis Method (PPM) is introduced for attempting to get a specific ratio of pyridinic-N, assisted with Sacrificial Support Method (SSM)<sup>28, 88-89, 105-108</sup>. Two kinds of pyridine with one or two amino groups used as N-C precursors are polymerized with in-situ or ex-situ silica templates, followed by pyrolysis with iron salts, acid etching, and ammonia gas thermal treatment processes successively. The synthesized PGM-free cathode catalyst performs well in electrochemical tests in both acidic and alkaline media. It is the first time to demonstrate the utilization of polymerized pyridine with a C-N-C backbone as the N-C precursor for the synthesis of ORR catalysts.

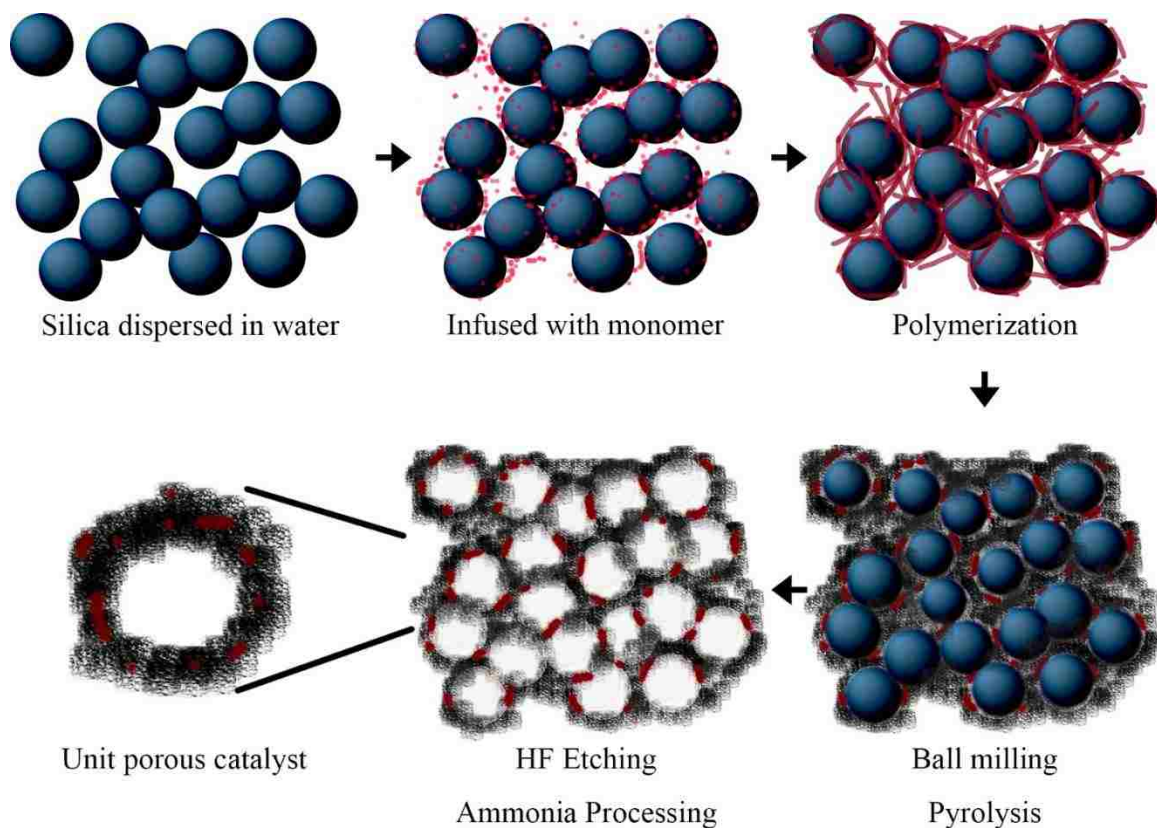


**Figure 6-1.** Schematic diagram of PPM process using in situ SSM

There are several reasons why pyridine polymers with amino groups are chosen as the nitrogen and carbon sources to prepare ORR catalysts: (i) pyridine based molecules have a nitrogen atom in the aromatic ring, which was previously observed to possess efficient catalytic performance in alkaline media after pyrolysis<sup>109</sup>; (ii) polymerization is an efficient way to reduce the distance between carbon and nitrogen atoms so that the N-C network could easily form during the pyrolysis (a similar method is to make Fe-N-C chelates as precursors<sup>110</sup>); (iii) polymers have been extensively used as precursors for some of M-N-C catalysts<sup>28</sup>; and (iv) C-N-C backbone forming polyaniline (the aromatic ring is benzene with no nitrogen atoms) have also been widely studied as precursors to synthesize highly active catalysts after pyrolysis<sup>31, 111-112</sup>. The general requirements to N-C precursors for

SSM were previously summarized by our group<sup>105</sup>. Inspired by the performance of pyrolyzed polyaniline<sup>106</sup> where monomers are combined into polymers by forming C-N-C bonds, pyridine-based precursors with amino groups attached to the aromatic cycle were used to form polymers with the oxidative function performed by persulfate salts. **Figure 6-1** shows the schematic diagram of polymerization-pyrolysis process using in situ SSM that is utilized in this chapter.

### **Synthesis of Fe-N-C via PPM**

2-Amino-6-methylpyridine and 2,6-diaminopyridine were obtained from Sigma Aldrich and used without further purification. Commercial silica powder (CAB-O-SIL LM-150 fumed silica) was used as SSM template, while ammonium persulfate was used for the polymerization process. Iron nitrate nonahydrate was used as the Fe source.

#### ***Polymerization***

The specific amount of 2-amino-6-methylpyridine (AMP) and 2,6-diaminopyridine (DAP) (precursors) were first weighed respectively, followed by placing 2-amino-6-methylpyridine in 50 °C thermostatic chamber to make it melt (melting point 40-44 °C). **IN SITU** synthesis: the equimolar amount of ammonium persulfate and 20 wt% of silica powder was mixed in water. By adding precursors into the water, the polymerization was started. For the 2-amino-6-methylpyridine polymer, the solution color started changing in 5 minutes, from initial light yellow to dark brown after three hours. For the 2,6-diaminopyridine polymer, the color instantly changed once the precursor was added to the mixture, becoming nearly black in just 1 minute. After stirring three hours, these slurries were centrifuged and washed by DI water at 3500 rpm, then dried and collected. **EX SITU**



synthesis: the equimolar amount of ammonium persulfate only was dissolved in water, followed by introducing amino pyridines. The color changing rate was slower than in situ ones, but the solution color with DAP inside still becomes nearly black in 1 to 3 minutes. After stirring three hours, the color of AMP polymerization products also became dark brown and nearly black. Silica was added post polymer formation before pyrolysis step together with iron nitrate in this process.

### ***Pyrolysis***

For **IN SITU** synthesis, a specific amount of AMP and DAP polymers were mixed with 10 wt% iron nitrate nonahydrate (calculated by the amount of precursors) by ball milling one hour at 480 rpm. For **EX SITU** synthesis, polymers were mixed with 10 wt% iron nitrate and 20 wt% silica (as a template) by ball milling using the same parameters. These mixtures were then pyrolyzed in 7 at% hydrogen (balanced by nitrogen) atmosphere at 950 °C for 60 minutes with a ramp rate of 10 °C/min. The pyrolyzed black powders were etched in HF and HNO<sub>3</sub> mixed acid (1:1 by volume), following by centrifugation, washing, and drying.

### ***Ammonia processing***

The pyrolyzed Fe-N-C catalysts were further processed in 10 at% ammonia (balanced by nitrogen) atmosphere at 950 °C for 60 minutes. After this, they were ground and collected for characterization. For IN SITU type, the final 2-amino-6-methylpyridine based catalyst was designated as 26AMP-in, while 2,6-diaminopyridine one was designated as 26DAP-in. For EX SITU type, the products were designated as 26AMP-ex and 26DAP-ex respectively.

## Properties and Discussion

### *Possible polymerization pathway*

It is hypothesized that the reaction between ammonium persulfate and 2-amino-6-methylpyridine or 2,6-diaminopyridine belong to the type of oxidative polymerization which is similar with the one where aniline is polymerized with the assistance of persulfate salt. Mechanism of polyaniline formation<sup>113</sup> implies a step where monomers could couple with each other either in ortho or para positions. For polyaniline, an ortho-type pathway leads to a linear structure while para-type results in planar construction. Each phenyl group is connected to each other by nitrogen atoms. With the interference of heterocyclic nitrogen in the aromatic ring, both ortho and para-types may lead polymerization of pyridine to a planar construction. **Figure 6-2** shows the proposed polymerization process of 2-amino-6-methylpyridine. It is probable that the methyl group in the meta position of the amino group could interfere with the reaction process due to steric hindrance. When this methyl group is substituted by an amino group, the polymerization should occur much easier since the ortho position of one amino group is also the para position of another amino group, as **Figure 6-2b** shows. This symmetry decreases the competition of ortho-type and para-type polymerization, leading to a rapid color transformation in just one minute for 2,6-diaminopyridine even without the use of silica template to promote the rate of reaction. However, lack of steric hindrance could limit the formation of pores, resulting in DAP samples with the much smaller surface area than AMP products, which is proved by the BET surface area measurement that will be discussed below.

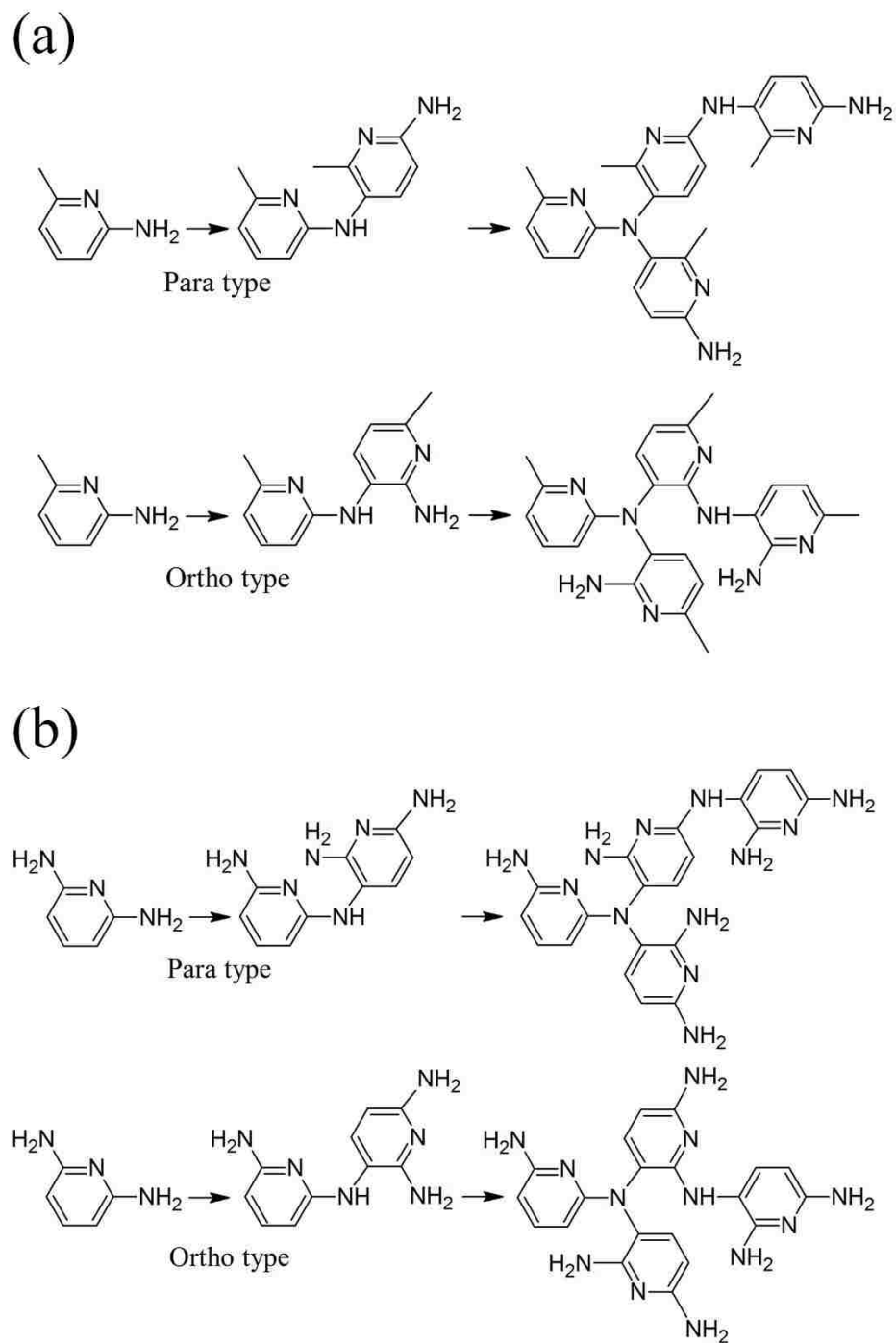


**Figure 6-2.** Polymerization diagram  
 (a) 2-amino-6-methylpyridine, and (b) 2,6-diaminopyridine

### *TGA and FTIR results*

The synthesized polymers are investigated using TGA and FTIR, as it shown in **Figure 6-3a** and **3b** respectively. TGA is used to analyze the decomposition process at high temperature whereas FTIR is mainly utilized as a structural identification tool. Both methods include spectra from in situ samples with encapsulated silica particles. From Figure 3a, long flat slopes could be observed in TGA spectra of AMP and DAP polymers tested under a nitrogen atmosphere, which is a typical pyrolysis feature of pyridine polymers<sup>114</sup>. In a low-temperature area ranging from 100 °C to 400 °C, it is found that AMP polymer decomposes earlier than DAP polymer, which could be attributed to a better-connected backbone formed by two amino groups than by one amino group. In the high-temperature region, the pyrolyzed AMP polymer stops losing weight around 600 °C while DAP polymer continues decomposition slowly until 900 °C. The final temperature 950 °C just exceeds the pyrolysis stabilization line of DAP. The reason why the final remaining weight ratio of AMP w/ silica mixture is higher than the one of DAP mixture may be attributed to the two causes. One is the presence of silica. As the yield of AMP polymer is lower, it constitutes a smaller weight portion in the mixture in contrast to the high yield DAP polymer, while the amount of silica is the same. The other cause is a stability of AMP polymer since it stops losing weight at just 600 °C. Figure 2b shows the FTIR spectra of in situ AMP and DAP polymers respectively. The strong peak around 1080 cm<sup>-1</sup> in both AMP and DAP polymers is caused by Si-O-Si stretching referring to the research of pyridylamine-modified silica<sup>115</sup>. Also, the peak at 1650 cm<sup>-1</sup> representing C=N bond exists while the signal of N-H (1° amine) stretching at 3450 cm<sup>-1</sup> is not apparent. This infrared feature reveals that amino group links pyridyl group together in both polymerizations. In

addition, according to other previous research in silicon oxide composite<sup>116</sup> and 2-aminopyridine<sup>117</sup>, other absorption peaks could be designated: 440  $\text{cm}^{-1}$  refers to  $\delta$  (bending) of Si-O-Si; 570  $\text{cm}^{-1}$  refers to the bending of pyridine ring; 780  $\text{cm}^{-1}$  refers to  $\gamma$  (out-of-plane bending) of C-H; absorption around 1410  $\text{cm}^{-1}$  in AMP refers to antisymmetric bending of C-H, and may also consist of an overlapping from the vibration of C-H around 1440  $\text{cm}^{-1}$ , which appears in DAP. Moreover, the absorptions at 2350  $\text{cm}^{-1}$  and 3200  $\text{cm}^{-1}$  could not be designated as there is strong interference from water and carbon dioxide from air<sup>118</sup>. The sharp peaks around 2350  $\text{cm}^{-1}$  are attributed to the interference of  $\text{CO}_2$ . Two flat broadenings in both AMP and DAP around 3200  $\text{cm}^{-1}$  may be either vibration of N-H ( $2^\circ$  amine) or O-H, which may come from the residue of polymerization or just from the environment.

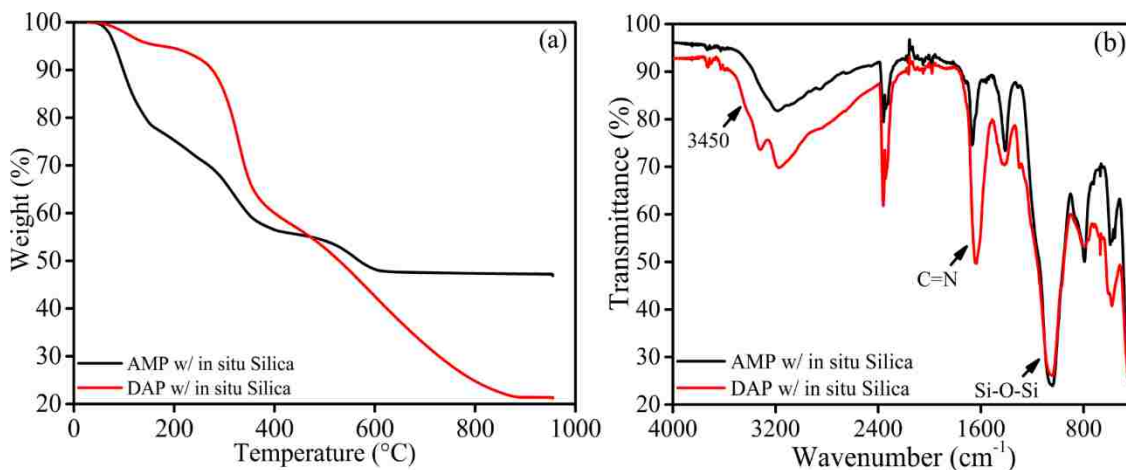


**Figure 6-3.** (a) TGA plots and (b) FTIR spectra of polymers. Both AMP and DAP polymers are tested with in-situ silica.

### ***XRD pattern and BET results***

XRD characterization was performed to determine the phases which can be formed during the synthesis. **Figure 6-4a** and **4b** show the diffractograms of 26AMP-in, 26AMP-ex and 26DAP-in, 26DAP-ex. The curves with noise show original data while the solid ones

describe fitted data which were processed by Jade 2010, with full results shown in **Table 6-1**. The strong diffraction peak at  $26^\circ$  in all spectra is found to be the (111) feature of graphite (according to JCPDS 98-001-9678), while the broadening indicates a presence of the amorphous phase. The graphite is estimated to occupy 3.8 weight% and has a 5.7 nm crystal size, calculated via the Scherrer equation. Four strong diffraction intensities at  $30^\circ$ ,  $33^\circ$ ,  $43^\circ$  and  $53^\circ$  could be found in all samples only except 26DAP-in, which could be referred to the most four apparent peaks of iron sulfide FeS (03-065-6841), whose strongest diffraction signal of FeS is at  $43^\circ$  but overlaps with graphite (100). They are estimated to be 1.2 wt%, 1.4 wt% and 1.0 wt% in 26AMP-in, 26AMP-ex and 26DAP-ex respectively. FeS is still used to fit 26DAP-in and estimated to occupy 0.5 wt%. Corresponding sizes are separately calculated to be 17.9 nm and 11.4 nm in 26AMP-in and 26AMP-ex while the sizes in both 26DAP catalysts are 15.5 nm. The existence of FeS probably comes from the reaction between iron nitrate and the residue of persulfate and sulfate after the polymerization. They may exist deep inside the carbon matrix which is difficult to be etched by nitric and hydrofluoric acid.

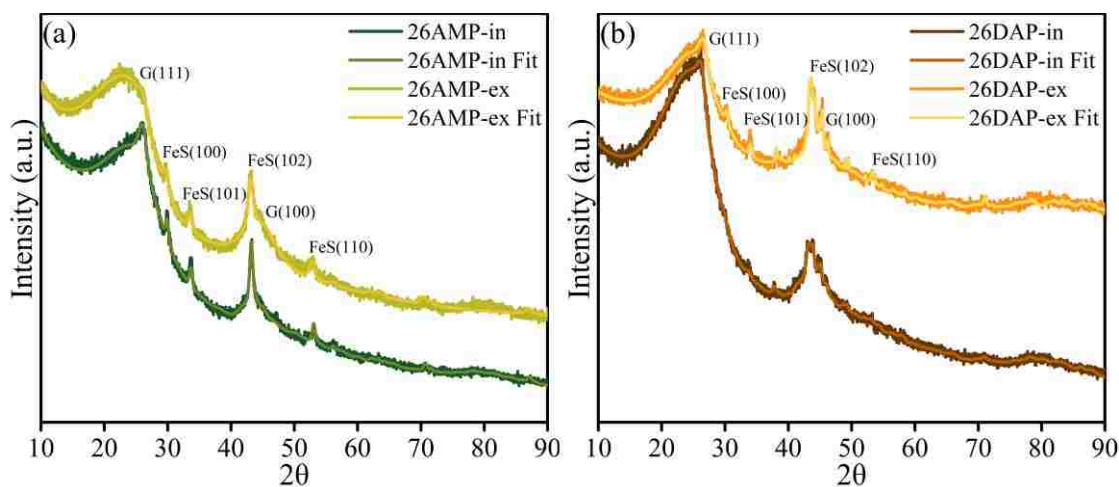


**Figure 6-4.** Raw and fitted XRD patterns  
(a) 26AMP-in, 26AMP-ex (b) 26DAP-in, 26DAP-ex.

<b>Table 6-1a</b>	Formula	PDF-#	Weight%	Size (Å)
Amorphous	N/A	N/A	89.4% (3.9)	N/A
Graphite	C	98-001-9678	5.2% (0.3)	57 (2)
Iron Sulfide	FeS	03-065-6841	1.2% (0.1)	179 (7)
Iron Nitride	Fe <sub>2</sub> N	00-050-0958	2.6% (0.2)	58 (4)
Iron Nitride	Fe <sub>8</sub> N	04-007-1780	1.6% (0.1)	58 (2)

R=2.09%, E=1.45%, R/E=1.31

N/A: Not Available

<b>Table 6-1b</b>	Formula	PDF-#	Weight%	Size (Å)
Amorphous	N/A	N/A	88.4% (4.3)	N/A
Graphite	C	98-001-9678	2.1% (0.2)	61 (4)
Iron Sulfide	FeS	03-065-6841	1.4% (0.1)	114 (4)
Iron Nitride	Fe <sub>2</sub> N	00-050-0958	4.4% (0.3)	59 (3)
Iron Nitride	Fe <sub>8</sub> N	04-007-1780	1.8% (0.1)	66 (2)
Cohenite	Fe <sub>3</sub> C	98-000-0170	1.9% (0.2)	61 (4)

R=1.5%, E=1.22%, R/E=1.22

<b>Table 6-1c</b>	Formula	PDF-#	Weight%	Size (Å)
Amorphous	N/A	N/A	93.1% (3.7)	N/A
Graphite	C	98-001-9678	2.9% (0.2)	59 (2)
Iron Sulfide	FeS	03-065-6841	0.5% (0.0)	77 (5)
Iron Nitride	Fe <sub>2</sub> N	00-050-0958	1.8% (0.1)	62 (4)
Iron Nitride	Fe <sub>8</sub> N	04-007-1780	1.1% (0.1)	57 (2)

Cohenite	Fe <sub>3</sub> C	98-000-0170	0.6% (0.0)	155 (14)
----------	-------------------	-------------	------------	----------

R=1.5%, E=1.25%, R/E=1.19

<b>Table 6-1d</b>	Formula	PDF-#	Weight%	Size (Å)
Amorphous	N/A	N/A	91.5% (2.3)	N/A
Graphite	C	98-001-9678	3.8% (0.3)	57 (2)
Iron Sulfide	FeS	03-065-6841	1.0% (0.1)	153 (9)
Siderazot	Fe <sub>3</sub> N	04-007-2250	0.7% (0.1)	58 (5)
Iron Nitride	Fe <sub>8</sub> N	04-007-1780	2.3% (0.1)	59 (1)
Cohenite	Fe <sub>3</sub> C	98-000-0170	0.8% (0.1)	554 (104)

R=1.53%, E=1.21%, R/E=1.25

<b>Table 6-1e</b>	26AMP-in	26AMP-ex	26DAP-in	26DAP-ex
C at%	99.670%	99.614%	99.863%	99.726%
Fe (Fe-S) at%	0.165%	0.193%	0.068%	0.137%
S at%	0.165%	0.193%	0.068%	0.137%

**Table 6-1.** XRD fitting datasheet of different catalysts

(a) 26AMP-in, (b) 26AMP-ex, (c) 26DAP-in, (d) 26DAP-ex, and (e) atomic percent estimation of sulfur. The figures between brackets after each value represent the deviation.

To clarify whether in situ method gives larger surface areas after etching silica, BET analysis was performed, as **Table 6-2** lists. It is found that both AMP-based in situ and ex situ samples have high surface areas, which are 867 m<sup>2</sup>/g and 639 m<sup>2</sup>/g respectively. As a comparison, 26DAP-in reaches 416 m<sup>2</sup>/g while 26DAP-ex has a surface area of 365 m<sup>2</sup>/g. These results reveal that the pyrolyzed polymer where monomer has one amino group is much more porous than that with two amino groups. In addition, the surface area difference



between AMP-based in situ and ex situ catalysts (228 m<sup>2</sup>/g) is much larger than the one between DAP based two catalysts (51 m<sup>2</sup>/g). This may be attributed to the fact that during in situ polymerization more homogeneous coverage of silica particles with the polymer is achieved. While in ex situ method ball milling mixing can be done on the level of agglomerate and aggregates in contrast to individual SiO<sub>2</sub> particles. Additionally, it is also observed that AMP monomer-based catalysts possess a higher surface area as compared to DAP based ones. This variation could be related to the initial polymer structure and the polymerization process difference that occurs in each of these monomers.

<b>Table 6-2</b>	26AMP-in	26AMP-ex	26DAP-in	26DAP-ex
BET (m <sup>2</sup> g <sup>-1</sup> )	867	639	416	365

**Table 6-2.** BET surface areas of different catalysts

### *XPS and Raman results*

XPS elemental compositions including C, O, N, Fe and S are shown in **Table 6-3**. Corresponding nitrogen and iron component XPS are shown in **Figure 6-5** and **6-6**. Compared with apparent FeS component in XRD, there are neither sulfur component detected in XPS except 0.1% in 26DAP-ex, nor iron-sulfur bonds detected in an iron component of all four catalysts. The reason is that XPS is a surface characterization technology that normally has only several nanometers in detection depth and less than 1 micrometer in diameter, while XRD is a bulk material detection technology (Rigaku SmartLab used here needs samples to be put in a square of centimeters). A simple estimation from fitting the XRD data is made to convert weight% to atomic% by regarding all components except FeS as carbon, which could be found in **Table 6-1e**. It shows that even in 26AMP-ex (it possesses the highest FeS weight% in four catalysts), there is only

0.19 atomic% of sulfur and equimolar iron bonding with sulfur. Considering FeS has an average size of 11 nm in this catalyst according to Scherrer equation estimation, there may be only very few FeS nanocrystals in the whole sample, which probably is undetected by XPS. It is found in **Table 6-3a** that both ex situ catalysts have two to three times higher concentration of Fe than in situ ones. The high iron content of ex situ samples may be attributed to less uniform distribution as compared to the in-situ materials. In the in-situ case, the pre-formed polymers and in situ silica are effectively intermixed due to the templating process, resulting in a distribution of excess metallic iron outside the polymer-silica system which is more accessible for etching after pyrolysis. However, the high iron content of ex situ catalysts is not contributing to high performance as the majority of iron atoms do not exist as atomically dispersed iron coordinated to nitrogen in Fe-N-C network. As chemical speciation in **Table 6-3d** shows, more than 30% of iron in 26AMP-ex and 26DAP-ex samples is present as a metallic iron-rich phase. For comparison, 26AMP-in has negligible metallic iron content. This low metallic iron content and a higher amount of iron in the form of atomically dispersed in the carbon matrix can contribute to higher catalytic performance in both acidic and alkaline electrolytes. This sample also has the smallest amount of nitrogen detected with the highest amount of hydrogenated nitrogen present. Very small amounts of sulfur were detected in 26DAP-ex sample which also has the largest amount of overall iron detected. Ex situ samples have the highest amount of nitrogen coordinated to metal detected and smallest amounts of hydrogenated nitrogen. Highest amounts of defects as manifested by the amount of surface oxides are present in 26AMP-ex and 26DAP-in samples. As we will discuss below the differences in chemical speciation of nitrogen and carbon are not directly responsible for differences in catalytic performance.

It is believed that the difference in catalytic performance in these materials is not so much governed by chemical composition as by electrolyte accessibility to catalytic sites which is a direct result of surface area differences in these catalysts.

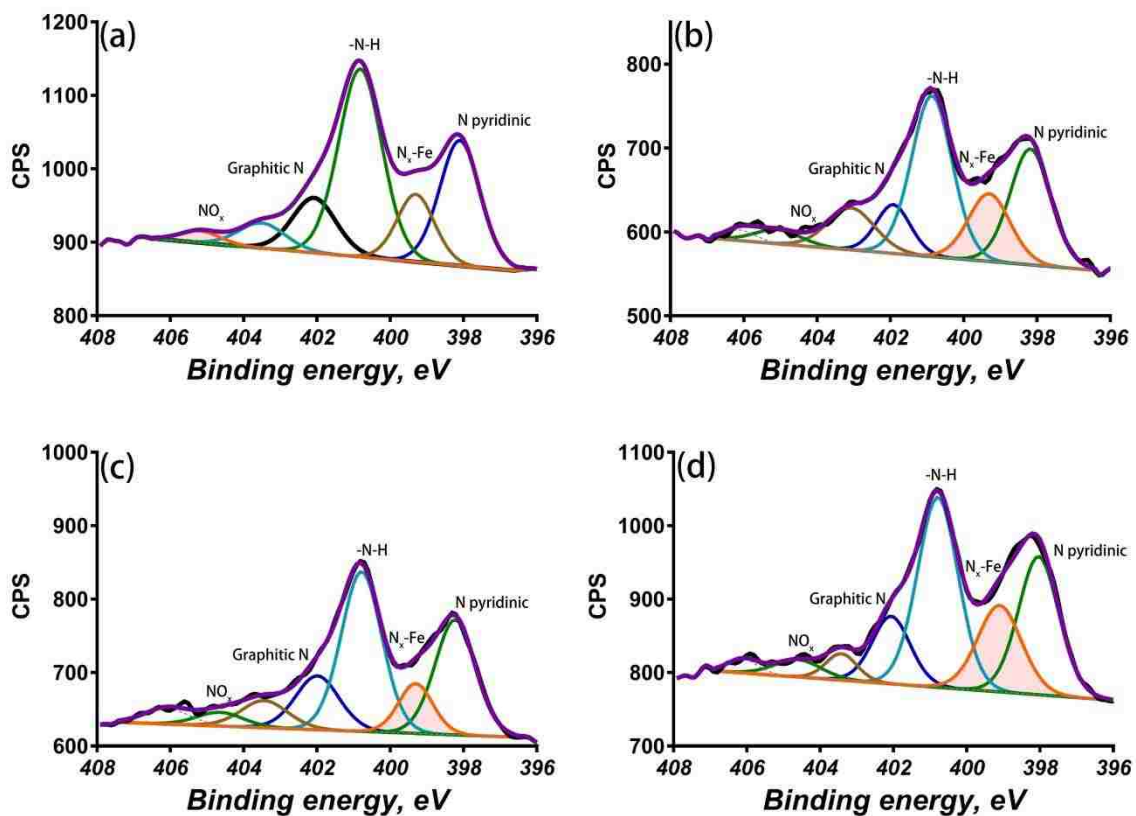


**Figure 6-5.** XPS spectra of nitrogen in different catalysts (a) 26AMP-in, (b) 26AMP-ex, (c) 26DAP-in, and (d) 26DAP-ex.

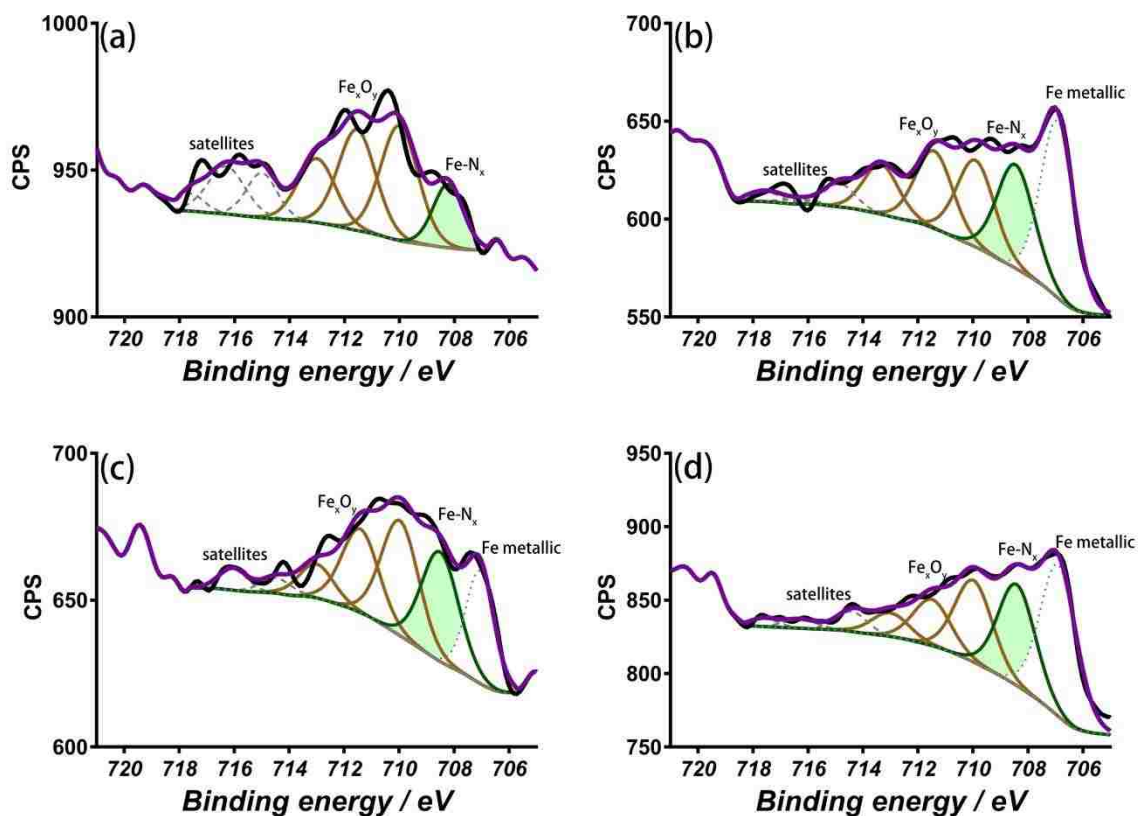


**Figure 6-6.** XPS spectra of iron in different catalysts  
 (a) 26AMP-in, (b) 26AMP-ex, (c) 26DAP-in, and (d) 26DAP-ex.

<b>Table 6-3a</b>	26AMP-in	26AMP-ex	26DAP-in	26DAP-ex
C 1s	90.5%	93.1%	91.9%	90.3%
O 1s	6.4%	2.3%	3.9%	5.1%
N 1s	2.9%	4.1%	4.0%	3.9%
Fe 2p	0.15%	0.46%	0.26%	0.53%
S 2p	N/D	N/D	N/D	0.1%

N/D: Not Detected

<b>Table 6-3b</b>	26AMP-in	26AMP-ex	26DAP-in	26DAP-ex
N pyridinic	25.6%	25.2%	26.2%	25.2%

N-metal	12.8%	15.1%	9.6%	15.1%
N-H	41.1%	34.9%	36.3%	34.9%
N graphitic	12.1%	9.0%	13.2%	9.0%
NO	8.4%	15.8%	14.7%	15.8%

<b>Table 6-3c</b>	26AMP-in	26AMP-ex	26DAP-in	26DAP-ex
C graphitic	31.3%	19.7%	31.8%	41.1%
C <sub>x</sub> O <sub>y</sub>	45.9%	63.0%	55.6%	41.3%
C-N	19.6%	12.8%	9.9%	15.7%

<b>Table 6-3d</b>	26AMP-in	26AMP-ex	26DAP-in	26DAP-ex
Fe metallic	0.0%	31.4%	19.4%	35.1%
Fe-N	15.8%	22.7%	25.2%	19.3%
Fe oxides	84.2%	45.9%	55.3%	45.7%

**Table 6-3.** XPS datasheet of different catalysts

(a) total element ratio, (b) nitrogen component ratio, (c) carbon component ratio, and (d) iron component ratio.

Representative Raman analysis was performed on the in-situ samples to analyze the structure of carbon and carbon-nitrogen network. **Figure 6-7** gives the Raman spectra of 26AMP-in and 26DAP-in. The peaks at about 1350 cm<sup>-1</sup> (D band) and 1585 cm<sup>-1</sup> (G band) reveal typical carbon features<sup>119</sup>. Both samples have broad peaks between 2500 to 3000 cm<sup>-1</sup>, the location of the 2D band and D+G band, showing the presence of amorphous carbon. The higher I<sub>D</sub>: I<sub>G</sub> ratio observed from the spectrum is a direct result and

confirmation of higher surface area of the 26AMP-in catalyst as compared to the 26DAP-in case. The analysis of Raman spectra fully supports the data obtained from XRD on presence both graphitic and amorphous components of Fe-N-C catalysts.

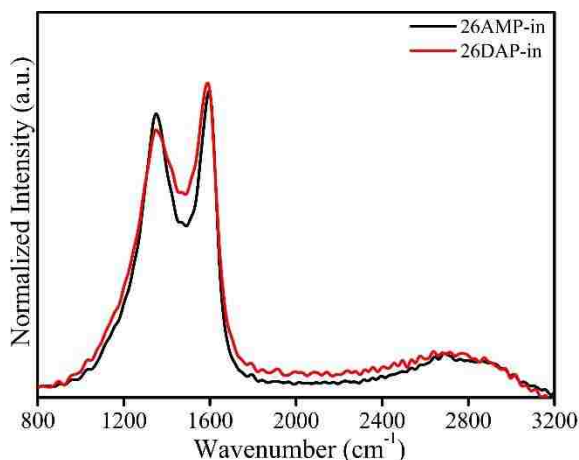


**Figure 6-7.** Raman spectra of 26AMP-in and 26DAP-in

### ***TEM figures***

TEM images express the porous feature of in situ catalysts. **Figure 6-8** presents the morphology of 26AMP-in and 26DAP-in catalysts. In the 26AMP-in sample from **Figure 6-8a**, the dense porous carbon backbone could be easily distinguished. Some of these backbones form a circle pore, but most of the pores have irregular structure. These circular pores may come from the etching of silica while the irregular pores come from the decomposition of organic molecules<sup>105</sup>. When the morphology goes to 26DAP-in as **Figure 6-8b** shows, the carbon framework is similar to 26AMP-in, but the backbone is more difficult to be recognized. It is also found that many circular shape pores in 26DAP-in catalysts do not have similar ones to be found in 26AMP-in, which implies that silica is not the only factor to form pores during the catalyst synthesis<sup>120</sup>. In addition, dense dark areas could be found in **Figure 6-8b** which indicate the severe accumulation. This agglomeration,

which could decrease the half-wave potential in LSV, probably comes from the structure of DAP and its rapid polymerization rate.

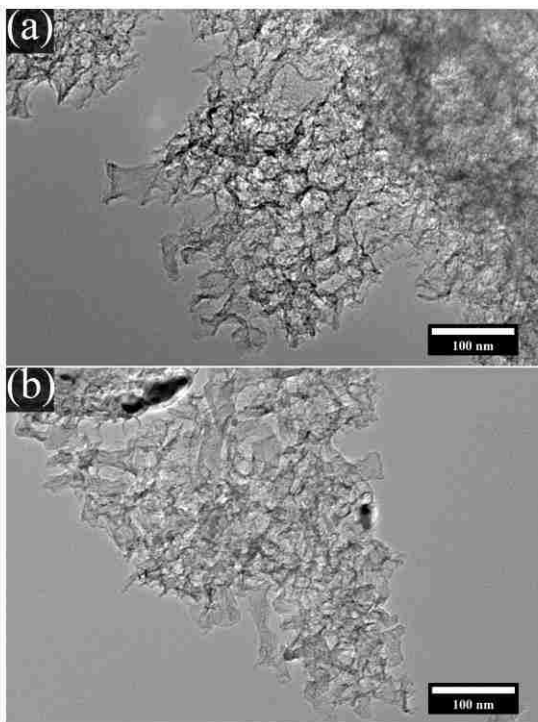


**Figure 6-8.** TEM images

(a) 26AMP-in, and (b) 26DAP-in, showing the highly porous structure of the catalysts generated by the polymerization pyrolysis protocol. In both polymers, a similar microstructure is observed.

### ***Electrochemistry Results***

To study the ORR catalytic properties of pyrolyzed aminopyridine polymers, Linear sweep voltammetry (LSV) was performed under RDE rotation of 1600 rpm with a scanning rate of  $5 \text{ mV s}^{-1}$  in  $\text{O}_2$  saturated 1 M KOH and 0.5 M  $\text{H}_2\text{SO}_4$  electrolytes. In the alkaline electrolyte, as **Figure 6-9a** shows, in the case when silica template is mixed with N-C precursor after polymerization by ball milling, the current densities of 26AMP-ex and 26DAP-ex are  $3.8$  and  $3.1 \text{ mA cm}^{-2}$  respectively, while the corresponding half-wave potentials are  $\sim 0.88 \text{ V}$  and  $\sim 0.87 \text{ V}$  versus RHE (obtained by calculating the highest derivative values in mixed kinetic-diffusion section). When silica was used as a template

during the polymerization, 26DAP-in gives better performance in both current density and half-wave potential than ex-situ one. It has a current density of  $3.2 \text{ mA cm}^{-2}$  with a related half-wave potential of  $\sim 0.87 \text{ V}$ . Meanwhile 26AMP-in gives a similar current density to that of 26AMP-ex with the half-wave potential of  $\sim 0.89 \text{ V}$ . It is obvious that both in-situ and ex-situ samples prepared from 26AMP polymers have much higher current density than those from the 26DAP polymers, probably due to higher surface areas. However, all four samples have similar half-wave potentials around  $\sim 0.85 \text{ V}$  versus RHE, which may be an indication of the similar density of the same type of active sites. Corresponding to the previous research<sup>121</sup>, the Pt/C benchmark catalyst tested in  $0.1 \text{ M KOH}$ ,  $1600 \text{ rpm}$  and a scanning rate of  $5 \text{ mV s}^{-1}$  exhibits a half-wave potential of  $0.85 \text{ V}$  and maximum diffusion current density of near  $6 \text{ mA cm}^{-2}$ . The four materials have competitive half-wave potentials but lower current density in diffusion part which could be attributed to the much higher viscosity in  $1 \text{ M KOH}$  medium.

LSV in  $0.5 \text{ M H}_2\text{SO}_4$  electrolyte is presented on **Figure 6-9c**. AMP-based catalysts exhibit give better half-wave potentials than DAP based ones. 26AMP-in has a  $\sim 0.74 \text{ V } E_{1/2}$  versus RHE with  $3.4 \text{ mA cm}^{-2}$  limiting current density while 26AMP-ex reaches a half wave potential of  $\sim 0.75 \text{ V}$  with a little lower current density ( $3.1 \text{ mA cm}^{-2}$ ). As a comparison, 26DAP-in has a half wave potential of  $\sim 0.70 \text{ V}$  and 26DAP-ex possesses the lowest value of  $\sim 0.65 \text{ V}$ . The limiting current density values of these catalysts are similar with AMP ones. The Pt/C benchmark<sup>122</sup> in the acid medium was reported to exhibit about  $0.85 \text{ V}$  of half-wave potential and  $6.5 \text{ mA cm}^{-2}$  of diffusion current density in  $0.1 \text{ M HClO}_4$  tested via  $1600 \text{ rpm}$  and  $5 \text{ mV s}^{-1}$ . The four polymerization-pyrolysis samples here still



have about 0.10 V difference with PGM catalysts. Similar with KOH situation, the concentrated 0.5 M H<sub>2</sub>SO<sub>4</sub> also limits the diffusion current densities.

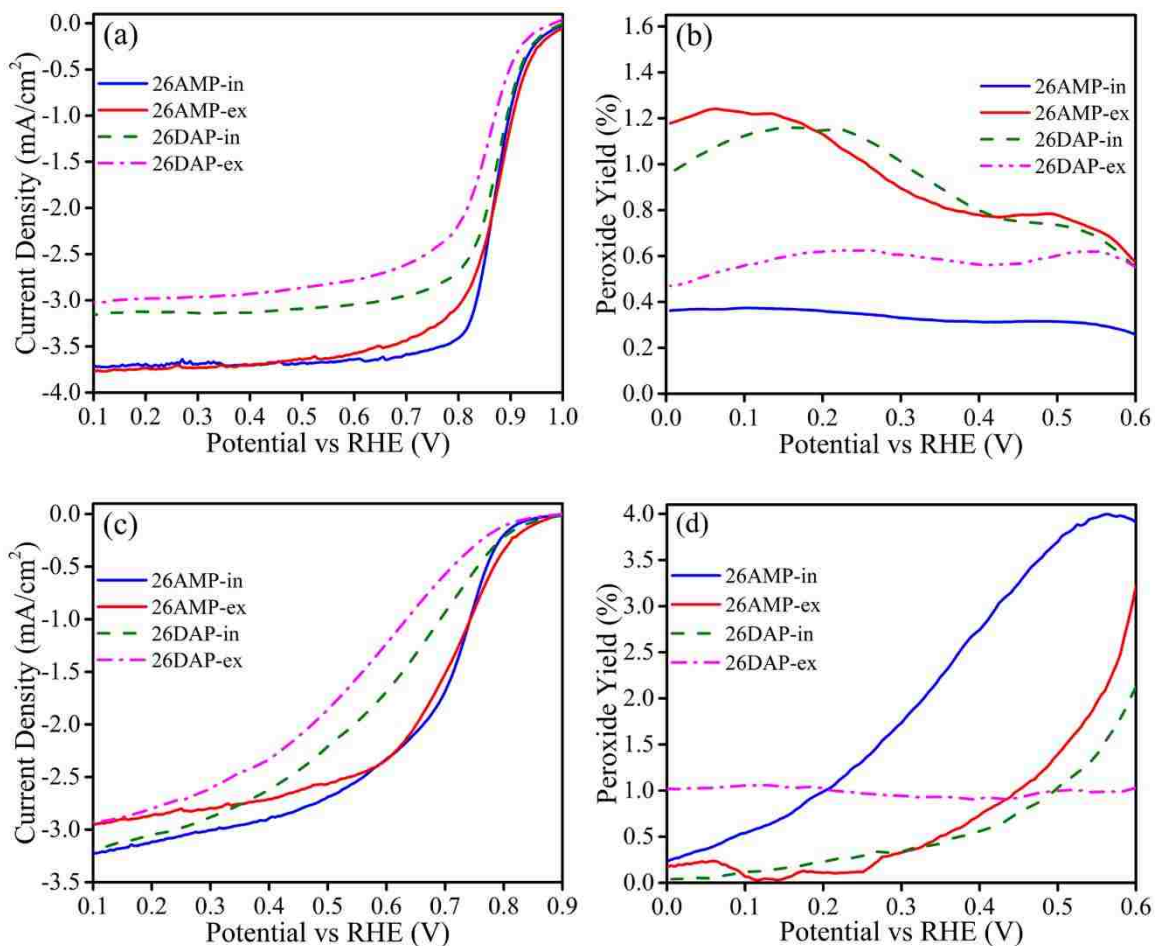


**Figure 6-9.** LSV and H<sub>2</sub>O<sub>2</sub>% in alkaline and acid  
 (a) LSV plots of 26AMP-in, 26AMP-ex, 26DAP-in and 26DAP-ex with 5 mV/s scanning rate, 1600 rpm rotation speed in RRDE and O<sub>2</sub> saturated 1 M KOH; (b) Peroxide yield generated by different Fe-N-C catalysts in 1 M KOH; (c) LSV plots of four catalysts using same conditions in 0.5 M H<sub>2</sub>SO<sub>4</sub>; (d) Peroxide yield generated by these catalysts in 0.5 M H<sub>2</sub>SO<sub>4</sub>.

Oxygen reduction reaction in the 2e<sup>-</sup> pathway results in the formation of hydrogen peroxide, which is an undesirable product resulting in degradation of fuel cell electrode components (ionomer and membrane). The %H<sub>2</sub>O<sub>2</sub> formation can be calculated by the following equation:

$$\%H_2O_2 = \frac{2I_{Ring}/N}{I_{Disk}+I_{Ring}/N} \times 100\% \quad \text{Eq. 6-1}$$

where  $I_{Ring}$  is the ring current,  $I_{Disk}$  is the disk current and  $N$  is collection efficiency ( $N = 0.42$ ). As **Figure 6-9b** shows, 26AMP-in also gives lower peroxide concentration. This production is permanent in selected potential range and keeps lower than 0.4% from 0 V to 0.6 V versus RHE. This value is substantially lower of the 2% target which is set by US Department of Energy Durability Working Group<sup>123</sup>. The other samples have a similar ultralow peroxide generation on the level of  $\sim 1.2\%$ . Also, 26DAP-in gives higher peroxide yield than ex-situ. This result is converse with the comparison between 26AMP-in and 26AMP-ex. When the case goes to the acidic environment as **Figure 6-9d** shows, the peroxide concentration goes down when the potential drops, whose trend is reverse with the one in the base. 26AMP-in, 26AMP-ex, and 26DAP-in all reach lower than 5%  $H_2O_2$  yield between 0 V and 0.2 V versus RHE. Among all eight measurements in both acid and base electrolytes, 26DAP-ex shows potential independent behavior. The yield keeps around 0.6% in potassium hydroxide and around 1.0% in sulfuric acid. Higher peroxide yield in alkaline media for 26AMP-ex and 26DAP-in may be explained by the highest amount of hydrogenated nitrogen present in these materials. Sample 26DAP-ex also has the highest amount of metallic iron which contributes to the steady generation of hydrogen peroxide in acidic media. No specific correlations between nitrogen chemistry and  $E_{1/2}$  observed have been found indicating that the role of chemistry is overshadowed by the differences in surface area.

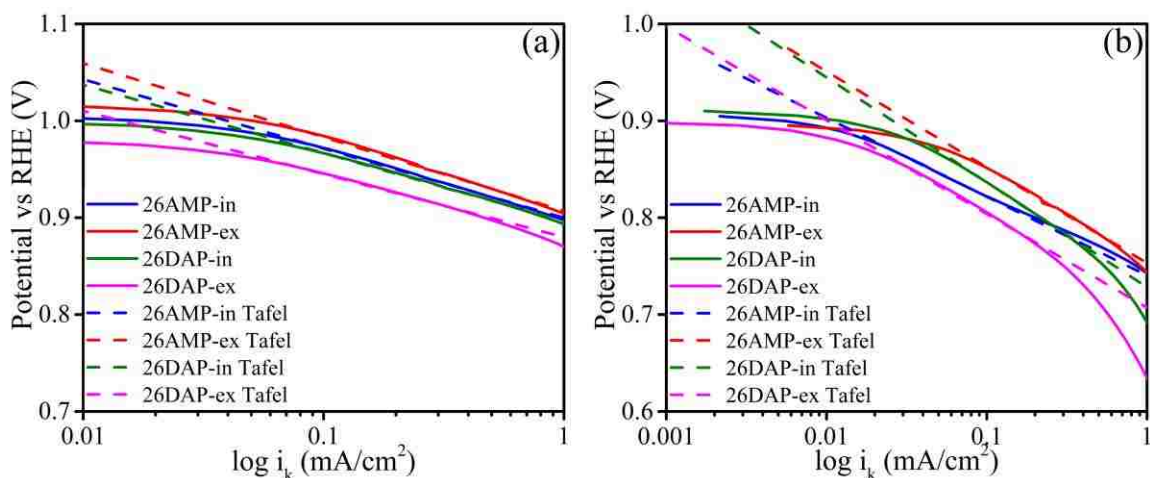


**Figure 6-10.** Tafel plots of four electrocatalysts (a) in 1 M KOH, and (b) in 0.5 M sulfuric acid.

Electrolyte	Catalyst	R <sup>2</sup> fit	Tafel slope (mV dec <sup>-1</sup> )	Y-Intercept (V)
1.0 M KOH	26AMP-in	0.9979	71.5	0.900
	26AMP-ex	0.9958	76.3	0.907
	26DAP-in	0.9986	70.5	0.896
	26DAP-ex	0.9974	65.1	0.880
0.5 M H <sub>2</sub> SO <sub>4</sub>	26AMP-in	0.9996	81.3	0.740
	26AMP-ex	0.9975	98.9	0.753
	26DAP-in	0.9997	108.2	0.728
	26DAP-ex	0.9952	96.8	0.707

**Table 6-4.** Parameters of Tafel plots

Based on the above RRDE plots above, corresponding Tafel plots are shown in **Figure 6-10**. Detailed parameters are listed in **Table 6-4**. The kinetic part of ORR plots that are independent of rotational speed and used for analysis is down to 0.90 V in alkaline and 0.80 V in acid respectively. The Tafel slopes reflect how quickly the current density

changes at low overpotentials. In the kinetic region, it needs 81 mV in potential in acid to change an order of magnitude for current, while in the base it only needs around 70 mV. It is found that for 26AMP catalysts, in-situ one performs better than ex situ one, while for 26DAP catalysts, the trend is inverse: ex situ one performs better. Considering the polymerization rate of diamino pyridine is already very high even without any silica template, in addition to the stable peroxide concentration of 26DAP-ex in both acid and alkaline, the introduction of silica probably interferes the formation of some nitrogen-carbon network. Moreover, if we only compare the Tafel plots of two ex situ catalysts, 26DAP-ex could always catalyze oxygen faster than 26AMP-ex. This phenomenon indicates that the steric hindrance of methyl group also has interference to the formation of the specific nitrogen-carbon network. If we only consider the number of active sites after pyrolyzing the polymer, two amino groups without any polymerization obstacles are preferred. However, to get the good kinetic property as well as excellent half-wave potential and diffusion current density, there is a balance between surface area and active sites to be found out. According to the previous research for Pt/C catalyst Tafel plots<sup>83</sup>, traditional platinum-based catalysts have two-step Tafel slopes ranging from 60 mV dec<sup>-1</sup> to 120 mV dec<sup>-1</sup> in 0.5 M sulfuric acid, while in 1 M NaOH they exhibit a two-step Tafel slopes ranging from 65-82 mV dec<sup>-1</sup>. The four AMP and DAP catalysts here especially 26DAP-ex have competitive one-step Tafel slopes in alkaline media. Considering the peroxide yielding trends in alkaline and acid, they probably exhibit 4e<sup>-</sup> mechanism during kinetic region in alkaline medium but 2e<sup>-</sup> mechanism in acid.

## Chapter Conclusion

The Fe-N-C electrocatalysts for oxygen reduction reaction were synthesized by polymerization of aminopyridine organic molecules in combination with Sacrificial Support Method. The catalysts prepared by in situ implementation of sacrificial support, as well as ex-situ, show high limiting current densities and noticeably high values for half-wave potentials in both acidic ( $\sim 0.70$  to  $\sim 0.75$  V vs. RHE) and basic ( $\sim 0.88$  V vs. RHE) electrolytes in RRDE tests. AMP-derived catalyst has the lowest peroxide yield in the range of 0.4% in 1 M KOH solution. Because polymerization was done with no inactive carbon added, the density of active sites is expected to be higher compared with conventional synthesis reported on polyaniline-derived ORR PGM-free materials. This work offers future directions to use simple amino aromatic compounds such as pyridine, imidazole, benzimidazole and pyrimidine with one or two amino groups to synthesize 3D high surface area Fe-N-C ORR catalyst for fuel cell application.

In addition, it is found that the content of metallic iron is more important for the LSV performance than nitrogen active sites. The optimization of Fe-N-C synthesis should focus on obtaining atomically dispersed Fe-N<sub>x</sub> first, followed by controlling the ratio of hydrogenated N and pyridinic N active sites.

## Chapter 7

### Conclusion and Outlook

#### Conclusion

This dissertation mainly investigates the active sites and corresponding inhibition effect of metal-nitrogen-carbon based electrocatalysts for oxygen reduction reaction in acidic proton-exchange membrane fuel cell. It is divided into three part: (1) proton dependence / independence of rate-determining step by using kinetic isotope effect of proton / deuteron, (2) selective inhibition of iron active sites and pyridinic nitrogen actives by using nitrogen-contained molecule probe Tris (tris-(hydroxymethyl)aminomethane), and (3) selective inhibition of pyrrolic / hydrogenated nitrogen by using nitrogen-free molecule probe HEDP (1-hydroxyethane-1,1-diphosphonic acid). All three sections involve the transfer of proton, (i) from solution to active sites by mass transport or surface diffusion, (ii) from a protonated inhibitor to deprotonated nitrogen active sites, and (iii) from protonated nitrogen active site to a deprotonated inhibitor.

It is found that an atomically dispersed Fe-N-C catalyst has a KIE value of around 1 derived from the kinetic-controlled region by using Tafel method, and a KIE value of about 2 derived from the mass transport-controlled region by using the Koutecky-Levich method. This result implies that the 1st charge transfer of iron active sites could be proton independent by careful optimization of synthesis on Fe-N-C catalyst structure, and that the 1st charge transfer of nitrogen active sites may be proton dependent indicating these active sites need to form an intermediate with proton and oxygen together to get electrons.

It is found that Tris is an efficient molecular probe that can permanently poison iron active sites but reversibly inhibit pyridinic nitrogen active sites. The inhibition on pyridinic

nitrogen active sites involves proton transfer from protonated Tris in an acidic solution to deprotonated pyridinic nitrogen, increasing peroxide yielding after inhibition. This molecule could be used to modify Fe-N-C catalyst to achieve specifically high peroxide production ability.

It is found that HEDP could efficiently inhibit pyrrolic / hydrogenated nitrogen active sites, without poisoning of iron active sites. This inhibition involves proton transfer from protonated nitrogen active sites to deprotonated HEDP in acidic solution, leading to low peroxide yielding after the introduction of this molecular probe. HEDP could be utilized as an enhancer to improve the fuel cell performance by making Fe-N-C prefer 4-electron pathway.

In addition, it is found that Fe-N-C catalysts synthesized by using pyridine-based nitrogen-carbon precursor through Polymerization Pyrolysis Method assisted with Sacrificial Support Method could achieve a low peroxide yielding in both acidic and alkaline environment. The corresponding pyridinic-N that reduces peroxide to water can be stabilized in a specific ratio to all N atoms in four synthesized catalyst samples. This rational design of synthesis is possible to be optimized by choosing better nitrogen monomer.

## **Outlook**

Further investigation based on this dissertation can start from the quantitative research in low loading (*e.g.* 0.2 mg cm<sup>-2</sup>) of a well synthesized catalyst: (*i*) The capacitance is essential to be tested for each deposited electrode layer, since it can correspond to the proton conductivity, the possible change of zeta-potential for the double layer, the distribution of multiple nitrogen active sites (some are Louis base while others are acid),

and carbon structure defects (possible P-N junction); *(ii)* The distinction of in-plane and edge active sites is important, as in-plane active sites may have slight shift in XPS but much more complicated pathway to finish ORR. *(iii)* The reversible blocking of a specific inhibitor needs to be checked, such as whether the inhibition of this molecule has pH dependence or not, which may require accurate acid-base titration.

In addition, Koutecky-Levich and Tafel methods need extra experiments in low loading of catalyst for more theoretic explanation and discussion. *(i)* Tafel method needs strict conditions to be practically meaningful: a) 1st charge transfer as the rate-determining step, b) a linear range of 3 magnitude change in logarithm, c) as less as possible porosity for the electrode, d) as same as possible electrode layer for the comparison of different tests. *(ii)* Koutecky-Levich method also has rigorous requirement though 1st charge transfer not needed for the usage: the porosity of the electrode layer should be as low as possible as the diffusion coefficient change of oxygen molecule and proton become non-negligible at the Helmholtz plane from bulk solution diffusion layer to electrode, and inside the pores of the catalysts.

Also, the rational design to get a specific ratio of N-H or pyridinic N active sites needs more investigation after achieving atomically dispersed Fe active sites. It is still unknown whether pyrrole-derived catalyst or pyridine-derived catalyst is more controllable on the selectivity of 2-electron ORR pathway. It is as well unknown whether protonated inhibitor or deprotonated inhibitor is more efficient to modify the Fe-N-C catalyst synthesized from this rational design.



## References

1. Sulaiman, N.; Hannan, M. A.; Mohamed, A.; Majlan, E. H.; Wan Daud, W. R., A review on energy management system for fuel cell hybrid electric vehicle: Issues and challenges. *Renewable and Sustainable Energy Reviews* **2015**, *52*, 802-814.
2. Wang, H.; Park, J. D.; Ren, Z. J., Practical energy harvesting for microbial fuel cells: a review. *Environ Sci Technol* **2015**, *49* (6), 3267-77.
3. Qiao, J.; Liu, Y.; Hong, F.; Zhang, J., A review of catalysts for the electroreduction of carbon dioxide to produce low-carbon fuels. *Chem Soc Rev* **2014**, *43* (2), 631-75.
4. Das, V.; Padmanaban, S.; Venkitesamy, K.; Selvamuthukumar, R.; Blaabjerg, F.; Siano, P., Recent advances and challenges of fuel cell based power system architectures and control – A review. *Renewable and Sustainable Energy Reviews* **2017**, *73*, 10-18.
5. Shahgaldi, S.; Hamelin, J., Improved carbon nanostructures as a novel catalyst support in the cathode side of PEMFC: a critical review. *Carbon* **2015**, *94*, 705-728.
6. Liu, Y.; Lehnert, W.; Janßen, H.; Samsun, R. C.; Stolten, D., A review of high-temperature polymer electrolyte membrane fuel-cell (HT-PEMFC)-based auxiliary power units for diesel-powered road vehicles. *Journal of Power Sources* **2016**, *311*, 91-102.
7. Chen, M.; Wang, L.; Yang, H.; Zhao, S.; Xu, H.; Wu, G., Nanocarbon/oxide composite catalysts for bifunctional oxygen reduction and evolution in reversible alkaline fuel cells: A mini review. *Journal of Power Sources* **2018**, *375*, 277-290.
8. Munjewar, S. S.; Thombre, S. B.; Mallick, R. K., Approaches to overcome the barrier issues of passive direct methanol fuel cell – Review. *Renewable and Sustainable Energy Reviews* **2017**, *67*, 1087-1104.
9. Strickland, K.; Pavlicek, R.; Miner, E.; Jia, Q.; Zoller, I.; Ghoshal, S.; Liang, W.; Mukerjee, S., Anion Resistant Oxygen Reduction Electrocatalyst in Phosphoric Acid Fuel Cell. *ACS Catalysis* **2018**, *8* (5), 3833-3843.
10. Jang, W.-J.; Kim, H.-M.; Shim, J.-O.; Yoo, S.-Y.; Jeon, K.-W.; Na, H.-S.; Lee, Y.-L.; Lee, D.-W.; Roh, H.-S.; Yoon, W. L., Deactivation of SiO<sub>2</sub> supported Ni catalysts by structural change in the direct internal reforming reaction of molten carbonate fuel cell. *Catalysis Communications* **2017**, *101*, 44-47.

11. Sunarso, J.; Hashim, S. S.; Zhu, N.; Zhou, W., Perovskite oxides applications in high temperature oxygen separation, solid oxide fuel cell and membrane reactor: A review. *Progress in Energy and Combustion Science* **2017**, *61*, 57-77.
12. APMEX Platinum Price. <https://www.apmex.com/spotprices/platinum-price>.
13. Ayers, K., Gigawatt-scale renewable hydrogen via water splitting as a case study for collaboration: The need to connect fundamental and applied research to accelerate solutions. *MRS Energy & Sustainability* **2017**, *4*, E11.
14. Xia, W.; Mahmood, A.; Liang, Z.; Zou, R.; Guo, S., Earth-Abundant Nanomaterials for Oxygen Reduction. *Angew Chem Int Ed Engl* **2016**, *55* (8), 2650-76.
15. Mauger, S. A.; Neyerlin, K. C.; Alia, S. M.; Ngo, C.; Babu, S. K.; Hurst, K. E.; Pylypenko, S.; Litster, S.; Pivovar, B. S., Fuel Cell Performance Implications of Membrane Electrode Assembly Fabrication with Platinum-Nickel Nanowire Catalysts. *Journal of The Electrochemical Society* **2018**, *165* (3), F238-F245.
16. Ying, J.; Li, J.; Jiang, G.; Cano, Z. P.; Ma, Z.; Zhong, C.; Su, D.; Chen, Z., Metal-organic frameworks derived platinum-cobalt bimetallic nanoparticles in nitrogen-doped hollow porous carbon capsules as a highly active and durable catalyst for oxygen reduction reaction. *Applied Catalysis B: Environmental* **2018**, *225*, 496-503.
17. Lin, F.; Wang, K.; Tang, Y.; Lai, J.; Lou, M.; Huang, M.; Guo, S., Enhanced bifunctional fuel cell catalysis via Pd/PtCu core/shell nanoplates. *Chem Commun (Camb)* **2018**, *54* (11), 1315-1318.
18. Montaut, A.; Moutin, S.; Chatenet, M. J.; Durstf, J. F. C.; Maillard, F. T.; Dubau, L. Hollow platinum nanoparticles for fuel cells. US9755246B2, 2017.
19. Yue, X.; He, C.; Zhong, C.; Chen, Y.; Jiang, S. P.; Shen, P. K., Fluorine-Doped and Partially Oxidized Tantalum Carbides as Nonprecious Metal Electrocatalysts for Methanol Oxidation Reaction in Acidic Media. *Adv Mater* **2016**, *28* (11), 2163-9.
20. Liu, J.; Huang, K.; Tang, H. L.; Lei, M., Porous and single-crystalline-like molybdenum nitride nanobelts as a non-noble electrocatalyst for alkaline fuel cells and electrode materials for supercapacitors. *International Journal of Hydrogen Energy* **2016**, *41* (2), 996-1001.

21. Zhen, S.; Sun, W.; Li, P.; Tang, G.; Rooney, D.; Sun, K.; Ma, X., High performance cobalt-free Cu<sub>1.4</sub>Mn<sub>1.6</sub>O<sub>4</sub> spinel oxide as an intermediate temperature solid oxide fuel cell cathode. *Journal of Power Sources* **2016**, *315*, 140-144.
22. Masud, J.; Nath, M., Co<sub>7</sub>Se<sub>8</sub> Nanostructures as Catalysts for Oxygen Reduction Reaction with High Methanol Tolerance. *ACS Energy Letters* **2016**, *1* (1), 27-31.
23. Tang, J.; Liu, J.; Li, C.; Li, Y.; Tade, M. O.; Dai, S.; Yamauchi, Y., Synthesis of Nitrogen-Doped Mesoporous Carbon Spheres with Extra-Large Pores through Assembly of Diblock Copolymer Micelles. *Angewandte Chemie* **2015**, *127* (2), 598-603.
24. Li, W.; Yang, D.; Chen, H.; Gao, Y.; Li, H., Sulfur-doped carbon nanotubes as catalysts for the oxygen reduction reaction in alkaline medium. *Electrochimica Acta* **2015**, *165*, 191-197.
25. Ma, Z.; Dou, S.; Shen, A.; Tao, L.; Dai, L.; Wang, S., Sulfur-doped graphene derived from cycled lithium-sulfur batteries as a metal-free electrocatalyst for the oxygen reduction reaction. *Angew Chem Int Ed Engl* **2015**, *54* (6), 1888-92.
26. Kaare, K.; Kruusenberg, I.; Merisalu, M.; Matisen, L.; Sammelselg, V.; Tammeveski, K., Electrocatalysis of oxygen reduction on multi-walled carbon nanotube supported copper and manganese phthalocyanines in alkaline media. *Journal of Solid State Electrochemistry* **2015**, *20* (4), 921-929.
27. Shang, L.; Yu, H.; Huang, X.; Bian, T.; Shi, R.; Zhao, Y.; Waterhouse, G. I.; Wu, L. Z.; Tung, C. H.; Zhang, T., Well-Dispersed ZIF-Derived Co,N-Co-doped Carbon Nanoframes through Mesoporous-Silica-Protected Calcination as Efficient Oxygen Reduction Electrocatalysts. *Adv Mater* **2016**, *28* (8), 1668-74.
28. Tylus, U.; Jia, Q.; Strickland, K.; Ramaswamy, N.; Serov, A.; Atanassov, P.; Mukerjee, S., Elucidating Oxygen Reduction Active Sites in Pyrolyzed Metal-Nitrogen Coordinated Non-Precious-Metal Electrocatalyst Systems. *J Phys Chem C Nanomater Interfaces* **2014**, *118* (17), 8999-9008.
29. Yang, W.; Liu, X.; Yue, X.; Jia, J.; Guo, S., Bamboo-like carbon nanotube/Fe<sub>3</sub>C nanoparticle hybrids and their highly efficient catalysis for oxygen reduction. *J Am Chem Soc* **2015**, *137* (4), 1436-9.

30. Diodati, S.; Negro, E.; Vezzù, K.; Di Noto, V.; Gross, S., Oxygen reduction reaction and X-ray photoelectron spectroscopy characterisation of carbon nitride-supported bimetallic electrocatalysts. *Electrochimica Acta* **2016**, *215*, 398-409.
31. Wu, G.; More, K. L.; Johnston, C. M.; Zelenay, P., High-performance electrocatalysts for oxygen reduction derived from polyaniline, iron, and cobalt. *Science* **2011**, *332* (6028), 443-7.
32. Chen, Y.; Gokhale, R.; Serov, A.; Artyushkova, K.; Atanassov, P., Novel highly active and selective Fe-N-C oxygen reduction electrocatalysts derived from in-situ polymerization pyrolysis. *Nano Energy* **2017**, *38*, 201-209.
33. Damjanovic, A.; Genshaw, M. A.; Bockris, J. O. M., The Mechanism of Oxygen Reduction at Platinum in Alkaline Solutions with Special Reference to H<sub>2</sub>O<sub>2</sub>. *Journal of The Electrochemical Society* **1967**, *114* (11), 1107-1112.
34. Su, L.; Jia, W.; Li, C. M.; Lei, Y., Mechanisms for enhanced performance of platinum-based electrocatalysts in proton exchange membrane fuel cells. *ChemSusChem* **2014**, *7* (2), 361-78.
35. Ge, X.; Sumboja, A.; Wu, D.; An, T.; Li, B.; Goh, F. W. T.; Hor, T. S. A.; Zong, Y.; Liu, Z., Oxygen Reduction in Alkaline Media: From Mechanisms to Recent Advances of Catalysts. *ACS Catalysis* **2015**, *5* (8), 4643-4667.
36. Artyushkova, K.; Serov, A.; Rojas-Carbonell, S.; Atanassov, P., Chemistry of Multitudinous Active Sites for Oxygen Reduction Reaction in Transition Metal–Nitrogen–Carbon Electrocatalysts. *The Journal of Physical Chemistry C* **2015**, *119* (46), 25917-25928.
37. Ghoneim, M. M., Oxygen Reduction Kinetics in Deuterated Phosphoric Acid. *Journal of The Electrochemical Society* **1985**, *132* (5), 1160-1162.
38. Mei, D.; He, Z. D.; Zheng, Y. L.; Jiang, D. C.; Chen, Y. X., Mechanistic and kinetic implications on the ORR on a Au(100) electrode: pH, temperature and H-D kinetic isotope effects. *Phys Chem Chem Phys* **2014**, *16* (27), 13762-73.
39. Tse, E. C.; Varnell, J. A.; Hoang, T. T.; Gewirth, A. A., Elucidating Proton Involvement in the Rate-Determining Step for Pt/Pd-Based and Non-Precious-Metal Oxygen Reduction Reaction Catalysts Using the Kinetic Isotope Effect. *J Phys Chem Lett* **2016**, *7* (18), 3542-7.

40. Malko, D.; Kucernak, A., Kinetic isotope effect in the oxygen reduction reaction (ORR) over Fe-N/C catalysts under acidic and alkaline conditions. *Electrochemistry Communications* **2017**, *83*, 67-71.
41. Thorum, M. S.; Hankett, J. M.; Gewirth, A. A., Poisoning the Oxygen Reduction Reaction on Carbon-Supported Fe and Cu Electrocatalysts: Evidence for Metal-Centered Activity. *The Journal of Physical Chemistry Letters* **2011**, *2* (4), 295-298.
42. von Deak, D.; Singh, D.; Biddinger, E. J.; King, J. C.; Bayram, B.; Miller, J. T.; Ozkan, U. S., Investigation of sulfur poisoning of CN<sub>x</sub> oxygen reduction catalysts for PEM fuel cells. *Journal of Catalysis* **2012**, *285* (1), 145-151.
43. Singh, D.; Mamtani, K.; Bruening, C. R.; Miller, J. T.; Ozkan, U. S., Use of H<sub>2</sub>S to Probe the Active Sites in FeNC Catalysts for the Oxygen Reduction Reaction (ORR) in Acidic Media. *ACS Catalysis* **2014**, *4* (10), 3454-3462.
44. Li, Y.; Zhou, W.; Wang, H.; Xie, L.; Liang, Y.; Wei, F.; Idrobo, J.-C.; Pennycook, S. J.; Dai, H., An oxygen reduction electrocatalyst based on carbon nanotube–graphene complexes. *Nature Nanotechnology* **2012**, *7*, 394.
45. Li, W.; Wu, J.; Higgins, D. C.; Choi, J.-Y.; Chen, Z., Determination of Iron Active Sites in Pyrolyzed Iron-Based Catalysts for the Oxygen Reduction Reaction. *ACS Catalysis* **2012**, *2* (12), 2761-2768.
46. Tylus, U.; Jia, Q.; Hafiz, H.; Allen, R. J.; Barbiellini, B.; Bansil, A.; Mukerjee, S., Engendering anion immunity in oxygen consuming cathodes based on Fe-N x electrocatalysts: Spectroscopic and electrochemical advanced characterizations. *Applied Catalysis B: Environmental* **2016**, *198*, 318-324.
47. von Deak, D.; Singh, D.; King, J. C.; Ozkan, U. S., Use of carbon monoxide and cyanide to probe the active sites on nitrogen-doped carbon catalysts for oxygen reduction. *Applied Catalysis B: Environmental* **2012**, *113-114*, 126-133.
48. Santoro, C.; Serov, A.; Villarrubia, C. W. N.; Stariha, S.; Babanova, S.; Artyushkova, K.; Schuler, A. J.; Atanassov, P., High catalytic activity and pollutants resistivity using Fe-AAPyr cathode catalyst for microbial fuel cell application. *Scientific Reports* **2015**, *5*, 16596.
49. Kneebone, J. L.; Daifuku, S. L.; Kehl, J. A.; Wu, G.; Chung, H. T.; Hu, M. Y.; Alp, E. E.; More, K. L.; Zelenay, P.; Holby, E. F.; Neidig, M. L., A Combined Probe-Molecule,

Mössbauer, Nuclear Resonance Vibrational Spectroscopy, and Density Functional Theory Approach for Evaluation of Potential Iron Active Sites in an Oxygen Reduction Reaction Catalyst. *The Journal of Physical Chemistry C* **2017**, *121* (30), 16283-16290.

50. Malko, D.; Kucernak, A.; Lopes, T., Performance of Fe-N/C Oxygen Reduction Electrocatalysts toward NO<sub>2</sub>(-), NO, and NH<sub>2</sub>OH Electroreduction: From Fundamental Insights into the Active Center to a New Method for Environmental Nitrite Destruction. *J Am Chem Soc* **2016**, *138* (49), 16056-16068.

51. Mamtani, K.; Jain, D.; Zemlyanov, D.; Celik, G.; Luthman, J.; Renkes, G.; Co, A. C.; Ozkan, U. S., Probing the Oxygen Reduction Reaction Active Sites over Nitrogen-Doped Carbon Nanostructures (CN<sub>x</sub>) in Acidic Media Using Phosphate Anion. *ACS Catalysis* **2016**, *6* (10), 7249-7259.

52. Workman, M. J.; Dzara, M.; Ngo, C.; Pylypenko, S.; Serov, A.; McKinney, S.; Gordon, J.; Atanassov, P.; Artyushkova, K., Platinum group metal-free electrocatalysts: Effects of synthesis on structure and performance in proton-exchange membrane fuel cell cathodes. *Journal of Power Sources* **2017**, *348*, 30-39.

53. Robson, M. H.; Serov, A.; Artyushkova, K.; Atanassov, P., A mechanistic study of 4-aminoantipyrine and iron derived non-platinum group metal catalyst on the oxygen reduction reaction. *Electrochimica Acta* **2013**, *90*, 656-665.

54. Rojas-Carbonell, S.; Babanova, S.; Serov, A.; Artyushkova, K.; Workman, M. J.; Santoro, C.; Mirabal, A.; Calabrese Barton, S.; Atanassov, P., Integration of Platinum Group Metal-Free Catalysts and Bilirubin Oxidase into a Hybrid Material for Oxygen Reduction: Interplay of Chemistry and Morphology. *ChemSusChem* **2017**, *10* (7), 1534-1542.

55. Rojas-Carbonell, S.; Santoro, C.; Serov, A.; Atanassov, P., Transition metal-nitrogen-carbon catalysts for oxygen reduction reaction in neutral electrolyte. *Electrochemistry Communications* **2017**, *75*, 38-42.

56. Weaver, M. J.; Nettles, S. M., Solvent isotope effects upon the thermodynamics of some transition-metal redox couples in aqueous media. *Inorganic Chemistry* **1980**, *19* (6), 1641-1646.

57. Blöchl, P. E., Projector augmented-wave method. *Physical Review B* **1994**, *50* (24), 17953-17979.

58. Kresse, G.; Joubert, D., From ultrasoft pseudopotentials to the projector augmented-wave method. *Physical Review B* **1999**, *59* (3), 1758-1775.
59. Perdew, J. P.; Burke, K.; Ernzerhof, M., Generalized Gradient Approximation Made Simple. *Physical Review Letters* **1996**, *77* (18), 3865-3868.
60. Perdew, J. P.; Burke, K.; Ernzerhof, M., Generalized Gradient Approximation Made Simple [Phys. Rev. Lett. *77*, 3865 (1996)]. *Physical Review Letters* **1997**, *78* (7), 1396-1396.
61. Kresse, G.; Furthmüller, J., Efficient iterative schemes for *ab initio* total-energy calculations using a plane-wave basis set. *Physical Review B* **1996**, *54* (16), 11169-11186.
62. Kresse, G.; Hafner, J., *Ab initio* molecular-dynamics simulation of the liquid-metal-amorphous-semiconductor transition in germanium. *Phys Rev B Condens Matter* **1994**, *49* (20), 14251-14269.
63. Blöchl, P. E.; Jepsen, O.; Andersen, O. K., Improved tetrahedron method for Brillouin-zone integrations. *Physical Review B* **1994**, *49* (23), 16223-16233.
64. Monkhorst, H. J.; Pack, J. D., Special points for Brillouin-zone integrations. *Physical Review B* **1976**, *13* (12), 5188-5192.
65. Artyushkova, K.; Matanovic, I.; Halevi, B.; Atanassov, P., Oxygen Binding to Active Sites of Fe–N–C ORR Electrocatalysts Observed by Ambient-Pressure XPS. *The Journal of Physical Chemistry C* **2017**, *121* (5), 2836-2843.
66. Parthasarathy, A., Temperature Dependence of the Electrode Kinetics of Oxygen Reduction at the Platinum/Nafion® Interface—A Microelectrode Investigation. *Journal of The Electrochemical Society* **1992**, *139* (9), 2530-2537.
67. Thompson, E. L.; Baker, D., Proton Conduction on Ionomer-Free Pt Surfaces. *ECS Transactions* **2011**, *41* (1), 709-720.
68. Paulus, U. A.; Veziridis, Z.; Schnyder, B.; Kuhnke, M.; Scherer, G. G.; Wokaun, A., Fundamental investigation of catalyst utilization at the electrode/solid polymer electrolyte interface. *Journal of Electroanalytical Chemistry* **2003**, *541*, 77-91.

69. Artyushkova, K.; Workman, M. J.; Matanovic, I.; Dzara, M. J.; Ngo, C.; Pylypenko, S.; Serov, A.; Atanassov, P., Role of Surface Chemistry on Catalyst/Ionomer Interactions for Transition Metal–Nitrogen–Carbon Electrocatalysts. *ACS Applied Energy Materials* **2018**, *1* (1), 68-77.
70. Rojas-Carbonell, S.; Artyushkova, K.; Serov, A.; Santoro, C.; Matanovic, I.; Atanassov, P., Effect of pH on the Activity of Platinum Group Metal-Free Catalysts in Oxygen Reduction Reaction. *ACS Catalysis* **2018**, *8* (4), 3041-3053.
71. Serov, A.; Tylus, U.; Artyushkova, K.; Mukerjee, S.; Atanassov, P., Mechanistic studies of oxygen reduction on Fe-PEI derived non-PGM electrocatalysts. *Applied Catalysis B: Environmental* **2014**, *150-151*, 179-186.
72. Ivanov, E. V.; Abrosimov, V. K., Specific Features of Hydration of Gaseous Nitrogen and Oxygen, Revealed from Data on Their Solubility in Water H/D Isotopomers. *Russian Journal of General Chemistry* **2005**, *75* (12), 1851-1856.
73. Battino, R.; Rettich, T. R.; Tominaga, T., The Solubility of Oxygen and Ozone in Liquids. *Journal of Physical and Chemical Reference Data* **1983**, *12* (2), 163-178.
74. Han, P.; Bartels, D. M., Temperature Dependence of Oxygen Diffusion in H<sub>2</sub>O and D<sub>2</sub>O. *The Journal of Physical Chemistry* **1996**, *100* (13), 5597-5602.
75. Cho, C. H.; Urquidi, J.; Singh, S.; Robinson, G. W., Thermal Offset Viscosities of Liquid H<sub>2</sub>O, D<sub>2</sub>O, and T<sub>2</sub>O. *The Journal of Physical Chemistry B* **1999**, *103* (11), 1991-1994.
76. Martens, C. P. V. J., Beyond the Structure: Deciphering the Molecular Mechanisms of Secondary Transport with Hydrogen-Deuterium Exchange Mass Spectrometry. *Biophysical Journal* **2018**, *114* (3), 334a.
77. Lou, X.; Lafleur, R. P. M.; Leenders, C. M. A.; Schoenmakers, S. M. C.; Matsumoto, N. M.; Baker, M. B.; van Dongen, J. L. J.; Palmans, A. R. A.; Meijer, E. W., Dynamic diversity of synthetic supramolecular polymers in water as revealed by hydrogen/deuterium exchange. *Nature Communications* **2017**, *8*, 15420.
78. Serov, A. A.; Min, M.; Chai, G.; Han, S.; Seo, S. J.; Park, Y.; Kim, H.; Kwak, C., Electroreduction of oxygen over iron macrocyclic catalysts for DMFC applications. *Journal of Applied Electrochemistry* **2009**, *39* (9), 1509-1516.



79. Sahraie, N. R.; Kramm, U. I.; Steinberg, J.; Zhang, Y.; Thomas, A.; Reier, T.; Paraknowitsch, J. P.; Strasser, P., Quantifying the density and utilization of active sites in non-precious metal oxygen electroreduction catalysts. *Nat Commun* **2015**, *6*, 8618.
80. Zitolo, A.; Goellner, V.; Armel, V.; Sougrati, M. T.; Mineva, T.; Stievano, L.; Fonda, E.; Jaouen, F., Identification of catalytic sites for oxygen reduction in iron- and nitrogen-doped graphene materials. *Nat Mater* **2015**, *14* (9), 937-42.
81. Olson, T. S.; Pylypenko, S.; Fulghum, J. E.; Atanassov, P., Bifunctional Oxygen Reduction Reaction Mechanism on Non-Platinum Catalysts Derived from Pyrolyzed Porphyrins. *Journal of The Electrochemical Society* **2010**, *157* (1), B54-B63.
82. Chen, Y.; Artyushkova, K.; Rojas-Carbonell, S.; Serov, A.; Matanovic, I.; Santoro, C.; Asset, T.; Atanassov, P., Inhibition of Surface Chemical Moieties by Tris(hydroxymethyl)aminomethane: A Key to Understanding Oxygen Reduction on Iron–Nitrogen–Carbon Catalysts. *ACS Applied Energy Materials* **2018**, *1* (5), 1942-1949.
83. Shinagawa, T.; Garcia-Esparza, A. T.; Takanabe, K., Insight on Tafel slopes from a microkinetic analysis of aqueous electrocatalysis for energy conversion. *Sci Rep* **2015**, *5*, 13801.
84. Huang, J.; Zhang, J.; Eikerling, M., Unifying theoretical framework for deciphering the oxygen reduction reaction on platinum. *Physical Chemistry Chemical Physics* **2018**, *20* (17), 11776-11786.
85. Hu, Y.; Jensen, J. O.; Pan, C.; Cleemann, L. N.; Shypunov, I.; Li, Q., Immunity of the Fe-N-C catalysts to electrolyte adsorption: Phosphate but not perchloric anions. *Applied Catalysis B: Environmental* **2018**, *234*, 357-364.
86. Chung, M. W.; Chon, G.; Kim, H.; Jaouen, F.; Choi, C. H., Electrochemical Evidence for Two Sub-families of FeN<sub>x</sub>C<sub>y</sub> Moieties with Concentration-Dependent Cyanide Poisoning. *ChemElectroChem* **2018**, *5* (14), 1880-1885.
87. Malko, D.; Kucernak, A.; Lopes, T., In situ electrochemical quantification of active sites in Fe–N/C non-precious metal catalysts. *Nature Communications* **2016**, *7*, 13285.
88. Janarthanan, R.; Serov, A.; Pilli, S. K.; Gamarra, D. A.; Atanassov, P.; Hibbs, M. R.; Herring, A. M., Direct Methanol Anion Exchange Membrane Fuel Cell with a Non-Platinum Group Metal Cathode based on Iron-Aminoantipyrine Catalyst. *Electrochimica Acta* **2015**, *175* (Supplement C), 202-208.

89. Sebastián, D.; Baglio, V.; Aricò, A. S.; Serov, A.; Atanassov, P., Performance analysis of a non-platinum group metal catalyst based on iron-aminoantipyrine for direct methanol fuel cells. *Applied Catalysis B: Environmental* **2016**, *182* (Supplement C), 297-305.
90. Serov, A.; Robson, M. H.; Halevi, B.; Artyushkova, K.; Atanassov, P., Highly active and durable templated non-PGM cathode catalysts derived from iron and aminoantipyrine. *Electrochemistry Communications* **2012**, *22* (Supplement C), 53-56.
91. Kattel, S.; Atanassov, P.; Kiefer, B., Stability, Electronic and Magnetic Properties of In-Plane Defects in Graphene: A First-Principles Study. *The Journal of Physical Chemistry C* **2012**, *116* (14), 8161-8166.
92. Sebastián, D.; Serov, A.; Matanovic, I.; Artyushkova, K.; Atanassov, P.; Aricò, A. S.; Baglio, V., Insights on the extraordinary tolerance to alcohols of Fe-N-C cathode catalysts in highly performing direct alcohol fuel cells. *Nano Energy* **2017**, *34*, 195-204.
93. Šljivančanin, Ž.; Hammer, B., Oxygen dissociation at close-packed Pt terraces, Pt steps, and Ag-covered Pt steps studied with density functional theory. *Surface Science* **2002**, *515* (1), 235-244.
94. Hyman, M. P.; Medlin, J. W., Theoretical study of the adsorption and dissociation of oxygen on Pt(111) in the presence of homogeneous electric fields. *J Phys Chem B* **2005**, *109* (13), 6304-10.
95. Li, R.; Li, H.; Liu, J., First principles study of O<sub>2</sub> dissociation on Pt(111) surface: Stepwise mechanism. *International Journal of Quantum Chemistry* **2016**, *116* (12), 908-914.
96. Gokhale, R.; Tsui, L.-K.; Roach, K.; Chen, Y.; Hossen, M. M.; Artyushkova, K.; Garzon, F.; Atanassov, P., Hydrothermal Synthesis of Platinum-Group-Metal-Free Catalysts: Structural Elucidation and Oxygen Reduction Catalysis. *ChemElectroChem* **2018**, *5* (14), 1848-1853.
97. Rojas-Carbonell, S.; Artyushkova, K.; Serov, A.; Santoro, C.; Matanovic, I.; Atanassov, P., Effect of pH on the Activity of Platinum Group Metal-Free Catalysts in Oxygen Reduction Reaction. *ACS Catalysis* **2018**, 3041-3053.

98. Ramaswamy, N.; Mukerjee, S., Influence of Inner- and Outer-Sphere Electron Transfer Mechanisms during Electrocatalysis of Oxygen Reduction in Alkaline Media. *The Journal of Physical Chemistry C* **2011**, *115* (36), 18015-18026.
99. Chen, Y.; Matanovic, I.; Weiler, E.; Atanassov, P.; Artyushkova, K., Mechanism of Oxygen Reduction Reaction on Transition Metal-Nitrogen-Carbon Catalysts: Establishing the Role of Nitrogen-containing Active Sites. *ACS Applied Energy Materials* **2018**.
100. Matanovic, I.; Artyushkova, K.; Strand, M. B.; Dzara, M. J.; Pylypenko, S.; Atanassov, P., Core Level Shifts of Hydrogenated Pyridinic and Pyrrolic Nitrogen in the Nitrogen-Containing Graphene-Based Electrocatalysts: In-Plane vs Edge Defects. *The Journal of Physical Chemistry C* **2016**, *120* (51), 29225-29232.
101. Artyushkova, K.; Serov, A.; Rojas-Carbonell, S.; Atanassov, P., Chemistry of Multitudinous Active Sites for Oxygen Reduction Reaction in Transition Metal–Nitrogen–Carbon Electrocatalysts. *J. Phys. Chem. C* **2015**, *119*, 25917–25928.
102. Workman, M. J.; Serov, A.; Tsui, L.-k.; Atanassov, P.; Artyushkova, K., Fe–N–C Catalyst Graphitic Layer Structure and Fuel Cell Performance. *ACS Energy Letters* **2017**, *2* (7), 1489-1493.
103. Matanovic, I.; Artyushkova, K.; Atanassov, P., Understanding PGM-free catalysts by linking density functional theory calculations and structural analysis: Perspectives and challenges. *Current Opinion in Electrochemistry* **2018**, *9*, 137-144.
104. Kabir, S.; Lemire, K.; Artyushkova, K.; Roy, A.; Odgaard, M.; Schlueter, D.; Oshchepkov, A.; Bonnefont, A.; Savinova, E.; Sabarirajan, D. C.; Mandal, P.; Crumlin, E. J.; Zenyuk, Iryna V.; Atanassov, P.; Serov, A., Platinum group metal-free NiMo hydrogen oxidation catalysts: high performance and durability in alkaline exchange membrane fuel cells. *Journal of Materials Chemistry A* **2017**, *5* (46), 24433-24443.
105. Serov, A.; Artyushkova, K.; Atanassov, P., Fe-N-C Oxygen Reduction Fuel Cell Catalyst Derived from Carbendazim: Synthesis, Structure, and Reactivity. *Advanced Energy Materials* **2014**, *4* (10), 1301735.
106. Serov, A.; Artyushkova, K.; Niangar, E.; Wang, C.; Dale, N.; Jaouen, F.; Sougrati, M.-T.; Jia, Q.; Mukerjee, S.; Atanassov, P., Nano-structured non-platinum catalysts for automotive fuel cell application. *Nano Energy* **2015**, *16*, 293-300.

107. Santoro, C.; Soavi, F.; Serov, A.; Arbizzani, C.; Atanassov, P., Self-powered supercapacitive microbial fuel cell: The ultimate way of boosting and harvesting power. *Biosensors and Bioelectronics* **2016**, *78*, 229-235.
108. Gokhale, R.; Chen, Y.; Serov, A.; Artyushkova, K.; Atanassov, P., Novel dual templating approach for preparation of highly active Fe-N-C electrocatalyst for oxygen reduction. *Electrochimica Acta* **2017**, *224*, 49-55.
109. Xia, W.; Masa, J.; Bron, M.; Schuhmann, W.; Muhler, M., Highly active metal-free nitrogen-containing carbon catalysts for oxygen reduction synthesized by thermal treatment of polypyridine-carbon black mixtures. *Electrochemistry Communications* **2011**, *13* (6), 593-596.
110. Gokhale, R.; Chen, Y.; Serov, A.; Artyushkova, K.; Atanassov, P., Direct synthesis of platinum group metal-free Fe-N-C catalyst for oxygen reduction reaction in alkaline media. *Electrochemistry Communications* **2016**, *72*, 140-143.
111. He, Y.; Han, X.; Du, Y.; Song, B.; Xu, P.; Zhang, B., Bifunctional Nitrogen-Doped Microporous Carbon Microspheres Derived from Poly(o-methylaniline) for Oxygen Reduction and Supercapacitors. *ACS Applied Materials & Interfaces* **2016**, *8* (6), 3601-3608.
112. Li, S.; Wu, D.; Cheng, C.; Wang, J.; Zhang, F.; Su, Y.; Feng, X., Polyaniline-Coupled Multifunctional 2D Metal Oxide/Hydroxide Graphene Nanohybrids. *Angewandte Chemie International Edition* **2013**, *52* (46), 12105-12109.
113. Sapurina, I.; Stejskal, J., The mechanism of the oxidative polymerization of aniline and the formation of supramolecular polyaniline structures. *Polymer International* **2008**, *57* (12), 1295-1325.
114. Gillissen, S.; Jonforsen, M.; Kesters, E.; Johansson, T.; Theander, M.; Andersson, M. R.; Inganäs, O.; Lutsen, L.; Vanderzande, D., Synthesis and Characterization of Poly(pyridine vinylene) via the Sulfinyl Precursor Route. *Macromolecules* **2001**, *34* (21), 7294-7299.
115. Mehrani, K.; Mehrani, A.; Amini, M. M.; Sadeghi, O.; Tavassoli, N., Dipyrildamine-modified nanoporous silicas as new sorbents for the separation and pre-concentration of palladium. *Microchimica Acta* **2011**, *173* (3), 521.

116. Grill, A., Porous pSiCOH Ultralow-k Dielectrics for Chip Interconnects Prepared by PECVD. *Annual Review of Materials Research* **2009**, *39* (1), 49-69.
117. Büyükmurat, Y.; Akalin, E.; Özel, A. E.; Akyüz, S., Calculation and analysis of IR spectrum of 2-aminopyridine. *Journal of Molecular Structure* **1999**, *482-483*, 579-584.
118. NIST Chemistry WebBook. <http://webbook.nist.gov/chemistry/>.
119. Ferrari, A. C., Raman spectroscopy of graphene and graphite: Disorder, electron–phonon coupling, doping and nonadiabatic effects. *Solid State Communications* **2007**, *143* (1), 47-57.
120. Leonard, N. D.; Artyushkova, K.; Halevi, B.; Serov, A.; Atanassov, P.; Barton, S. C., Modeling of Low-Temperature Fuel Cell Electrodes Using Non-Precious Metal Catalysts. *Journal of The Electrochemical Society* **2015**, *162* (10), F1253-F1261.
121. Sa, Y. J.; Park, C.; Jeong, H. Y.; Park, S.-H.; Lee, Z.; Kim, K. T.; Park, G.-G.; Joo, S. H., Carbon Nanotubes/Heteroatom-Doped Carbon Core–Sheath Nanostructures as Highly Active, Metal-Free Oxygen Reduction Electrocatalysts for Alkaline Fuel Cells. *Angewandte Chemie* **2014**, *126* (16), 4186-4190.
122. Pedersen, C. M.; Escudero-Escribano, M.; Velázquez-Palenzuela, A.; Christensen, L. H.; Chorkendorff, I.; Stephens, I. E. L., Benchmarking Pt-based electrocatalysts for low temperature fuel cell reactions with the rotating disk electrode: oxygen reduction and hydrogen oxidation in the presence of CO (review article). *Electrochimica Acta* **2015**, *179*, 647-657.
123. DOE Durability Working Group. <https://energy.gov/eere/fuelcells/durability-working-group>.